PANE Journal of Physics

Volume 2, Number 2, August 2026

ISSN: 3107-9342 (Online)

A Peer-reviewed Open Access Journal
Published by

Physics Academy of the North East

Table of Contents

=true

EXTERNAL CHARGED DEBRIS INDUCED NONLINEAR STRUCTURES IN A FLOWING PLASMA

Bikramjit Joardar*[1] and Madhurjya P. Bora[1]

[1]*Department of Physics, Gauhati University, Guwahati 781014, Assam, India*

*Corresponding Author: bikramjitjoardar1@gmail.com

(Received 25 September 2025; accepted 11 December 2025; published 1 August 2026)

Abstract: In this work, we investigate the nonlinear structures triggered by periodically fluctuating external charged debris in a flowing plasma. Using the forced Korteweg-de Vries (fKdV) model together with Particle-in-Cell (PIC) simulations, we demonstrate that the periodic fluctuation suppresses the pinned solitons excited by the negatively charged debris whereas the dispersive shock waves (DSWs) excited by the positively charged debris are least affected. These findings highlight the role of debris charge fluctuation in plasma dynamics and its implications for debris-induced phenomena in the low Earth orbit (LEO) plasma.

Keywords: Debris Charge Fluctuation; Solitons; Dispersive Shock Waves

PACS: 52.65.Kj, 52.35.Fp, 52.35.Tc, 52.35.Sb

1 Introduction

The subject of nonlinear structures driven by moving charged debris in a space plasma has received considerable attention not only due to their intricate nature but also due to the risks posed by such foreign entities to the numerous satellites orbiting the Earth. The topic of interaction of such objects with low Earth plasmas has gained prominence since the early space missions of the 1960s, which started studying the interaction between satellites/spacecrafts and space plasma environments [1–3]. It is now well established that such space debris can excite pinned, precursor and wake solitons as well as collisionless or dispersive shocks, depending on the velocity and polarity of such debris [4–6]. Experimental investigations have also confirmed the excitation of pinned solitons in the dust-acoustic regime in plasmas [7]. Space debris are also known to excite envelope compressional Alfvénic solitons as well as electromagnetic pinned solitons in magnetized plasmas [8]. Another study has also explored the properties of such solitons like amplitude, width and production frequency relating them with the size, velocity and position of the debris [9].

On the theoretical side, solitons are described by the Korteweg-de Vries (KdV) equation, arising out of the balance between nonlinearity and dispersion [10]. Envelope solitons are another type of nonlinear structure that can propagate while maintaining their shape because of their slowly varying envelope which modulates the comparatively faster carrier wave. Such envelope solitons can also result from a balance between nonlinearity and dispersion and is one of the solutions of the nonlinear Schrödinger equation (NLSE) [11]. The NLSE is also known to exhibit shock wave solutions, which appear in cases where the nonlinearity dominates over dispersion causing a steepening of the wavefront [12]. Such shocks can be either monotonic or oscillatory in nature and unlike solitons, they can evolve with time [13, 14]. In the context of the space debris problem, the fluid equations of the plasma can be reduced into a forced KdV (fKdV) equation, where the forcing term accounts for the charged debris. The fKdV equation can also exhibit solitons and dispersive shock wave solutions. It is worth noting that the soliton solution of the fKdV equation isn't actually a true soliton in the sense that a true soliton maintains its shape over time, unlike the fKdV solitons, which are unstable and originate from a non-integrable system [15].

In this work, we explore the effect of a periodic charge fluctuation of the debris on such nonlinear structures, for both positively and negatively charged debris. Our work is primarily focussed on the low Earth orbit (LEO) plasma where the context of plasma-debris interaction is most relevant. There could be many reasons for the variation of the debris charge including periodic photo-emissions due to eclipse transitions, debris in density gradients in the ambient plasma, etc. Among these, the most prominent mechanism is the debris charge fluctuation due to interactions with plasma waves, as it is a natural process. Debris in a plasma will inherently excite an ion-acoustic wave (IAW), which induces periodic oscillations in the ion and electron densities. This leads to a variation in the ion and electron currents reaching the debris surface. As a result, the equilibrium floating potential is disturbed and the debris charge evolves dynamically to restore the equilibrium, leading to periodic fluctuations in the debris charge [6, 16].

The manuscript is structured as follows. The governing fluid equations of the plasma-debris interaction are introduced in Section. 2. Section. 3 presents the forced Korteweg-de Vries (fKdV) analysis, and Section. 4 discusses the corresponding Particle-in-Cell (PIC) simulation results. Section. 5 concludes the paper.

2 The Plasma Model

The plasma model under consideration is 1-D, collisionless, and unmagnetized, with thermal ions and Boltzmannian electrons in the ion-acoustic regime. The external charged debris are embedded into the plasma. The relevant equations for this plasma are the ion continuity and momentum equation with the system being closed by the Poisson equation. The equations are as follows

$$\frac{\partial n_i}{\partial t} + \frac{\partial}{\partial x}(n_i v_i) = 0, \tag{1}$$

$$\frac{\partial v_i}{\partial t} + v_i \frac{\partial v_i}{\partial x} = -\frac{1}{m_i n_i}\frac{\partial p_i}{\partial x} - \frac{e}{m_i}\frac{\partial \phi}{\partial x}, \tag{2}$$

$$n_e = n_0 \exp\left(\frac{e\phi}{T_e}\right), \tag{3}$$

$$\epsilon_0 \frac{\partial^2 \phi}{\partial x^2} = e(n_e - n_i) + \rho_{ext}(t, x - v_d t), \tag{4}$$

where n_i and n_e denote the respective number densities of ions and electrons, and v_i, ϕ, and p_i represent the ion fluid velocity, electrostatic plasma potential, and ion pressure respectively. The quantities e, m_i, n_0, and T_e correspond to the electronic charge, ion mass, equilibrium plasma density, and electron temperature (in energy units) respectively. The term ρ_{ext} represents the time-dependent external charged debris moving with velocity v_d with respect to the background plasma. Depending on the charge of the debris, ρ_{ext} can be $\gtrless 0$. The ion pressure is assumed to be polytropic

$$p_i \propto n_i^{\gamma}, \tag{5}$$

with γ being the ratio of the specific heats and is equal to 2 for our current 1-D model. Upon normalization, the above model becomes

$$\frac{\partial n_i}{\partial t} + \frac{\partial}{\partial x}(n_i v_i) = 0, \tag{6}$$

$$\frac{\partial v_i}{\partial t} + v_i \frac{\partial v_i}{\partial x} = -\gamma\sigma n_i^{\gamma-2}\frac{\partial n_i}{\partial x} - \frac{\partial \phi}{\partial x}, \tag{7}$$

$$n_e = e^{\phi}, \tag{8}$$

$$\frac{\partial^2 \phi}{\partial x^2} = n_e - n_i + \rho_{ext}(t, x - v_d t), \tag{9}$$

where the ion and electron densities have been normalized by the equilibrium value n_0, velocities by the ion-sound speed $c_s = \sqrt{T_e/m_i}$, plasma potential ϕ by (T_e/e). Time is normalized by the inverse ion plasma frequency, ω_{pi} while length has been normalized by the electron Debye length, λ_D.The parameter σ denotes the ion-to-electron temperature ratio. The debris term, ρ_{ext} has also been normalized accordingly.

The debris charge density ρ_{ext} can be further expanded as

$$\rho_{ext}(x, t) = \rho(x) f(t), \tag{10}$$

where $\rho(x)$ denotes the spatial distribution of the debris and $f(t)$ represents the time-variation of the debris charge. In this work, the debris charge fluctuation is controlled externally as modeling of a self-consistent periodic fluctuation would require calculation of the collision cross-sections and subsequent ion and electron currents to the

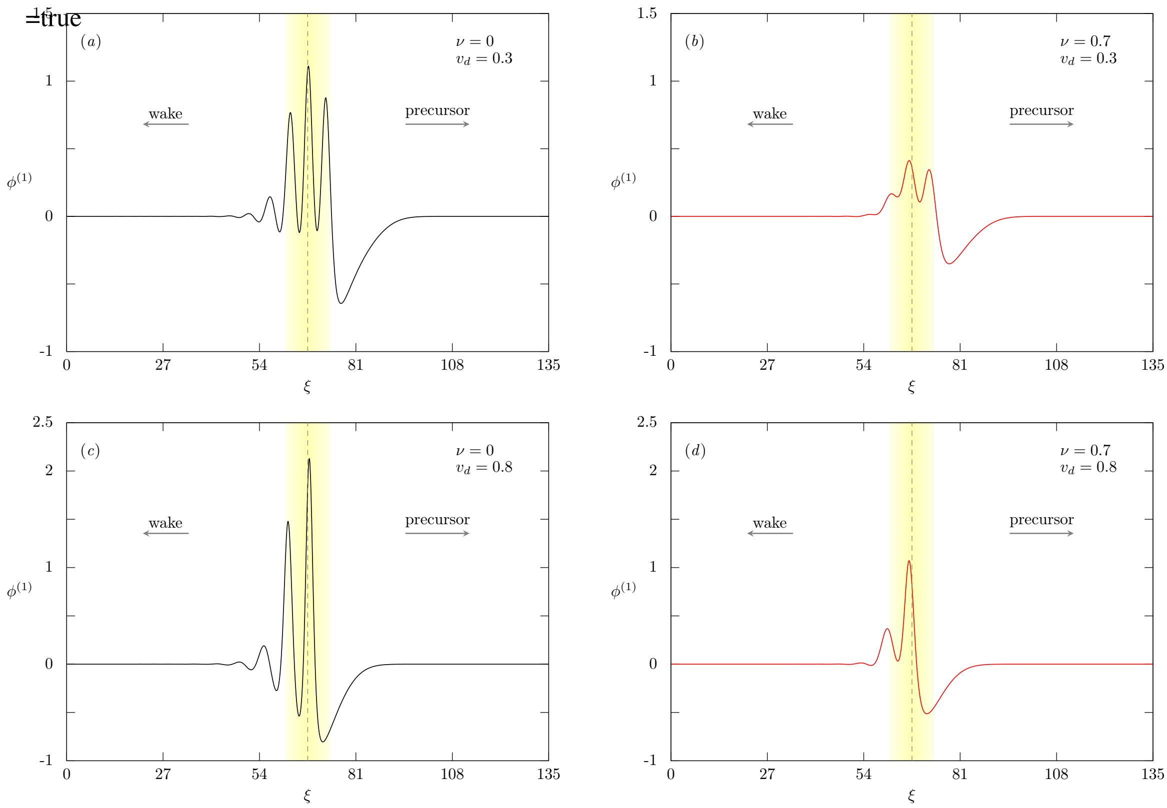

Figure 1: Solutions of the fKdV equation for negatively charged debris, where ν is the fluctuation frequency and v_d is the debris velocity normalized by the ion-acoustic speed. The figures are shown in the debris frame, indicated by the shaded vertical strip.

debris, which is computationally extensive and might not be consistent with the standard orbit motion limited (OML) theory. Besides, our externally controllable debris charge fluctuation can be seamlessly integrated into both the fKdV and PIC simulation setups. Additionally, the debris charge is assumed to be either positive definite or negative definite, while oscillating in time.

3 Forced KdV Dynamics

In order to derive the forced Korteweg-de Vries (fKdV) equation, we define the followingstretched coordinates

$$\xi = \epsilon^{1/2}(x - \lambda t), \quad \tau = \epsilon^{3/2}t, \tag{11}$$

where ϵ denotes a smallness parameter, which is $\ll 1$ and λ denotes the phase velocity of the ion-acoustic wave.

Following the reductive perturbation technique and considering a static and neutral equilibrium, we expand the variables n_i, v_i, and ϕ in powers of the parameter ϵ as

$$n_i = 1 + \epsilon n_i^{(1)} + \epsilon^2 n_i^{(2)} + \cdots, \tag{12}$$

$$v_i = \epsilon v_i^{(1)} + \epsilon^2 v_i^{(2)} + \cdots, \tag{13}$$

$$\phi = \epsilon\phi^{(1)} + \epsilon^2\phi^{(2)} + \cdots, \tag{14}$$

$$\rho_{ext} = \epsilon^2 \rho_{ext}^{(2)}, \tag{15}$$

where the external debris term has been considered as a second order perturbation [15]. As per the standard approach, at the lowest power of ϵ, we get the following relations for the first order perturbed quantities in terms

=true

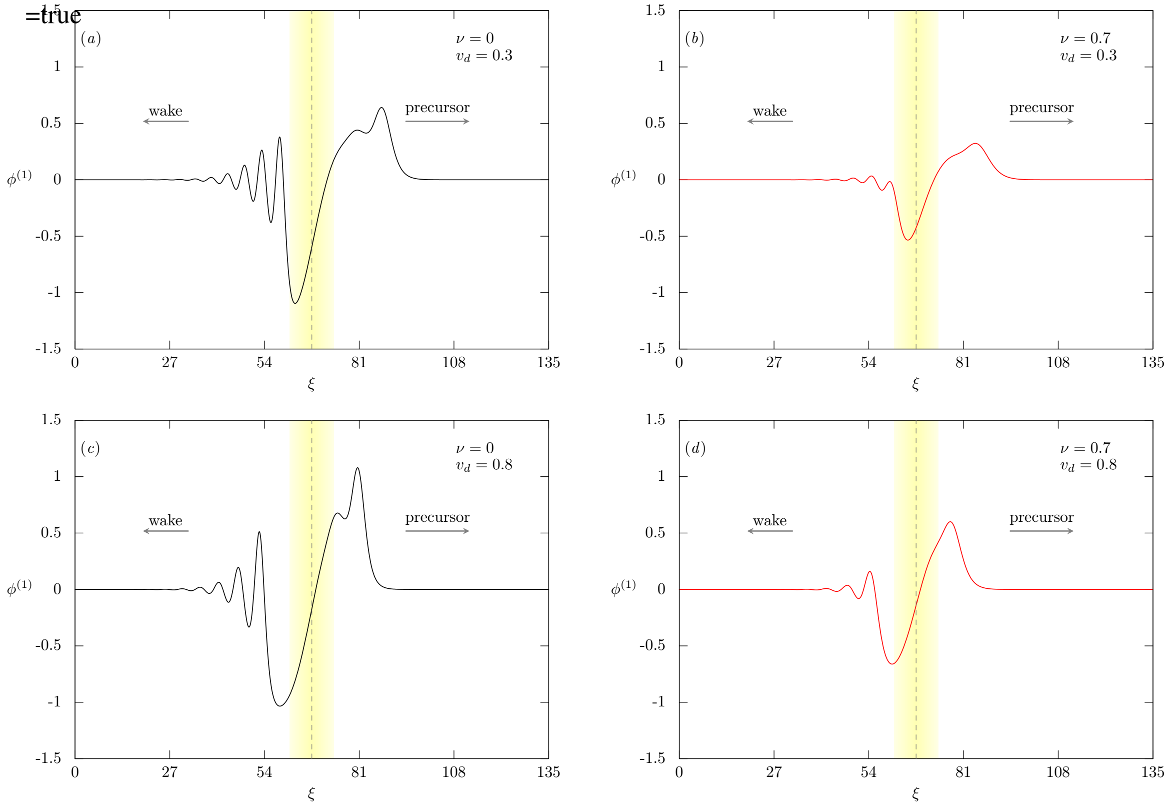

Figure 2: Solutions of the fKdV equation for positively charged debris, where ν is the fluctuation frequency and v_d is the debris velocity normalized by the ion-acoustic speed. The figures are shown in the debris frame, indicated by the shaded vertical strip.

of $\phi^{(1)}$

$$n_i^{(1)} = \frac{\phi^{(1)}}{\lambda^2 - 2\sigma}, \tag{16}$$

$$v_i^{(1)} = \frac{\lambda\phi^{(1)}}{\lambda^2 - 2\sigma}, \tag{17}$$

with the phase velocity (or the first compatibility condition) given by

$$\lambda = \sqrt{1 + 2\sigma}, \tag{18}$$

At the next higher power of ϵ, we eliminate the second order perturbed quantities using the first order relations (Eqs. 16 and 17), to get the fKdV equation as follows

$$\frac{\partial\phi^{(1)}}{\partial\tau} + A\phi^{(1)}\frac{\partial\phi^{(1)}}{\partial\xi} + B\frac{\partial^3\phi^{(1)}}{\partial\xi^3} = B\frac{\partial\rho_{ext}^{(2)}}{\partial\xi}, \tag{19}$$

with A and B denoting the coefficients of nonlinearity and dispersion respectively, and are given as

$$A = \frac{1 + 3\sigma}{\sqrt{1 + 2\sigma}}, \tag{20}$$

$$B = \frac{1}{2\sqrt{1 + 2\sigma}}, \tag{21}$$

In Eq. 19, the debris term can be expressed as

$$\rho_{ext}^{(2)} = \rho_0 \exp\left(-\frac{(\xi - v_d\tau)^2}{2\delta^2}\right)\left(\frac{1 + \lfloor sin(\nu\tau)\rfloor}{2}\right), \tag{22}$$

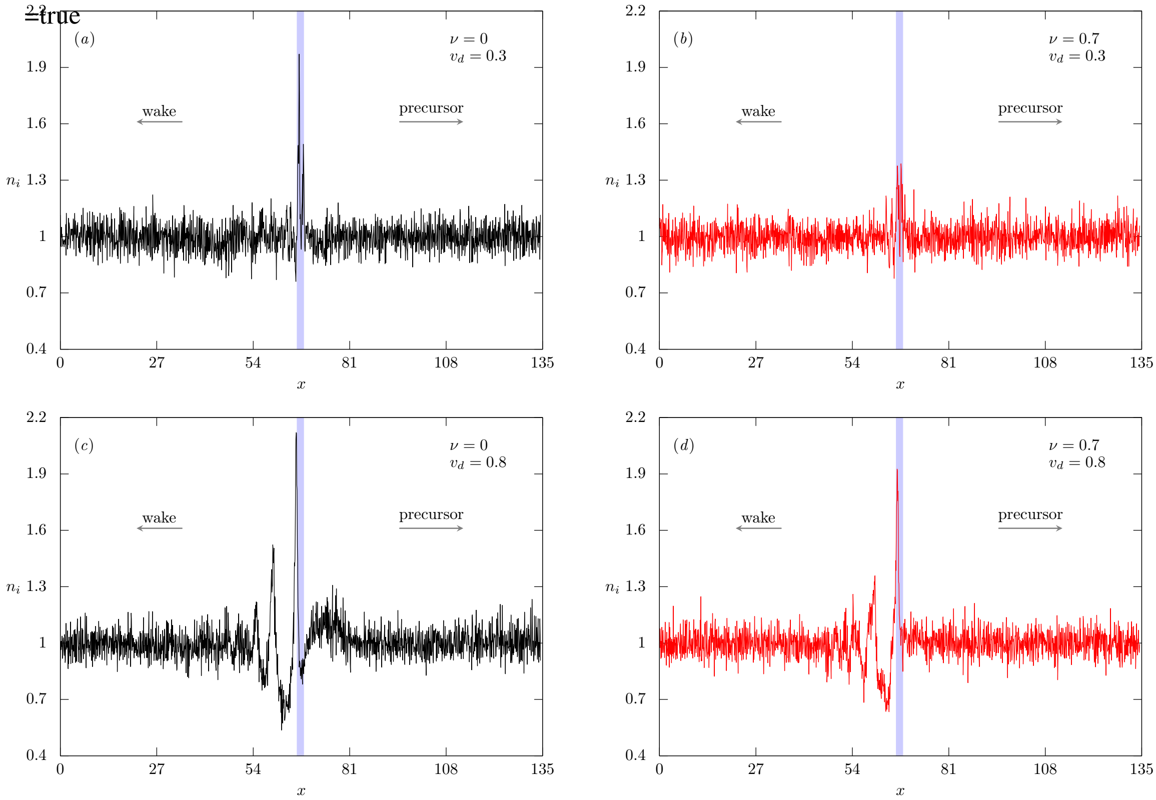

Figure 3: Ion density plots for negatively charged debris obtained from the PIC simulation after 20 ion plasma periods. The figures are shown in the debris frame, denoted by the vertical blue strip. The parameters ν and v_d are same as in Figs. 1 and 2.

where ρ_0 is the peak of the Gaussian profile of width δ moving with velocity v_d, normalized by the ion-sound speed. The term $(1 + \lfloor \sin(\nu\tau) \rfloor)/2$ modulates the debris charge by periodically turning it on and off at frequency ν.

The fKdV equation is numerically solved using the following parameters – $\rho_0 = 1.0$, $\sigma = 0.01$ and $\delta = 4.5$. The boundary conditions are assumed to be periodic with $\phi = 0$ being the initial condition. The numerical solutions for both negative and positively charged debris are now plotted in the rest frame of the debris for different values of v_d and ν in Figs. 1 and 2. For a negatively charged debris, the fKdV solutions exhibit pinned solitons localized at the debris site. These pinned solitons correspond to the ions trapped in the ion phase-space vortices, arising from the ion-ion counter streaming instability (IICSI) induced by the negatively charged debris. As the debris velocity increases, the pinned solitons begin to separate away from each other as the vortex widens, before ultimately disappearing. However, on applying a periodic fluctuation of the debris amplitude, the pinned solitons get suppressed and their formation appears to be delayed in Fig .1. When the positively charged, the plasma response is fundamentally different. In Fig .2, the positively charged debris creates a steepened precursor which evolves into a dispersive shock wave (DSW) along with an oscillatory wake. The DSW appears to be stable as the debris velocity increases. On applying the periodic fluctuation, a similar suppression of the DSW can be seen here as well.

4 PIC Simulation

In this section, we present the results obtained from a Particle-in-Cell (PIC) simulation of our e-i plasma model with the external charged debris under periodic charge fluctuation. The simulation has been performed using the h-PIC-MCC code [17, 18] which has been used in various electrostatic plasma studies like debris induced ion-ion counter streaming instability, dust-charge fluctuations, external debris induced chaotic dynamics, etc.

For relevance to the LEO region, the e-i number density of the plasma is taken as $n_{e,i} \sim 10^{16}\,\mathrm{m}^{-3}$ with

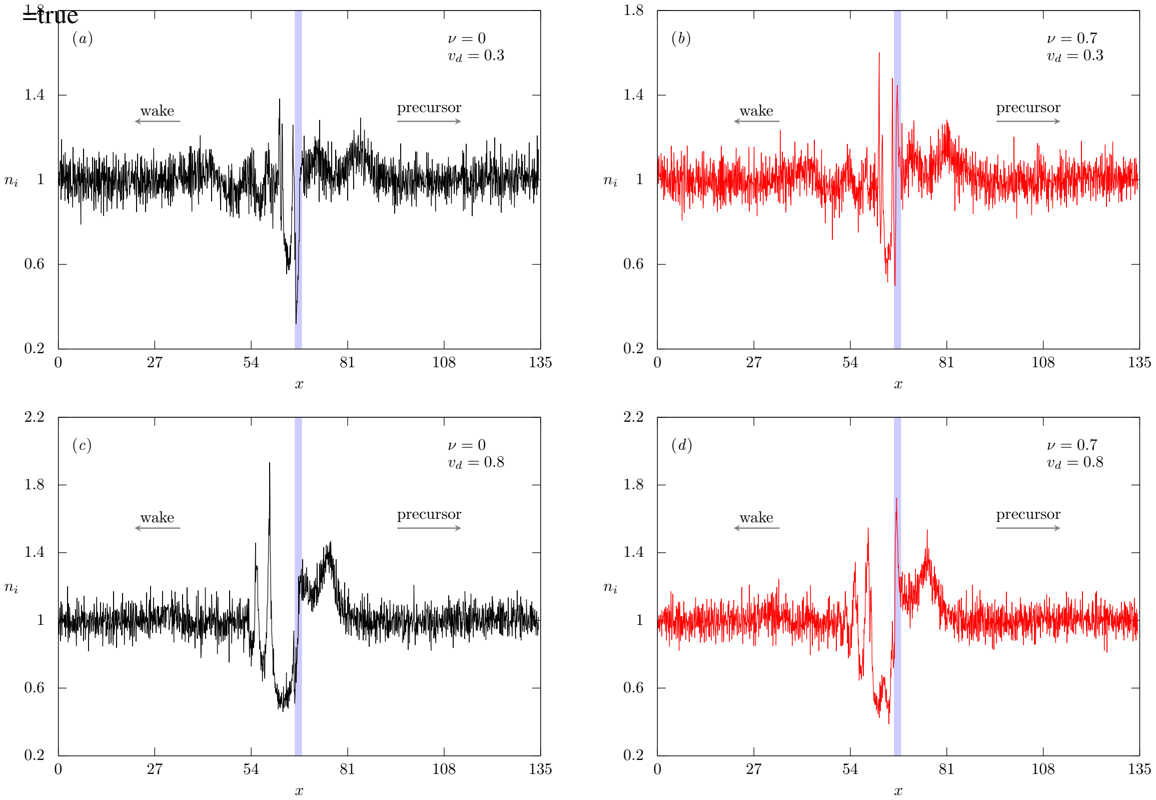

Figure 4: Ion density plots for positively charged debris obtained from the PIC simulation after 20 ion plasma periods. The figures are shown in the debris frame, indicated by the vertical blue strip. The parameters ν and v_d are same as in Figs. 1 and 2.

electron temperature $1\,\mathrm{eV}$ and ion temperature $0.01\,\mathrm{eV}$. The simulation domain has a length of $135\lambda_D$ equally discretized into 1600 cells, each having width $\sim 0.05\lambda_D$, fine enough to ensure proper resolution of Debye-scale structures. The external charged debris has been initialized at the centre of the simulation domain having width $\sim 2\lambda_D$. The simulation has been performed for 20 ion plasma periods, long enough to accurately capture the nonlinear structures induced by the debris. We should also note that the debris charge density must exceed a certain threshold value for the debris-induced nonlinear structures to emerge, otherwise the debris will be suppressed by the inherent particle noise, causing its effects to diminish rapidly. This threshold value for our plasma model happens to be 0.08 times the background charge density [5].

The simulation results for negatively charged debris are consistent with the fKdV results. However, the DSW excited by positively charged debris does not seem to be affected by the periodic debris charge fluctuation, which is contradicting the fKdV results. This discrepancy can be attributed to the fact that DSWs usually comprise multi-wavelength oscillations and their energy is spread over different wavenumbers. So, any damping in a particular wavenumber will not show up in a PIC simulation as it naturally evolves all the wavenumbers. In contrast to this, an fKdV solution will pick up only a single mode and it will show the damping (suppression) effectively.

5 Summary and Conclusion

In the present study, we have explored the various nonlinear structures generated by periodically fluctuating external charged debris in a flowing e-i plasma. Using the fluid equations of the plasma, we derived the forced Korteweg-de Vries (fKdV) equation, whose numerical solutions revealed the generation of pinned solitons for negatively charged debris and dispersive shock waves (DSWs) for positively charged debris. A key finding of the fKdV analysis was that a periodic fluctuation of the debris charge tends to suppress or delay the onset of these nonlinear structures.

To complement the fKdV results, a PIC simulation of the plasma was carried out with parameters relevant to the ~~low~~ lower Earth orbit (LEO) plasma. The simulation confirmed the suppression of pinned solitons for negatively charged debris. However, unlike the fKdV model, the DSWs excited by the positively charged debris were not significantly influenced by the periodic debris charge fluctuation. This discrepancy arises due to the PIC simulation inherently evolving multiple wavenumbers whereas the fKdV model captures only a single mode, making the suppression more apparent in the latter.

Our findings provide key insights into the effect of periodic charge fluctuation of space debris on the formation and evolution of nonlinear structures excited by the debris. These results are particularly relevant for understanding debris-plasma interactions in the LEO region, where monitoring such structures is key to the detection of space debris.

Acknowledgements

One of the authors B.J. gratefully acknowledges financial support from Gauhati University through the research fellowship grant GU/UGC/GURF/2023/712.

References

[1] A. C. Tribble, *The space environment: implications for spacecraft design*, (Princeton University Press, 2003).

[2] U. Samir, K. H. Wright Jr., and N. H. Stone, Rev. Geophys. **21**, 1631 (1983).

[3] G. L. Delzanno and X.-Z. Tang, Phys. Plasmas **22**, 113703 (2015).

[4] H. Sarkar and M. P. Bora, Phys. Plasmas **30**, 083701 (2023).

[5] M. Das and M. P. Bora, Phys. Plasmas **32**, 032301 (2025).

[6] B. Joardar, H. Sarkar, and M. P. Bora, Chaos, Solitons & Fractals **200**, 117102 (2025).

[7] G. Arora, P. Bandyopadhyay, M. G. Hariprasad, and A. Sen, Phys. Rev. E **103**, 013201 (2021).

[8] P. A. Bernhardt, L. Scott, A. Howarth, and G. J. Morales, Phys. Plasmas **30**, 092106 (2023).

[9] A. S. Truitt and C. M. Hartzell, J. Spacecr. Rockets **57**, 876 (2020).

[10] P. D. Lax, Commun. Pure Appl. Math. **21**, 467 (1968).

[11] Y. H. Ichikawa and S. Watanabe, J. Phys. Colloq. **38**, C6-15 (1977).

[12] A. M. Kamchatnov, A. Gammal, and R. A. Kraenkel, Phys. Rev. A **69**, 063605 (2004).

[13] Y. Nakamura, Phys. Plasmas **9**, 440 (2002).

[14] G. A. El and M. A. Hoefer, Physica D **333**, 11 (2016).

[15] H. Sarkar and M. P. Bora, Phys. Plasmas **32**, 062305 (2025).

[16] G. Ganguli, C. Crabtree, A. Fletcher, and A. Sen, Phys. Plasmas **32**, 022902 (2025).

[17] S. Changmai and M. P. Bora, Phys. Plasmas **26**, 042113 (2019).

[18] S. Changmai and M. P. Bora, Sci. Rep. **10**, 20980 (2020).

SILVER NANOPARTICLE DECORATED 2D-$MoSe_2$ NANOSHEETS FOR EXPLORATION OF OPTICAL PROPERTIES

Shahnaz Shabnam*[1] and Gazi Ameen Ahmed[1]

[1]*Department of Physics, Tezpur University, Napaam -784028, Assam, India*

*Corresponding Author: shahnazshabnam07@gmail.com

(Received 26 September 2025; revised 6 November 2025; accepted 13 December 2025; published 1 August 2026)

Abstract: The present work illustrates the synthesis of a transition metal dichalcogenide material (TMDC), $MoSe_2$ and its composite with Silver (Ag) nanoparticles, employing the liquid phase exfoliation method through a sonication process. The synthesized $MoSe_2$ nanosheets and $MoSe_2$–Ag nanocomposite exhibits synergistically enhanced optical properties compared to that of bulk $MoSe_2$. The optical bandgap comparison of $MoSe_2$, $MoSe_2$-Ag was investigated using UV-Vis Spectroscopy. The corresponding nanostructures were determined by Scanning Electron Microscopy (SEM), Field Emission Scanning Electron Microscopy (FESEM), X-Ray diffraction (XRD), Raman spectroscopy.

Keywords: Transition metal dichalcogenide material (TMDC); Molybdenum Diselenide ($MoSe_2$); Bandgap

PACS: 78.20.-e 78.90.+t

1 Introduction

Two-dimensional materials are regarded as highly promising candidates for next-generation applications in electronics and optoelectronics [1]. Among various 2D materials, transition metal dichalcogenides (TMDCs) (MoS_2, $MoSe_2$, $MoTe_2$, WS_2, and WSe_2) have attracted extensive research attention owing to their distinctive optical, electrical, catalytic, and mechanical properties 2,3. Molybdenum Diselenide ($MoSe_2$), a representative member of the TMDC family, is a layered 2D material that has gained significant interest due to its large surface area, tunable bandgap, etc., making it a potential candidate for applications in optoelectronic devices, energy storage, catalysis, sensing, etc. [2, 3]. Bulk $MoSe_2$ has indirect band gap of 1.1 eV, which changes to direct band gap after exfoliation. The monolayer and few layers of $MoSe_2$ nanosheets exhibit band gaps of about 1.41 eV and (1.5-1.6 eV) respectively [4]. This wide band gap semiconductor is characterized by its excellent optical transparency, adjustable carrier concentration, and tunable electrical conductivity [5]. These characteristics make $MoSe_2$ highly attractive for application in optoelectronics, photovoltaics, photocatalysis, photodetectors, and chemical sensing [6, 7]. In its monolayer form, $MoSe_2$ exhibits a direct bandgap that enhances light- matter interactions and promotes strong absorption within the UV–visible region [8, 9]. Furthermore, its excellent thermal and chemical stability ensures reliable performance under harsh environmental conditions [10]. These combined features establish $MoSe_2$ as a promising candidate for advanced optoelectronic applications [11]. To further enhance the optical and electrical properties of $MoSe_2$, researchers have employed various innovative strategies such as metal or non-metal doping, layer-number control, heterostructure formation, strain engineering, plasmonic nanoparticle decoration, and surface functionalization [12, 13]. Among these approaches, hybridization with plasmonic nanostructures such as silver (Ag), gold (Au), and copper (Cu) nanoparticles has proven particularly effective due to their localized surface plasmon resonance (LSPR) effects, strong light-scattering ability, and high electrical conductivity [14]. When decorated on 2D MoSe2 nanosheets, plasmonic nanoparticle can induce synergistic interactions that modulate the band structure, promote charge transfer, and enhance light absorption across a broader spectral range. These hybrid effects are expected to significantly boost the performance of $MoSe_2$-based systems in optoelectronic devices, energy storage, optical detection platforms, and photocatalytic application.

In this this work we report a facile sonication-assisted method for the decoration of Ag nanoparticle onto $MoSe_2$ nanosheets to form $MoSe_2$-Ag nanocomposite. The synthesized hybrid system was systematically investigated to study the synergistic modulation of the optical bandgap and the enhancement of the optical properties of $MoSe_2$ nanosheets.

2 Materials and methods

2.1 Materials

Bulk $MoSe_2$(99.9%) was purchased from Thermo Scientific, N- Methyl-2-pyrolidone (NMP) was purchased from merck. Silver Nitrate ($AgNo_3$, 98.5%) was purchased from Loba Chemie and Sodium Borohydride ($NaBH_4$) from SRL.

2.2 Synthesis

$MoSe_2$ nanosheets were exfoliated from bulk $MoSe_2$ using Liquid Phase Exfoliation (LPE) method. It is an ultrasound-assisted technique where cavitation occurs and breaks the Van Der Walls cohesive forces between the layers to form exfoliated structures [15]. For the exfoliation of $MoSe_2$, a bath sonicator with an ultrasonic power 60 W was employed. Twenty milligrams of bulk $MoSe_2$ were dispersed in N-methyl-2-pyrrolidone (NMP) solvent followed by stirring and sonicated for 8 hours. The dispersion was further centrifuged at 7000 rpm for 20 min to separate the exfoliated nanosheets from the sediment. The sediment was washed several times and dried, after that added in DI water for further use.

The Silver nanoparticles (AgNPs) were synthesized from $AgNO_3$ by a chemical reduction method using Sodium Borohydride (NaBH4) as the reducing agent. Ten milliliters of 1 mM $AgNO_3$ solution were added drop wise to 30ml of 2mM freshly prepared $NaBH_4$. After complete reduction, a light brown colour Ag nanoparticle was obtained. To synthesize $MoSe_2$-Ag nanocomposite 20ml of exfoliated $MoSe_2$ dispersion and 20 ml of Ag nanoparticle suspension were mixed and sonicated for 3 hours to ensure uniform decoration of AgNPs on the $MoSe_2$ nanosheets.

3 Results and Discussion

The morphology of the exfoliated $MoSe_2$ nanosheets was examined using FESEM (JEOL). The sheets like layered structures were observed from the FESEM image (Fig. 1.a). The crystalline structure of bulk $MoSe_2$, exfoliated $MoSe_2$ and Ag-decorated $MoSe_2$ nanosheets ($MoSe_2$-Ag) were studied by P-XRD (`BRUKER AXS`). The diffraction peaks of bulk $MoSe_2$ (Fig. 1.c) are well indexed to the hexagonal phase (JCPDS card no. 29-0914), with prominent reflections corresponding to the (002), (004), (100), (103), (105), and (110) planes. These sharp and intense peaks confirm the high crystallinity of the bulk material. Some peaks are absent in exfoliated $MoSe_2$ which were present in bulk indicating a reduction in stacking order and the formation of few-layered nanosheets. Distinct Ag peaks are not observed in the $MoSe_2$–Ag nanocomposite, likely due to low Ag loading below the XRD detection limit or the formation of poorly crystalline Ag nanoparticles that produce weak, broadened diffraction signals. The energy dispersive X-ray spectroscopy (EDX) has been performed to identify the elemental composition of Mo, Se, and Ag (Fig. 1.d). The EDX spectra and the elemental mapping of Mo, Ag, and Se confirm the formation of $MoSe_2$-Ag nanocomposites. The smaller peaks below 1 keV are likely due to light elements such as carbon (C), oxygen (O), or nitrogen (N). These are commonly observed in EDX spectra and can originate from the sample environment, carbon tape, or minor surface contamination. The Raman spectroscopy shows the typical peaks of $MoSe_2$ nanosheets at 242 cm^{-1} and 289 cm^{-1}, which corresponds to the out-of-plane A_{1g} mode, in-plane E^1_{2g} mode [16]. Although the intensity of A_{1g} decreases in exfoliated nanosheets compared to the bulk $MoSe_2$, it increases again after incorporation of Ag nanoparticles. The optical properties of bulk $MoSe_2$, exfoliated $MoSe_2$ nanosheets and Ag-decorated $MoSe_2$ ($MoSe_2$-Ag) nanocomposite were investigated using UV–Vis spectroscopy, as shown in Fig 2. The two noticeable excitonic peaks, B($\sim$730nm) and A($\sim$836nm) are observed for bulk $MoSe_2$ which redshift to $\sim$706 and $\sim$807, respectively, for exfoliated $MoSe_2$. These arise from valence-band splitting caused by spin–orbit coupling, confirming the formation of few-layer 2H-phase $MoSe_2$ nanosheets [17]. Pristine $MoSe_2$ exhibits broad absorption across the UV–visible region, characteristic of its semiconducting nature and excitonic transitions associated with layered TMDCs. After Ag decoration, the $MoSe_2$-Ag nanocomposite exhibits enhanced absorption intensity, particularly in the visible region, along with a more pronounced feature around ∼420 nm. This enhancement is attributed to the localized surface plasmon resonance (LSPR) effect of Ag nanoparticles, which facilitates stronger light–matter interactions and improves photon harvesting. The increased absorbance also indicates effective electronic coupling between Ag nanoparticles and $MoSe_2$ nanosheets, promoting charge transfer and broadening the optical response. The optical bandgap was estimated (Fig. 2c-e) using the

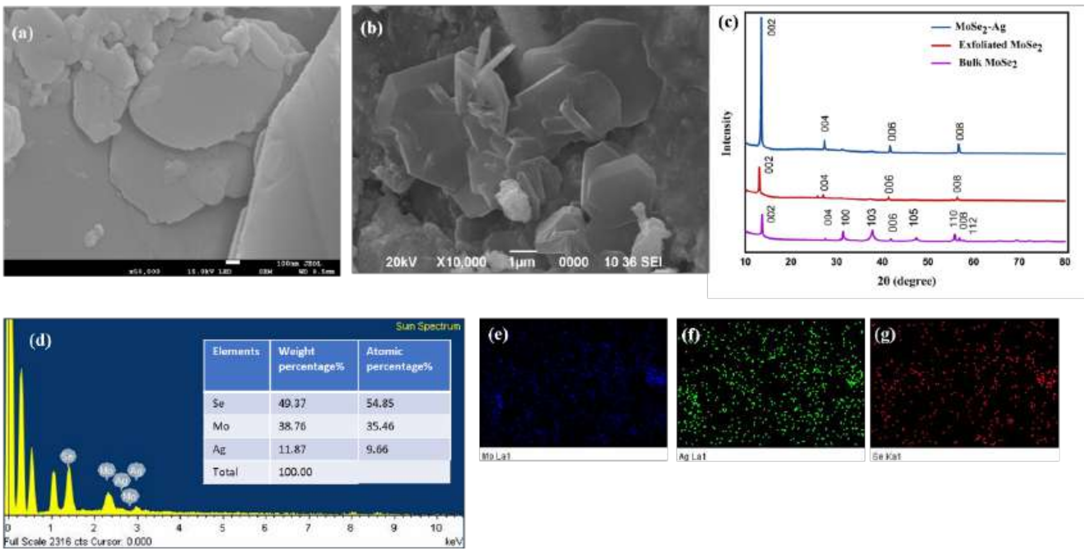

Figure 1: (a) FESEM image of exfoliated $MoSe_2$ nanosheets (b) SEM image of $MoSe_2$-Ag nanocomposite (c) XRD Spectra (d) EDX Spectra of $MoSe_2$-Ag nanocomposite (e)-(g) elemental mapping of Mo, Ag, Se respectively

Tauc relation

$$(\alpha h\nu)^x = A(h\nu - E_g) \tag{1}$$

Where $\alpha, h\nu, A, E_g$ are the absorption coefficient, photon energy, proportionality constant, and optical band gap, respectively. The value of x is $\frac{1}{2}$ for indirect transitions and 2 for direct allowed transitions. For bulk $MoSe_2$, the indirect band was estimated to be approximately 1.2eV, which increases to a direct bandgap of about 2.2 eV for exfoliated $MoSe_2$. Meanwhile, the $MoSe_2$-Ag nanocomposite exhibited a slightly reduced band gap of around 2.0 eV compared to pristine $MoSe_2$. This narrowing of the band gap upon Ag decoration can be attributed to strong interfacial interactions between $MoSe_2$ nanosheets and Ag nanoparticles. These interactions introduce additional electronic states and facilitate charge transfer, effectively lowering the transition energy. The decrease in band gap, along with enhanced optical absorption, indicates that Ag decoration successfully modifies the electronic structure of $MoSe_2$, enabling more efficient utilization of the visible spectrum. Such band gap engineering is advantageous for applications in optoelectronics, photocatalysis, and colorimetric sensing, where broad spectral absorption and efficient charge transport are crucial.

4 Conclusion

In this study, $MoSe_2$ nanosheets were successfully synthesized using the liquid-phase exfoliation (LPE) technique. Silver nanoparticles were incorporated through a sonication-assisted method to fabricate $MoSe_2$–Ag nanocomposites, resulting in a significant enhancement of their optical properties. The XRD confirmed the formation of few-layer $MoSe_2$ with uniformly dispersed AgNPs. UV–Vis spectroscopy revealed enhanced optical absorption due to the plasmonic effect of Ag, while Tauc analysis indicated a reduction in the optical bandgap from ∼2.2 eV to ∼2.0 eV after Ag incorporation. These findings demonstrate that Ag decoration effectively enhances light harvesting and tunes the electronic structure of $MoSe_2$, making the nanocomposite a promising material for optoelectronic, photocatalytic, and sensing applications.

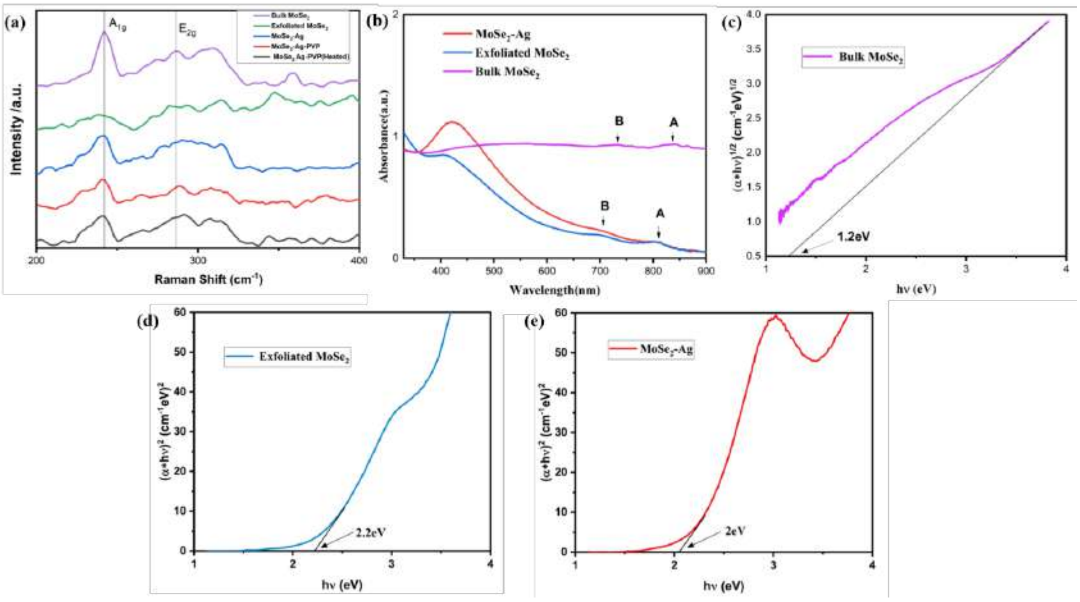

Figure 2: (a) Raman Spectroscopy, (b) UV-Vis Spectroscopy Tauc plot for (c) bulk $MoSe_2$ (indirect band gap) (d) exfoliated $MoSe_2$ (e) $MoSe_2$-Ag nanocomposite

Acknowledgements:

Authors would like to acknowledge SAIC Tezpur University for providing XRD and FESEM, EDX facilities. The authors also thank Dr. Pabitra Nath for providing access to the Raman Spectrometer. The authors would also like to give thanks to Dr. Rajib Biswas for providing the UV-Visible Spectrophotometer facility.

References

[1] T. Tan, X. Jiang, C. Wang, B. Yao, and H. Zhang, Adv. Sci. **7**, 2000058 (2020).

[2] A. Ghorai, S. K. Ray, and A. Midya, ACS Appl. Nano Mater. **4**, 2999 (2021).

[3] Z. Dehghani, F. Ostovari, and M. Nadafan, J. Appl. Phys. **131**, 213101 (2022).

[4] A. Arora, K. Nogajewski, M. Molas, M. Koperski, and M. Potemski, Nanoscale **7**, 20769 (2015).

[5] A. Chafai, I. Essaoudi, M. Behloul, A. Ainane, and C. A. Duque, Phys. B: Condens. Matter **651**, 414574 (2023).

[6] F. Zhong, J. Ye, T. He, L. Zhang, *et al.*, Small **17**, 2102855 (2021).

[7] A. Eftekhari, Appl. Mater. Today **8**, 1 (2017).

[8] G. S. Papanai, K. R. Sahoo, S. Gupta, and B. K. Gupta, RSC Advances **12**, 13428 (2022).

[9] F. Creazzo, ACS Applied Materials and Interfaces **17** (2025).

[10] J. Sun, K. Dai, W. Xia, W. Chen, K. Jiang, Y. Li, *et al.*, ACS Omega **6**, 30526 (2021).

[11] B. Babariya, D. Raval, S. K. Gupta, and P. N. Gajjar, Mater. Today Commun. **28**, 102614 (2021).

[12] K. Nam, J. Im, G. H. Han, J. Y. Park, H. Kim, S. Park, S. Yoo, *et al.*, ACS Omega **9**, 21587 (2024).

[13] K. Vasu, O. E. Meiron, A. N. Enyashin, R. Bar-Ziv, and M. Bar-Sadan, J. Phys. Chem. C **123**, 1987 (2018).

[14] J. Wu, Y. Lu, Z. Wu, S. Li, Q. Zhang, Z. Chen, and Q. Liu, Sens. Actuators B: Chem. **261**, 279 (2018).

[15] P. Sriram, A. Manikandan, F. C. Chuang, and Y. L. Chueh, Small **16**, 1904271 (2020).

[16] P. Tonndorf, R. Schmidt, P. Böttger, X. Zhang, J. Börner, A. Liebig, *et al.*, Opt. Express **21**, 4908 (2013).

[17] N. Dong, Y. Li, Y. Feng, S. Zhang, X. Zhang, C. Chang, and J. Wang, Sci. Rep. **5**, 14646 (2015).

UWB FILTERING USING HEXAGONAL HONEYCOMB SHAPED RESONATOR

Partha Protim Kalita[*1], Gouree Shankar Das[1], Akash Buragohain[1,2], Trishna Doloi[1], and Yatish Beria[1]

[1]*Microwave Research Laboratory, Department of Physics, Dibrugarh University, Dibrugarh-786004, Assam, India*
[2]*Department of Physics, Tingkhong College, Dibrugarh-786612, Assam, India*

[*]Corresponding Author: kalitapartha14@gmail.com

(Received 25 September 2025; revised 16 December 2025; accepted 22 December 2025; published 1 August 2026)

Abstract: Ultra-wideband (UWB) technology is a modern wireless communication system that uses a large amount of bandwidth. Due to its various advantages, such as high-speed data transfer, precise location detection, and secured communication, it has numerous applications in communication systems, medical imaging, automobile and radar systems etc. According to the Federal Communications Commission (FCC), in 2002, the unlicensed allowed frequency for UWB indoor and handheld applications is restricted within 3.1 GHz to 10.6 GHz. Hence, research is carried out to develop UWB filters, which are an important component of a UWB communication system to limit the frequency and reduce interference from other signals. This paper introduces a new UWB filter that uses a hexagonal honeycomb-shaped resonator. The hexagonal design not only saves space but also improves how the filter performs compared to traditional designs. Also, interdigital parallel coupled microstrip lines (PCML) are used to excite the resonator and to achieve the bandpass behaviour. We carefully designed the resonator's dimensions to achieve good performance, resulting in low insertion loss (IL) and a wide operational bandwidth. The passband of the designed filter spans from 3.14 GHz to 10.56 GHz with a fractional bandwidth of 108.32% and minimal signal loss. The filter is designed on a low-cost FR4 substrate with a dielectric constant of 4.4 and a thickness of 1.6 mm. The simulation of the filter is done using ANSYS High Frequency Structure Simulator (HFSS). Due to its compact and cost-effective design, this filter can be used in applications like communication systems and radar systems.

Keywords: UWB filter; PCML; Hexagonal resonator; Honeycomb shaped filter.

PACS: 88.80.ht, 84.30.Bv, 85.50.-n, 84.40.Dc

1 Introduction

In microwave communication systems, various components like antennas, filters, and low noise amplifiers (LNAs) are used to effectively and efficiently transmit the signals across the communication chain. Among these, filters are essential components that transmit only desired frequency signals through it while rejecting other signals. Filters can control the bandwidth, reduce noise, and improve signal integrity with enhanced performance [1, 2]. Filters can be used in a wide range of narrow-band applications like Bluetooth, Wi-Fi, and GPS for smooth signal transmission by blocking interference from outside sources [3]. But with the growth of the modern communication system, there is a need for a more stable, high-speed, high-capacity and secure system. To fill this void, ultra-wideband (UWB) technology emerges as a suitable technical evolution due to its high bandwidth capacity [4, 5]. Instead of using continuous radio waves, UWB technology uses a series of short-range and short-duration pulses to transmit signals wirelessly, making it a secure mode of communication [6]. These enable UWB technology with high data rates, precision in ranging, and imaging with low power uses, which makes it suitable for indoor, medical, and radar applications. Initially, UWB technology was used primarily for military purposes, particularly radar and secure communication [7]. But, in 2002, the U.S. Federal Communications Commission (FCC) formally allocated the unlicensed use of UWB for indoor and handheld devices in the frequency range from 3.1 GHz to 10.6 GHz with a strict power density limit of -41.3 dBm/MHz, thus creating a standardised spectral window for commercial development of UWB systems [8]. Since then, UWB has found significant use in short-range wireless networks, indoor localisation, biomedical imaging, vehicular radar systems, and next-generation IoT-enabled communication networks [9].

To operate UWB technology over a wide-ranging band, the UWB bandpass filter (BPF) plays a critical role by shaping the bandwidth (3.1-10.6 GHz), minimising insertion loss ($<$3dB), maintaining adequate return loss ($>$10dB), and providing strong out-of-band signal suppression [2, 10]. Although these filters can be theoretically implemented using lumped inductors, capacitors and resistors, it is not feasible for higher frequencies like microwaves and mm waves due to their fabrication limitation, parasitic effects and increased losses [11]. Hence, different distributed element technologies such as microstrip [12], co-planar waveguide (CPW) [13] and substrate integrated waveguide (SIW) [14, 15] are more suitable for UWB filter implementation. These technologies have gained attention due to their planar structure, ease of fabrication, low cost, and fabrication using printed circuit board (PCB) manufacturing. In microstrip technology, a single transmission line can exhibit inductor and resistor characteristics, which can help achieve the desired filtering response without the need for bulky lumped elements.

Over the past twenty years, numerous ultra-wideband filters have been developed utilising different design principles to increase their effectiveness and minimise size. One of the most common methods is using multi-mode resonators (MMR), which produce a series of different resonant frequencies within a single unit to cover a wide bandwidth [4]. Stepped impedance resonators (SIR) and stub-loaded resonators (SLR) have also been used to provide a more advanced filter response and increase control over the width of the passband [5]. Technologies such as using patterns within the ground plane, known as defected ground structures (DGS), or slight adjustments in the transmission lines, known as defected microstrip structures, have been widely used. These technologies suppress unwanted harmonics, increase filter selectivity, and provide strong rejection within the stopband area [18]. In [19], a quintuple-mode resonator for a UWB BPF has been designed, featuring a compact design with capacitively ended stubs and inter-digital coupled feed lines. An equivalent circuit analysis of the MMR-based UWB filter is performed and identified four resonant modes by coupling analysis in [20].

Alongside these techniques, there has been a focus on more sophisticated and innovative resonator geometries aimed at achieving reduced size and weight, while maintaining robust performance filters. Interdigital resonators, resembling a configuration of interleaved fingers, have demonstrated significant capability in providing effective electromagnetic coupling within an exceptionally compact structure, facilitating the generation of wideband responses without demanding extensive spatial requirements [21]. An alternative strategy involves the utilisation of periodically loaded microstrip lines, which incorporate small loading components positioned at uniform intervals along the transmission line. This configuration induces a slow-wave phenomenon, allowing the line to be shortened while achieving equivalent electrical length, thus resulting in marked miniaturisation and an expanded passband [22]. Researchers have expanded their focus beyond traditional rectangular configurations, embracing innovative geometrical forms. Hexagonal resonators are particularly appealing due to their distinctive shape, which facilitates enhanced spatial efficiency and improved frequency response management. Such geometries contribute to achieving compactness while simultaneously enhancing stopband effectiveness [23]. Similarly, structures inspired by fractals utilising recurring patterns at various scales have been utilised to develop filters with adjustable bandwidth and increased frequency attenuation that extends beyond the primary operating range [24].

In [25], a compact UWB filter using a multilayer printed circuit board (MPCB) structure with blind holes and a DGS to improve roll-off rates and in-band return loss. However, the design showed sensitivity to manufacturing tolerances and provided a relatively narrow fractional bandwidth (FBW) of 40.33%. Miniaturized balanced UWB filter on a high-temperature superconducting (HTS) substrate was designed using a composite right-/left-handed (CRLH) transmission line, which achieved an extremely low insertion loss of less than 0.2 dB [26]. A major limitation is the requirement for cryogenic operating temperatures (20 K), and the measured out-of-band rejection was worse than simulated due to fabrication imprecision. A reconfigurable filter is presented in [27] that uses pin diodes to switch between a UWB and a wideband response, achieving a large bandwidth switching range of 6.23 GHz. The drawback was a relatively high insertion loss of up to 1.6 dB and a low roll-off rate in its UWB mode, indicating reduced selectivity. In [28] UWB bandpass filter using a multi-stub-loaded short-circuited ring resonator was designed to generate five resonant modes and achieve a wide FBW of 108.9%. The design's coupling strength was noted to be limited by manufacturing capabilities, which contributed to discrepancies between simulated and measured results. A reconfigurable filter with three switchable quarter-wavelength stubs was designed, enabling five different passbands across four operational states. This versatility came at the cost of inconsistent performance, with some states exhibiting high insertion loss (up to 2.6 dB) and poor return loss [29]. In [30] a hybrid microstrip-to-CPW UWB filter was proposed that uses an MMR in the ground plane to generate multiple transmission zeros for sharp passband roll-offs. While the design achieves good selectivity, its measured insertion loss of up to 1.2 dB is relatively high for a non-reconfigurable filter of this type.

There are many ways to design UWB BPFs, but the existing research still shows some common problems. Many designs face trade-offs such as high insertion loss, low selectivity with slow roll-off, and unstable performance. This creates a clear gap for a UWB filter that can combine high selectivity, low insertion loss, and stable performance while still being simple, low-cost, and easy to manufacture. Using affordable materials like FR4 instead of expensive substrates such as Rogers can make the design much more practical and cost-effective for real-world applications.

In this work, a highly selective UWB BPF has been designed using an interdigital PCML and a honeycomb-shaped resonator. The parallel coupled lines have been modelled using admittance inverter method [31] and honeycomb shaped resonator consist of multiple hexagonal rings and hexagons. Two open stubs are also introduced to increase the selectivity of the filter as well as to increase out-of-band rejection. The filter is simulated and optimized using ANSYS High Frequency Structure Simulator (HFSS) within the frequency range 0.5 GHz to 20 GHz. The filter shows a very good performance in terms of insertion loss, return loss, group delay and out-of-band rejection. The filter has been able to achieve a wide passband from 3.14 GHz to 10.56 GHz along with a fractional bandwidth of 108.32%. Unlike most of the reported filters where expensive low loss substrate materials are used, this work uses high loss and cost-effective substrate material FR4, which can compete with traditional filters by showing high performance with effective and efficient signal transmission.

2 Design Methodology

The honeycomb shaped resonator based UWB BPF is designed in various steps. As the filer is designed using microstrip technology, a suitable substrate material must be selected first. Here, an FR4 substrate with dielectric constant 4.4 and loss tangent 0.02 is chosen due to its versatility, thermal stability and cost effectiveness. The height of the FR4 is taken to be 1.53 mm and a 0.035 mm width copper layer on both sides. A parallel coupled interdigital structure with a central transmission line is designed to achieve a bandpass behaviour using copper on the top layer of FR4 substrate, and the ground layer is filled with copper, as shown in Fig. 1. To excite these parallel coupled lines, 50Ω microstrip transmission line (feed line) is designed on both sides of the structure. The design parameters of this parallel coupled interdigital structure are evaluated using the admittance inverter (J-inverter) method [31, 32]. Then the design is modelled in HFSS software and it is simulated in the frequency range 0.5 GHz to 20 GHz. After optimisation, the dimensional values of width (w) and split gap (s) are found to be $w = 0.2mm$ and $s = 0.2mm$. The transmission (S_{21}) and reflection (S_{11}) characteristics of the filter have been extracted and plotted in Fig. 2. From the plot, it can be observed that the transmission characteristics shows a wide passband of 3 to 10 GHz with -3 dB bandwidth. However, the insertion loss in the passband is too high, and the reflection characteristics achieve a return loss less than 10 dB. Hence, the parallel coupled interdigital structure serves as an initial building block for the UWB BPF, but it needs to be improved in further steps.

Figure 1: interdigital microstrip coupled line structure.

The next step is to use a resonating structure to get a minimum insertion loss in the passband and a sharp transition (higher roll-off) between the passband and stopband. To get the final UWB BPF behaviour, the resonating structure has undergone various changes, shown in Fig. 3 and corresponding transmission and reflection characteristics in Fig. 4 and 5, respectively. A hexagonal ring-shaped structure is embedded in the central transmission line (Fig. 3(a)), resulting in lower insertion loss and higher return loss than the initial interdigital parallel coupled

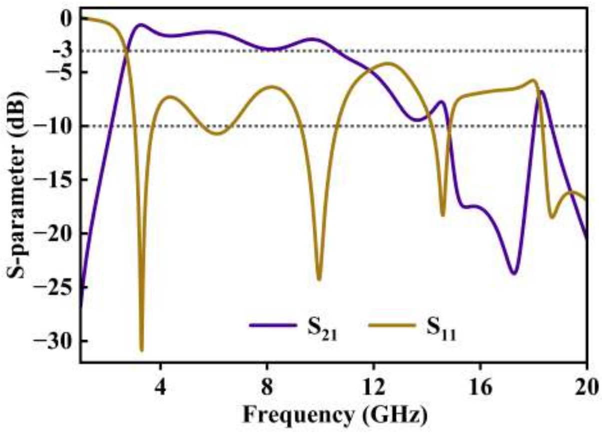

Figure 2: S-parameter response for interdigital coupled line structure.

structure. This structure also shows a lower out-of-band rejection and return loss of 10.37 dB, which needs to be improved in further steps. By using two hexagonal rings instead of a single ring as in Fig. 3(b), wider out-of-band rejection can be achieved, and return loss increases to 12.81 dB. These performances is further improved by adding two inductively coupled hexagonal solid structures in the intermediate space between hexagonal rings without touching the central transmission line, as shown in Fig. 3(c). The return loss found for this structure is 14.94 dB. In the next two steps, the whole structure is covered with hexagonal rings, $i.e.$ first using two more rings as shown in Fig. 3(d) and another four more rings as shown in Fig. 3(e). These neighbouring rings are inductively coupled with each other and the central transmission line. Due to the inclusion of multiple hexagonal rings, the structure looks like a honeycomb structure. This honeycomb structure minimises the insertion loss upto 0.5 dB and maximises the return loss upto 17.1 dB.

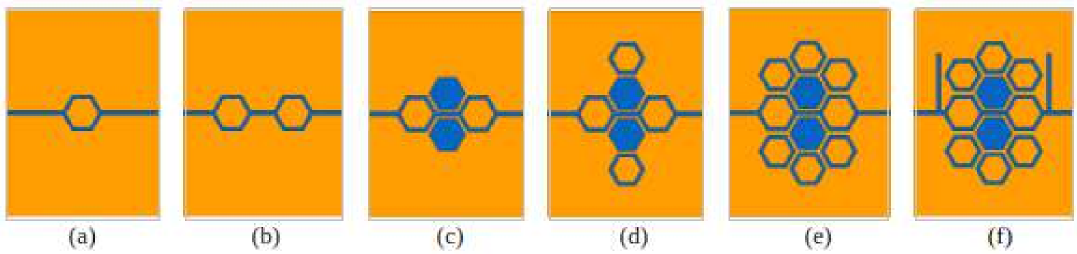

Figure 3: Evolution of the UWB filter.

Finally, at the last stage, two open stubs are placed on both sides of the honeycomb shaped resonator. The inclusion of stubs results in a sharper roll-off in the transition, higher return loss in the passband, and wide out-of-band rejection. These can be clearly observed from Figures 4 and 5. The open stub is optimised for multiple lengths and widths, for which various results are obtained. But the optimum result of s parameter is found at length p = 2.9 mm and width r = 0.2 mm.

The electromagnetic behaviour of the resonator geometry was further analysed using surface current distribution plots for square, circular, and hexagonal configurations, as shown in Fig. 6. It is observed that the hexagonal (honeycomb) resonator exhibits stronger and more uniformly distributed surface current compared to the square and circular structures. The inherent symmetry of the hexagonal structure promotes balanced current flow and stronger confinement of the electric and magnetic fields within the resonator, thereby reducing energy leakage and return loss. In contrast, the square geometry shows current crowding at the corners, resulting in localized field distortion, while the circular geometry exhibits relatively weaker coupling due to limited edge interaction. Consequently, the honeycomb configuration improves field uniformity, suppresses spurious modes, and enhances energy transfer efficiency between the resonator and the feed line, leading to wider bandwidth, lower insertion loss, and improved impedance matching compared to simpler geometries.

After optimising the results for honeycomb shaped resonator, the BPF has been analysed under weak and strong coupling between parallel coupled interdigital lines. This can be done by changing the length a of the

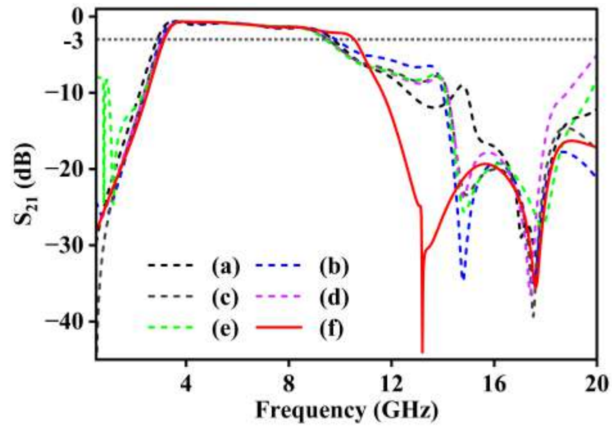

Figure 4: Variation in transmission characteristics.

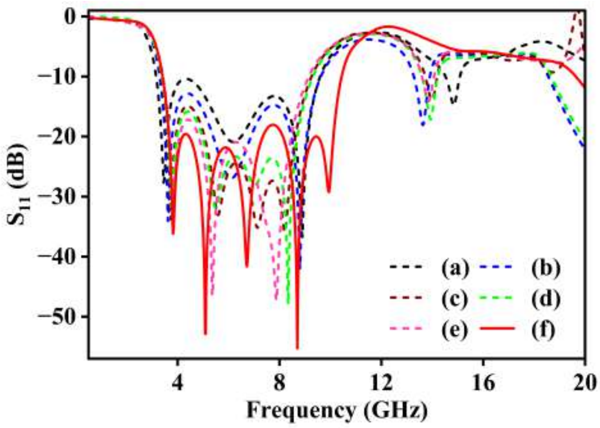

Figure 5: Variation in reflection Characteristics.

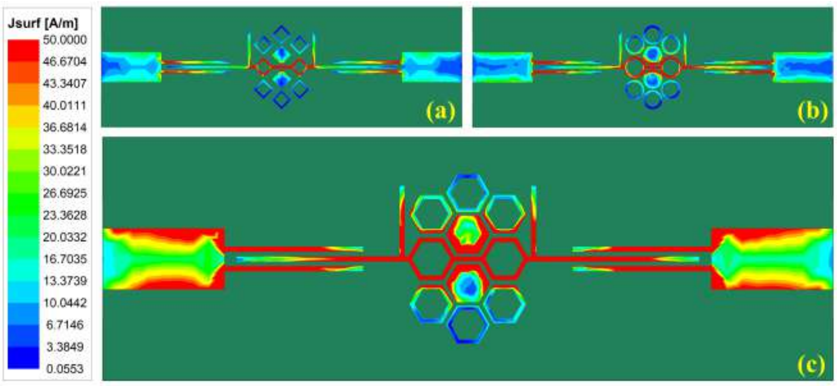

Figure 6: Surface current distribution for (a) Square shaped structure (b) Circular shaped structure (c) Hexagonal shaped structure.

parallel coupled lines. The S_{21} results obtained from this variation with 'a' are plotted in Fig. 7. The figure shows that under very weak coupling, the filter shows three resonant modes in 4.64 GHz, 7.10 GHz and 9.56 GHz, respectively. As we increase the coupling by increasing the length a, the insertion loss decreases and a minimum insertion loss of 0.39 dB is obtained for $a = 5.7$ mm. This happens due to the strong coupling between the coupled lines. Also, if we see analytically, a quarter wavelength ($\lambda_g/4$) transmission line gives the best result and strong coupling, where λ_g is the guided wavelength at the centre frequency of the BPF.

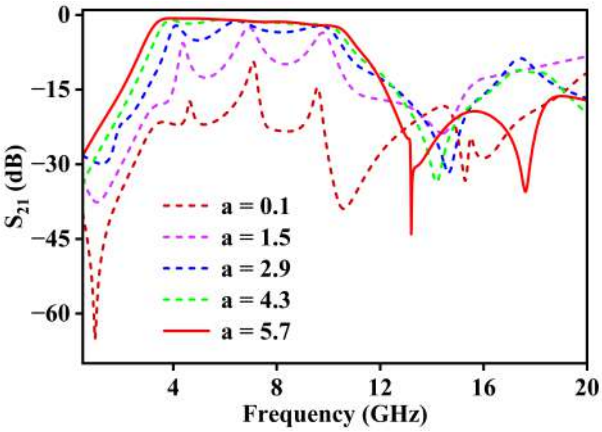

Figure 7: Honeycomb resonator under weak and strong coupling.

3 Results and Discussion

After going through numerous design changes through different steps, the optimised UWB BPF has been demonstrated in Figure 8. In the figure, the filter model is shown with two Sub-miniature version A (SMA) female connectors which will be later used for measurement. The overall dimension of the filter is very small, only $10 \times 30 \times 1.6$ mm^3 or 0.38×1.13 in terms of λ_g. The optimised dimensions of the filter for various parts in the structure are listed in Table 1.

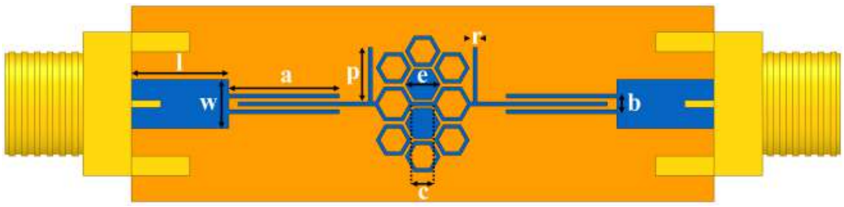

Figure 8: Final design of the UWB filter with ports.

Parameter	Dimension (mm)	Parameter	Dimension (mm)
a	0.2	l	5
b	1.0	p	2.9
c	1.1	r	0.2
e	1.8	w	2.5

Table 1: Optimised dimensions of UWB BPF

In the Fig. 9 the final transmission and reflection characteristics of the UWB filter is plotted within frequency range 0.5 GHz to 20 GHz. From the graph it can be observed that, a wide passband of 3.14 GHz to 10.56 GHz has been achieved by the UWB filter. The insertion loss and return loss in the passband are found to be 0.39 dB and 18.35 dB, respectively which are far better than most of the recently reported works. The bandwidth of the designed filter is 7.42 GHz with fractional bandwidth 108.32% at 6.85 GHz centre frequency. In addition to the wide passband characteristics, the proposed filter exhibits strong out-of-band suppression with steep roll-off at both band edges. Quantitative analysis shows that the stopband rejection levels are approximately -15.02 dB at 12 GHz, -20 dB at 12.86 GHz, -45 dB at 13.2 GHz, -35 dB at 17.5 GHz, and -17.12 dB at 20 GHz. This corresponds to a wide out-of-band rejection bandwidth of about 8 GHz, with minimum attenuation of 15 dB and maximum attenuation of 45 dB. The roll-off rate in the lower transition (1.44 GHz to 3.08 GHz) is 51.49 dB/decade, while in the upper transition (10.62 GHz to 12.86 GHz) it is 204.53 dB/decade. These results confirm the sharp skirt selectivity or sharp roll-off and strong stop band suppression of the proposed filter. To study the time delay between input and output ports, a frequency versus group delay graph is plotted in Fig. 10, where

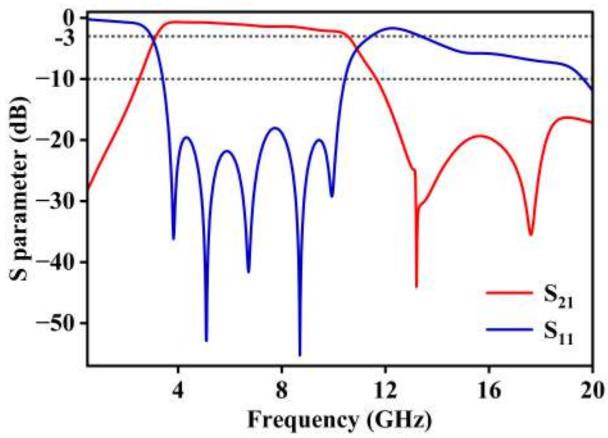

Figure 9: Simulated transmission and reflection Characteristics of UWB filter.

the group delay is taken in the unit nanosecond (ns). The plot shows that the group delay response is almost flat within the passband, around 0.25 ns to 0.3 ns. This shows a smooth and efficient transmission of input signals, maintaining signal integrity.

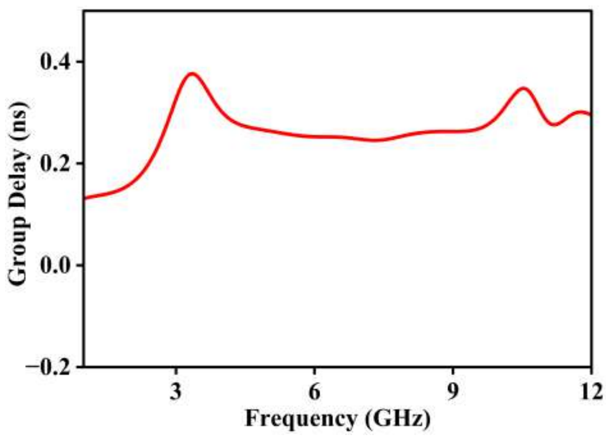

Figure 10: Group Delay of the UWB filter.

The passband and stopband characteristics of the filter can also be verified using surface current density (Jsurf) shown in Fig. 11. The surface current density for the UWB BPF is plotted for two frequencies, one for the centre frequency 6.85 GHz (Fig. 11(a)) and one for a frequency of 13 GHz from the stopband (Fig. 11(a)). From the figure, it can be clearly seen that the current density is uniform throughout the passband throughout the structure. On the other hand, for the stopband the current density vanishes halfway between the structure. From these observations, it can be concluded that the filter works perfectly in the whole frequency range.

To clearly highlight the effectiveness of the proposed honeycomb-shaped UWB filter, a comparative analysis with recently reported works is summarised in Table 2, which presents key parameters such as substrate used, operating passband, centre frequency (Cf), fractional bandwidth (FBW), insertion loss, return loss, group delay, and size of the filter. The table shows that most designs rely on advanced and costly substrates, such as Rogers-made RT/duroid to achieve wide passbands, sharp roll-off, and improved stopband rejection. While these works demonstrate excellent electrical performance, relying on expensive materials often limits their suitability for cost-sensitive applications. On the other hand, the honeycomb-shaped UWB filter presented here is implemented on a low-cost FR4 substrate, which is widely available and practical for mass production. Despite the intrinsic dielectric losses of FR4 at high frequencies, the proposed design successfully achieves a wide operating bandwidth and low insertion loss, comparable to or better than many state-of-the-art UWB BPFs.

As the objective of this work is to establish the design methodology and validate the proposed structure through simulation, all results presented are based on full-wave electromagnetic analysis. The fabrication of the filter and subsequent measurement using a Vector Network Analyzer (VNA) will be carried out in future to experimentally

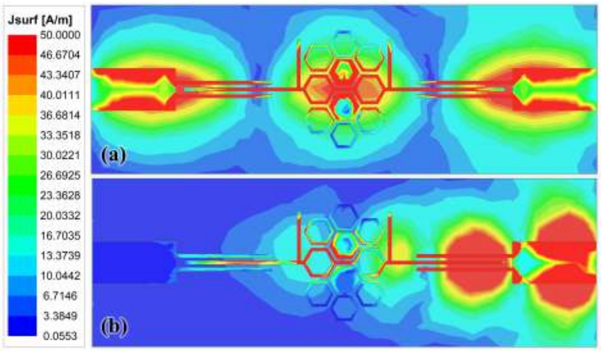

Figure 11: Surface current density at (a) 6.85 GHz and (b) 13 GHz.

confirm the simulated performance. During the practical fabrication of the proposed UWB filter, certain tolerances and material variations may slightly affect the final performance. The dielectric constant of the FR-4 substrate may vary at higher frequencies and the copper cladding thickness may differ due to manufacturing tolerances. Such variations can lead to minor shifts in the passband and small deviations in insertion loss. In addition, parasitic effect due to SMA connector and soldering imperfections may introduce additional losses during measurement. Environmental factors such as temperature and humidity may also cause slight performance fluctuations. These aspects have been considered during the design optimization process, and they will be further examined after prototype fabrication and experimental characterization.

Ref	**Substrate** (ϵ_r)	**Passband (GHz)**	C_f **(GHz)**	**FBW** (%)	**Insertion Loss (dB)**	**Return Loss (dB)**	**Group Delay (ns)**	**Size** ($\lambda_g \times \lambda_g$)
[13]	Rogers RT Duroid 5880 (2.2)	2.30–8.29	5.295	113	0.5	9.7	0.62	–
[19]	FR4 (4.4)	3.11–10.63	6.87	109.4	0.8	–	0.6	0.09×0.43
[25]	Rogers RO4003 (3.55)	3.49–11.04	7.265	103.92	1.95	6	1.73	0.38×1.04
[26]	MRO (9.78)	3.8–8.2	6	72.5	0.2	18.3	–	0.073×0.073
[28]	F4B-2 (3.3)	2.8–9.5	6.15	108.9	0.36	13	0.85	0.41×0.84
[33]	FR4 (4.3)	3–9.5	6.25	104	2	12	0.45	0.43×0.85
[34]	Roger 5880 (2.2)	3.05–10.8	6.925	112	0.5	13	0.8	0.45×0.60
[35]	Rogers RO3003 (3)	3.1–10.7	6.9	110	1.2	10.8	0.4	–
This work	**FR4 (4.4)**	**3.14–10.56**	**6.85**	**108.32**	**>0.39**	**>18.35**	**0.3**	**0.38×1.13**

Table 2: Comparison of this filter with recently reported works

4 Conclusions

In this work, a compact and highly selective UWB bandpass filter has been successfully designed and demonstrated to overcome common limitations in existing filter designs such as high insertion loss, poor selectivity, and reliance on costly substrates. The proposed filter combines interdigital PCML with a honeycomb-shaped resonator implemented on an economical FR-4 substrate, ensuring both performance and cost-effectiveness. The design achieves a wide operational passband ranging from 3.14 GHz to 10.56 GHz with a fractional bandwidth of 108.32%, while maintaining a minimum insertion loss of 0.39 dB and excellent selectivity characterized by sharp roll-off skirts. Additionally, the filter exhibits a flat group delay response across the passband, which guarantees high signal integrity for broadband applications. Moreover, the unique honeycomb geometry contributes to improved spatial efficiency and compactness. In contrast, other filters frequently employ multilayer configurations, defected ground structures, or fractal shapes to attain similar outcomes. This balance of performance, compactness, and cost-effectiveness establishes the honeycomb resonator filter as a strong alternative to existing solutions for real-world UWB communication systems. This study is presently based on design and full-wave simulation of UWB filter. The fabrication and measurement of the proposed UWB filter will be undertaken in future to experimentally validate its performance. Future research may also explore the integration of tunable notches for interference suppression, particularly for applications in cognitive radio and dynamic spectrum access systems.

Acknowledgements

The authors sincerely acknowledge the DST FIST (level-I) Project No (SR/FST/PSI-217/2016) and the DST PURSE Project No (SR/PURSE/2022/143) and funding by the Department of Science & Technology, Govt. of India to the Department of Physics, Dibrugarh University, Assam, India for financial assistance.

References

[1] J. Hong and M. J. Lancaster, *Microstrip Filters for RF/Microwave Applications*, 1st ed. (John Wiley & Sons Ltd, 2001).

[2] D. M. Pozar, *Microwave Engineering*, 4th ed. (Wiley, 2011).

[3] A. I. Zverev, *Handbook of Filter Synthesis* (Wiley-Interscience, 2005).

[4] X. Gao and L. Huai, Int. J. Ultra Wideband Commun. Syst. **4**, 57 (2020).

[5] P. P. Kalita *et al.*, *Advances in Microwave Engineering: From Novel Materials to Novel Microwave Applications*, edited by A. Bhattacharya *et al.* (CRC Press, Boca Raton, 2023), pp. 297–315.

[6] M. NoroozOliaei, in *Wideband Wave-Propagating Components for Wireless RF Communications*, edited by M. Alibakhshikenari (IntechOpen, 2025).

[7] H. Nikookar and R. Prasad, *Introduction to Ultra Wideband for Wireless Communications* (Springer Netherlands, Dordrecht, 2009), pp. 1–10.

[8] S. Yan, P. J. Soh, and G. A. E. Vandenbosch, IEEE Access **6**, 42177 (2018).

[9] F. Che *et al.*, Sensors **23**, 5710 (2023).

[10] P. P. Kalita *et al.*, in *2024 15th International Conference on Computing Communication and Networking Technologies (ICCCNT)* (IEEE, Kamand, India, 2024), pp. 1–6.

[11] A. Basit, A. Daraz, and G. Zhang, Micromachines **14**, 1986 (2023).

[12] F. M. Alnahwi *et al.*, Electronics **10**, 450 (2021).

[13] X.-F. Li and J.-K. Xiao, AEU - International Journal of Electronics and Communications **175**, 155100 (2024).

[14] Q. Li and T. Yang, IEEE Trans. Microwave Theory Tech. **69**, 65 (2021).

[15] S. Udhayanan and K. Shambavi, Prog. Electromagn. Res. Lett. **117**, 41 (2024).

[16] G. Saxena, P. Jain, and Y. K. Awasthi, Int. J. Microw. Wireless Technol. **13**, 999 (2021).

[17] M.-H. Weng *et al.*, Electronics **9**, 209 (2020).

[18] P. Chakraborty *et al.*, Prog. Electromagn. Res. M **108**, 89 (2022).

[19] P. P. Shome and T. Khan, Microsyst. Technol. **26**, 2295 (2020).

[20] B. Sahu, in *2020 6th International Conference on Signal Processing and Communication (ICSC)* (IEEE, Noida, India, 2020), pp. 71–73.

[21] S. M. A. Motakabber and M. N. Haidari, Int. J. Electr. Comput. Eng. **8**, 1654 (2018).

[22] C. Yang *et al.*, J. Phys.: Conf. Ser. **2480**, 012005 (2023).

[23] M. Popov *et al.*, Sci. Rep. **13**, 1179 (2023).

[24] N. Radhi and M. Fadhil, Int. J. Wirel. Mob. Networks **15**, 09 (2023).

[25] C. Li *et al.*, Electronics **12**, 1728 (2023).

[26] H. Tian, H. Liu, and Z. Song, IEEE Microw. Wirel. Technol. Lett. **33**, 1607 (2023).

[27] A. Bandyopadhyay, P. Sarkar, and R. Ghatak, IEEE Trans. Circuits Syst. II **69**, 2747 (2022).

[28] G. Wei, Y. Wang, J. Liu, and H. Li, ACES Journal, **38**, 496 (2023).

[29] S. Ramkumar and R. Boopathi Rani, AEU-Int. J. Electron. Commun. **151**, 154219 (2022).

[30] A. N. Ghazali, M. Sazid, and B. Virdee, Microw. Opt. Technol. Lett. **60**, 1925 (2018).

[31] P. P. Kalita *et al.*, AEU - Int. J. Electron. Commun. **191**, 155682 (2025).

[32] G. L. Matthaei, L. Young, and E. M. T. Jones, *Microwave Filters, Impedance-Matching Networks, and Coupling Structures* (Artech House, 1980).

[33] H. Louazene, M. Challal, and M. Boulakroune, Prog. Electromagn. Res. Lett. **109**, 75 (2023).

[34] M. Bod and S. M. Hashemi, IETE J. Res. **70**, 4415 (2023).

[35] K. Aliqab, Sci. Rep. **14**, 15669 (2024).

QUANTUM SUPPRESSION OF ION ACOUSTIC INSTABILITY IN DENSE PLASMA

Tonuj Deka*[1], Niranjan Gogoi[2], and Nilakshi Das[2]

[1]*Department of Physics, Tezpur College, Tezpur- 784001, Assam, India*
[2]*Department of Physics, Tezpur University, Tezpur- 784028, Assam, India*

*Corresponding Author: tonuj.tc@gmail.com

(Received 25 September 2025; revised 22 December 2025; accepted 24 December 2025; published 1 August 2026)

Abstract: A 1-D quantum hydrodynamics (QHD) model has been used to investigate the stability criteria of the ion-acoustic wave in a dense electron-ion quantum plasma. The ion-acoustic instability caused by electron streaming is well understood in classical plasma; however, when quantum effects are considered, the stability criteria undergo significant modifications. In the present work, electrons are described by the quantum fluid equation with $H = \frac{\hbar\omega_{pe}}{2k_BT_{Fe}}$ representing the quantum diffraction of the electron wavepacket. In classical plasma, even a small value of electron streaming velocity is enough to trigger ion acoustic instability; however, in presence of parameter H, a much higher value of electron streaming velocity is required to excite the instability. In this work, it is observed that the electron streaming contributes to the excitation of the instability, which gets suppressed due to the quantum effects of the electron, whereas the streaming ion provides energy to the wave mode.

Keywords: Quantum Plasma; Quantum Hydrodynamics; Quantum Ion Acoustic Wave

PACS: 52.35.-g; 61.10.Jn; 52.27.Cm

1 Introduction

Quantum plasma is a system of charged particles showing both collective and quantum effects [1]. Although the plasma is considered to be classical, the quantum mechanical behaviour of the constituent particles in a plasma are observed only at very large densities and relatively low temperatures in such a scenario, where the inter particle distance becomes almost equal to the de-Broglie wavelength [1, 2]. In such circumstances, the many particle system can be well defined by the Fermi Dirac statistics instead of Maxwell-Boltzmann statistics, preferably used in laboratory and space plasmas. However, the ions are considered to be nondegenerate due to their heavier masses as compared to the electron masses. Recently, quantum plasma has drawn immense interest due to its relevance in describing quantum effects observed in various environments such as in dense astrophysical objects [3], in ultrasmall electronic devices [4] and in intense laser plasma experiments [5].

During the last few decades, a great deal of interest has grown in the study of linear and nonlinear properties of electrostatic [6–9] and electromagnetic waves [10–12] in the quantum plasma. Haas et al. [6] utilized a nonlinear Schrodinger-Poisson system to develop a quantum multistream model and analysed the dispersion relations for plasma instabilities. They concluded that the reduced quantum effects in the plasma significantly amplify the two-stream instability. Manfredi et al. [7] derived an effective Schrodinger-Poisson model by taking the moments of the Wigner equation and applied it to investigate linear wave propagation and two-stream instability for a system of degenerate electron gas. Anderson et al. [13] did similar work to investigate various effects in quantum plasma using the Wigner-Poisson system. They demonstrated the suppression of instabilities in one and two stream plasma by a Landau-like damping mechanism. The characteristics of linear and nonlinear ion acoustic waves (QIAW) in a one-dimensional quantum plasma were investigated by Haas et al. [8] using the quantum hydrodynamic model (QHD). Ghosh et al. [14] too had used one-dimensional QHD model to investigate the linear and nonlinear properties of electron plasma waves in a two-dimensional quantum plasma. The QHD model is basically analogous to the classical fluid model containing a quantum correction term called the Bohm potential. Its simplicity and numerical efficiency have led to its usage in numerous linear and nonlinear studies of quantum waves in quantum plasma [15].

The streaming instability in various quantum plasma systems has attracted significant interest from researchers due to several fundamental reasons applicable to both laboratory settings and compact astrophysical environments [16]. In this present work, we have studied the linear wave characteristics of the quantum ion acoustic wave with electron and ion streaming in a quantum plasma in the core of white dwarf star. The dispersion relation of the quantum ion acoustic wave has been derived using a one-dimensional quantum hydrodynamics model. The model consists of the continuity equations, momentum equations with the Bohm potential term and Poisson's equation. The effect of the electron to ion mass ratio and quantum effects on the wave are also investigated here. We have further investigated the instability triggered by electron streaming velocity in the quantum regime of ion acoustic wave. In section 2, we present the QHD model used for our quantum plasma system in details. Section 3 deals with the results of this study and discussions were presented for the plasma in the white dwarf star's core. In section 4 we present the study of the instability triggered by the streaming electrons in the white dwarf plasma environment. Finally, section 5 contains the conclusion.

2 Theoretical Model

In this work, we consider a 1-D quantum hydrodynamic model to describe the propagation of a quantum ion acoustic wave in a two-component quantum plasma. Here, the ion mass provides the inertia while the restoring force is provided by the Bohm potential of the electrons and the degeneracy pressure. At very high density, the de Broglie wavelength of electrons becomes of the order of inter-particle separation. The quantum diffraction effect arising due to this wave nature of electrons is introduced to the system via the Bohm potential term. Electron and ion streaming velocities u_{e0} and u_{i0}, respectively, are included in the respective equations. Such flow may be important in quantum plasma system such as white dwarf, caused by accretion flow. This 1-D QHD model consists of continuity and momentum equations for the electrons and ions together with Poisson's equation for the self-consistent potential as described below:

$$\frac{\partial n_e}{\partial t} + \frac{\partial (n_e u_e)}{\partial x} = 0 \tag{1}$$

$$\frac{\partial n_i}{\partial t} + \frac{\partial (n_i u_i)}{\partial x} = 0 \tag{2}$$

$$\frac{\partial u_e}{\partial t} + u_e \frac{\partial u_e}{\partial x} = \frac{e}{m_e}\frac{\partial \varphi}{\partial x} - \frac{1}{m_e n_e}\frac{\partial P_e}{\partial x} + \frac{\hbar^2}{2{m_e}^2}\frac{\partial}{\partial x}\left(\frac{1}{\sqrt{n_e}}\frac{\partial^2 \sqrt{n_e}}{\partial x^2}\right) \tag{3}$$

$$\frac{\partial u_i}{\partial t} + u_i \frac{\partial u_i}{\partial x} = -\frac{e}{m_i}\frac{\partial \varphi}{\partial x} + \frac{\hbar^2}{2{m_i}^2}\frac{\partial}{\partial x}\left(\frac{1}{\sqrt{n_i}}\frac{\partial^2 \sqrt{n_i}}{\partial x^2}\right) \tag{4}$$

$$\frac{\partial^2 \varphi}{\partial x^2} = \frac{e}{\epsilon_0}(n_e - n_i) \tag{5}$$

Here n_i (n_e), u_i (u_e), m_i (m_e), e ($-e$) are the number density, velocity, mass and charge of the ions (or electrons) respectively and, $\hbar$ and ϵ_0 are the reduced Planck's constant and dielectric constant respectively. Here, 1-D system in the electrostatic approximation with potential φ is being considered. The last term on the right hand side of the Eqs. (3) and (4) is the Bohm potential term, the term related to the quantum diffraction effects present in the system.

Here, the following normalization are being used for further calculations: $\bar{t} = \omega_{pi} t$, $\bar{x} = \omega_{pi} x/c_s$, $\overline{n_e} = n_e/n_0$, $\overline{n_i} = n_i/n_0$, $\overline{u_e} = u_e/c_s$, $\overline{u_i} = u_i/c_s$, and $\overline{\varphi} = e\varphi/2k_B T_{Fe}$. Here, $\omega_{pi} = \sqrt{\frac{n_0 e^2}{m_i \epsilon_0}}$ is the ion plasma frequency n_0 is the equilibrium number density, k_B is the Boltzmann constant, T_{Fe} is the Fermi temperature, and $c_s = \sqrt{\frac{2k_B T_{Fe}}{m_i}}$ is the ion acoustic velocity. Along with these, the nondimensional quantum parameter H ($H = \frac{\hbar \omega_{pe}}{2k_B T_{Fe}}$, where $\omega_{pe} = \sqrt{\frac{n_0 e^2}{m_e \epsilon_0}}$ is the electron plasma frequency) is used to describe the quantum diffraction of the electron wavepacket. Physically, this quantum parameter H signifies the ratio of the electron plasmon energy to electron Fermi energy and measures the strength of the quantum diffraction effects.

Using the normalization parameters and dropping the bars, Eqs. (3) and (4) becomes

$$\mu\left(\frac{\partial u_e}{\partial t}+u_e\frac{\partial u_e}{\partial x}\right)=\frac{\partial\varphi}{\partial x}-n_e\frac{\partial n_e}{\partial x}+\frac{H^2}{2}\frac{\partial}{\partial x}\left(\frac{1}{\sqrt{n_e}}\frac{\partial^2\sqrt{n_e}}{\partial x^2}\right) \tag{6}$$

$$\frac{\partial u_i}{\partial t}+u_i\frac{\partial u_i}{\partial x}=-\frac{\partial\varphi}{\partial x}+\frac{m_e}{m_i}\frac{H^2}{2}\frac{\partial}{\partial x}\left(\frac{1}{\sqrt{n_i}}\frac{\partial^2\sqrt{n_i}}{\partial x^2}\right) \tag{7}$$

The ion momentum equation contains a Bohm potential term. However, we can neglect the term in the Eq. (7) for the ions with the argument that the quantum diffraction effects for the ions are negligible due to their heavier masses. Using Eqs. (5),(6), and (7), the dispersion relation for linear waves in the two-component quantum plasma is obtained, which is given by

$$1-\frac{1}{\mu(\omega-ku_{e0})^2-k^2\left(1+\frac{k^2H^2}{4}\right)}-\frac{1}{(\omega-ku_{i0})^2}=0 \tag{8}$$

Here $\mu=\frac{m_e}{m_i}$ is the ratio of electron to ion masses. The quantum parameter H introduces the additional dispersive effect to the propagation of the acoustic mode. The wave is further affected due to the presence of ion-electron streaming.

3 Results & Discussions

To understand the properties of the quantum ion acoustic wave, the dispersion relation is interpreted on the basis of typical parameters for the core of white dwarf star: quantum parameter $H\sim 0.3$ [17], fermi temperature $T_{Fe}\sim 10^5$ eV [17], ion temperature $T_i\sim 10^3$ eV [18]. The typical ion and electron streaming velocity are $u_{i0}\sim 0.06-0.07$ and $u_{e0}\sim 18.38-31.82$ respectively (as estimated from [19]). White dwarf stars go through several cooling phases after the completion of thermonuclear reactions such that the cores of such stars may attain mass density of $\rho\sim 10^6-10^7 gm/cm^3$, and temperature $T\leq 10^8K$. In such extreme conditions, the quantum effects become important for electrons, thus providing an ideal test bed for quantum ion acoustic wave. To understand the linear ion acoustic wave mode of the dense plasma in the white dwarf star, the dispersion relation is plotted for different quantum parameter *H*, electron and ion streaming velocities corresponding to the white dwarf environment. The dispersion relation given by Eq. (8) can be further simplified to

$$\omega(k)-ku_{i0}=k\left(\sqrt{\frac{4+k^2H^2-4\mu u_{e0}^2}{4+k^4H^2+4k^2(1-\mu u_{e0}^2)}}\right)=\omega'(k) \tag{9}$$

where both streaming electrons and ions play a significant role in the dispersion properties of the quantum ion acoustic wave. For small wavenumbers, $\omega\approx k$ suggests that a wave propagates in the system with the phase velocity, $v_p=\sqrt{\frac{4+k^2H^2-4\mu u_{e0}^2}{4+k^4H^2+4k^2(1-\mu u_{e0}^2)}}+u_{i0}$. This wave mode is analogous to the classical ion-acoustic wave mode and hence can be termed as quantum ion acoustic wave [8]. While ion streaming contributes via Doppler shifted frequency, electron streaming may excite streaming instability of the QIAW mode.

Fig. 1 shows the dispersion relation for the linear waves without the streaming electron and ion for three different values of quantum parameter *H*, namely *H* = 0, 0.5, 1.0. Similar to the classical mode, this quantum wave mode represents the electrons and ions oscillations at low frequency. Hence, at a smaller wavelength or at a larger wavenumber, the electrons and ions oscillate at the ion plasma frequency, ω_{pi}. Here, in Fig. 1, the curve corresponding to *H* = 0 represents the absence of any quantum effects due to high density in the white dwarf core, thus representing the classical ion acoustic wave. It is seen that with the increase of the parameter *H*, the wave reaches faster to the ω = 1 value. In absence of streaming, the results agree with those obtained by [8] in their study on quantum ion acoustic wave in quantum plasma. Here, the quantum ion acoustic wave describes the low-frequency density fluctuations near the ion plasma frequency $\omega_{pi}=3.30\times10^{14}$ Hz for the values of considered parameters. This is found to be significantly higher than the ion acoustic wave excited in laboratory plasma. In the limit u_{e0}, u_{i0}, $H\to 0$, Eq. (9) reduces to the usual IAW dispersion relation. Putting the above values in Eq. (9), the typical frequency of the QIAW is $0.77\omega_{pi}$ which is nearly equal to 2.55×10^{14} Hz for Oxygen ions of mass

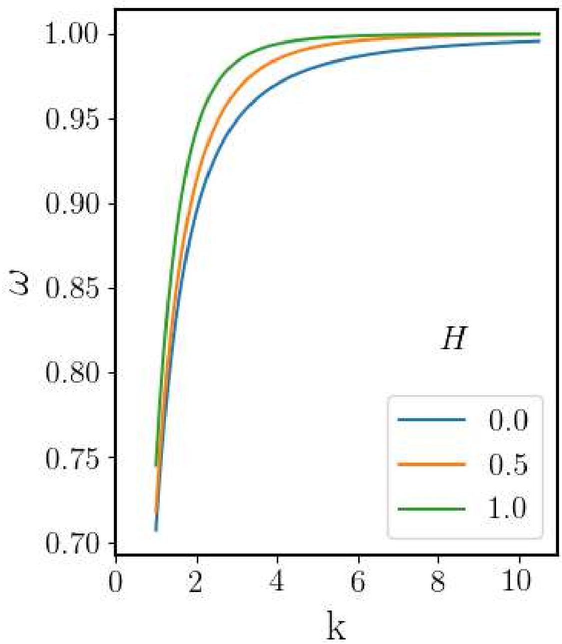

Figure 1: Dispersion relation for three different values of quantum parameter *H*, ($H \sim 0.0, 0.5, 1.0$) without any streaming electrons and ions in the white dwarf core plasma.

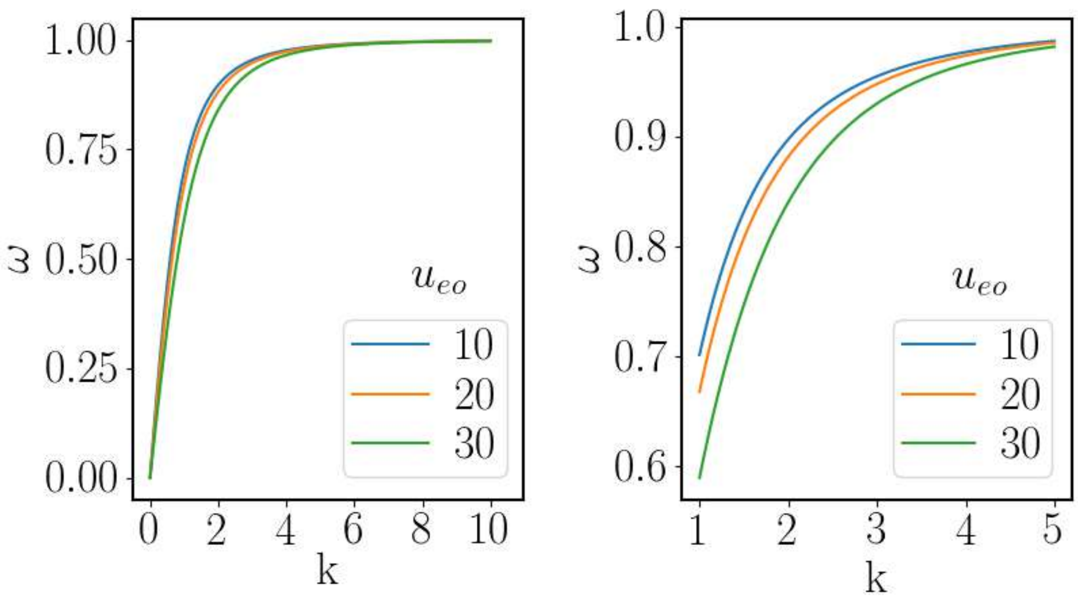

Figure 2: The image on the left panel shows dispersion relation with normalized electron streaming velocities $u_{eo} = 10, 20, 30$ and ion streaming velocity $u_{io} = 0$ for $H = 0.3$. The image on the right panel shows the zoomed image of the dispersive curve in the range $1 < \mathrm{k} < 5$.

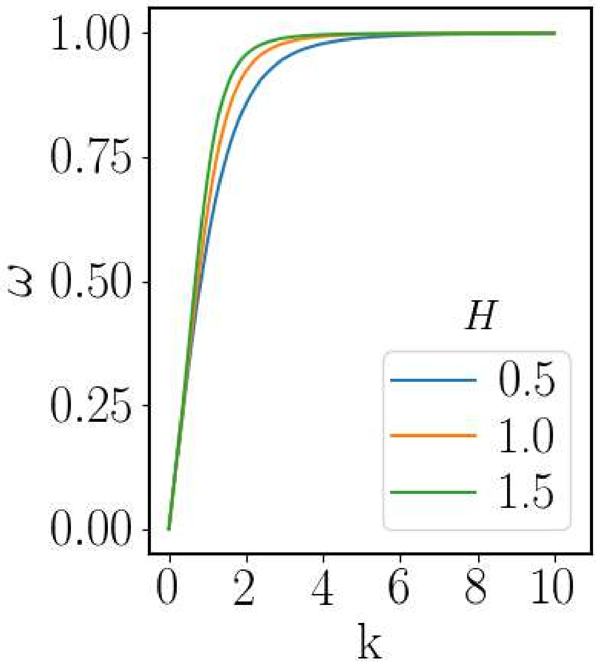

Figure 3: Dispersion relation with normalized electron streaming velocity $u_{e0} = 32$ and ion streaming velocity $u_{i0} = 0$ for $H = 0.5, 1.0, 1.5$.

2.66×10^{-26} kg and the number density considered is $10^{30} m^{-3}$. Hence, at a smaller wavelength or at a larger wavenumber, the electrons and ions oscillate at the ion plasma frequency, ω_{pi}.

We have seen that Eq. (8) and Eq. (9) contains both the electron and ion streaming velocities. The effect of the streaming electrons on the quantum ion acoustic wave mode is presented in Fig. 2. To verify this effect, we have considered three values of the normalized electron streaming velocity $u_{eo} = 10, 20, 30$, and neglected the ion streaming velocity ($u_{io} = 0$). Here, the dispersion relation is plotted for the parameter *H* = 0.3. It is observed in Fig. 2 that as the electron streaming velocity increases, the slope of the dispersion curve decreases, thereby suggesting a decrease of the wave velocity. This effect of the increase of the electron streaming velocity is clearly visible in the right-hand image of Fig. 2. Moreover, these streaming electrons have no effect on the influence of the parameter *H* on the wave mode. The influence of the increase of *H* on the quantum ion acoustic wave is the same even in the presence of the streaming electrons, as evident from Fig. 3. Fig. 3 shows the dispersion relation considering streaming electrons with the streaming velocity $u_{eo} = 32$ and neglecting the ions streaming for three different values of $H = 0.5, 1.0, 1.5$.

The effect of the streaming ions on the quantum acoustic wave mode is also investigated. Ignoring the electron streaming velocity, we have plotted the dispersion relation taking the ion streaming velocities $u_{io} = 0.0, 0.06, 0.07$ and the parameter $H = 0.3$ in Fig. 4. When the ion streaming velocity is considered, the wave no longer saturates and continues its propagation. As the wavenumber k increases, the wave frequency keeps on increasing. This can be considered to be due to the fact that as the velocity of the streaming ions increases, these ions provide energy to the wave propagation; as a result, the wave no longer saturates at the ion plasma frequency and keeps on propagating. However, at $u_{i0} = 0$ i.e. in the absence of the streaming ions, the wave saturates similarly to the normal ion acoustic wave.

The impact of the quantum parameter on the wave mode in the presence of the streaming ions is also investigated. Here, the dispersion relation of the wave is plotted in Fig. 5 for three different values of the parameter $H = 0.5, 1.0, 1.5$ with normalized ion streaming velocity $u_{io} = 0.06$ and negligible electron streaming velocity $u_{eo} = 0$. Fig. 5 shows the effect of the streaming ions i.e. the bending of the saturation curve, along with the effect of the increase of the parameter *H*. Similar to the case of no streaming, the wave here reaches faster to the $\omega = 1$ value with the increase of the parameter, even with the streaming ions.

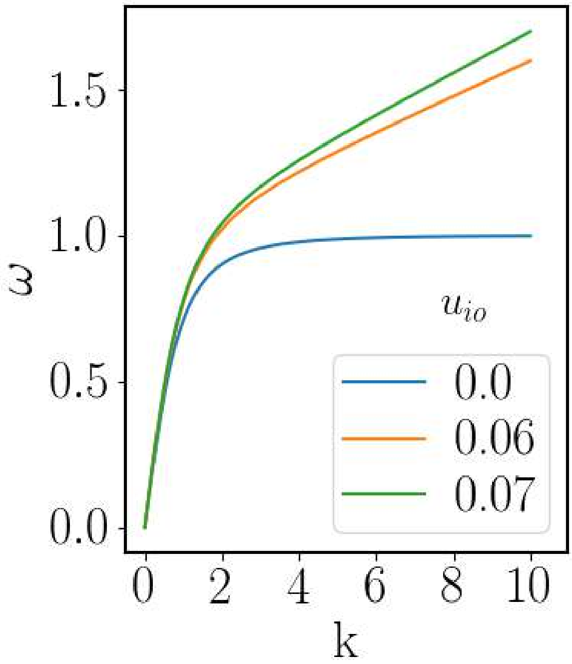

Figure 4: Dispersion relation with normalized ion streaming velocities $u_{io} = 0.0, 0.6, 0.7$ and electron streaming velocity $u_{eo} = 0$ for $H = 0.3$.

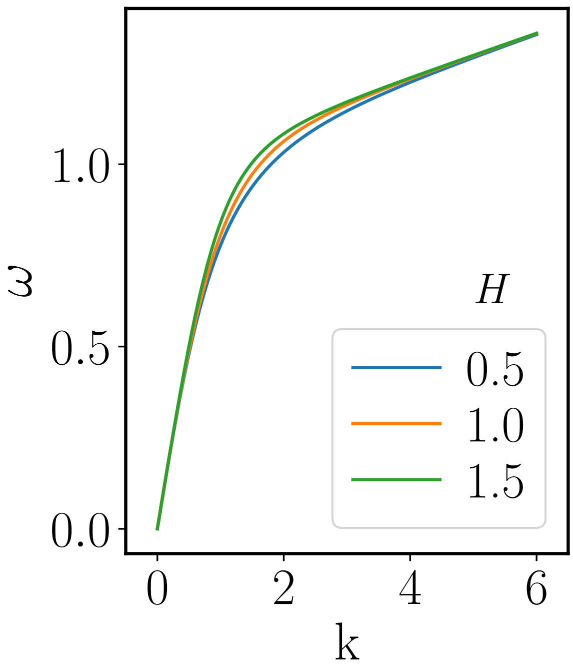

Figure 5: Dispersion relation showing the effect of the increase of the quantum parameter H ($H \sim 0.5, 1.0, 1.5$) on the wave mode in the presence of the streaming ions with normalized streaming velocity u_{io}= 0.06 and electron streaming velocity $u_{e0} = 0$.

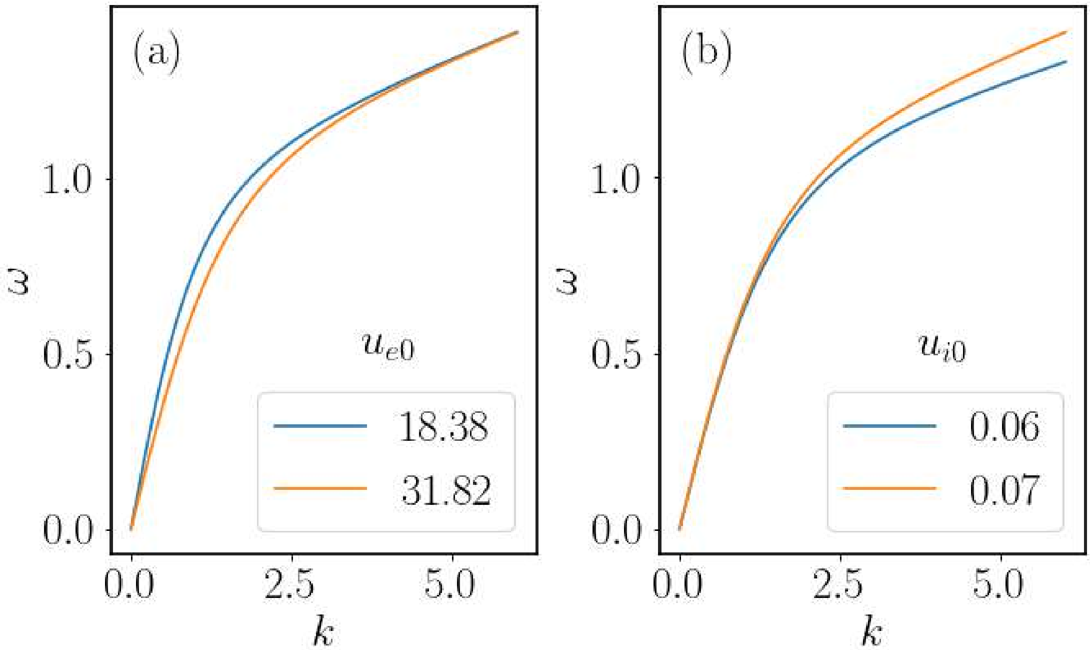

Figure 6: Dispersion relation with normalized electron and ion streaming velocities for (a) $u_{io} = 0.07$ and $u_{eo} = 18.38, 31, 82$, (b) $u_{eo} = 31.5$ and $u_{io} = 0.06, 0.07$.

The combined effect of electron and ion streaming velocities on the quantum ion acoustic wave mode can be seen from the plots of Figs. 6 (a) and 6 (b). The ion streaming velocity mainly contributes towards adding a constant velocity to the phase velocity of the wave mode. On the other hand, small values of u_{e0} have only a negligible effect on the dispersion curve. The electron streaming velocity starts affecting the wave significantly only in the presence of streaming ions and the effect is mainly revealed in the long wavelength regime (lower value of wavenumber). The role of electron streaming is further investigated in the next section in the context of streaming-induced instability in the presence of quantum effects. In Fig. 6 (a) the dispersion relation is shown for two values of the electron streaming (u_{e0} = 18.38 and 31.82), considering constant ion streaming velocity ($u_{i0} = 0.07$). It has been observed that at sufficiently high electron streaming velocities, a change in the velocity can decrease the slope of the curve, hereby suggesting that with the increase of the streaming velocity of the electrons, the phase velocity of QIAW decreases. Fig. 6 (b) is plotted for two values of ion streaming velocities $u_{io} = 0.06$ and 0.07 and electron streaming velocity $u_{eo} = 31.5$. Here, it is observed that as ion streaming velocities increase, the wave no longer saturates. In both the situations (Fig. 6 (a) and 6 (b)) the common phenomenon observed is that in the presence of both electron and ion streaming velocities, the wave no longer saturates, and as wavenumber k increases, the wave frequency keeps on increasing.

4 Stability Analysis

An analysis of the dispersion relation Eq. (9) gives important insight into the role of electron streaming on the instability of quantum ion acoustic wave mode. It has been observed that the quantum parameter H has a stabilizing effect, whereas electron streaming may trigger the instability. A straightforward analysis of Eq. (9) gives the boundary of the unstable regime as $1 + \frac{1}{4}k^2H^2 < \mu u_{e0}^2 < 1 + \frac{1}{k^2} + \frac{1}{4}k^2H^2$. Fig. 7 depicts the boundaries of the unstable regime in the $(\mu u_{e0}^2 - k)$ plane for various values of parameter H. For a higher value of H, a higher value of electron streaming velocity u_{e0} is required to trigger the instability. The above boundary condition for the unstable region may be stated in terms of the quantum parameter H as $4(\mu u_{e0}^2 - 1) - \frac{4}{k^2} < k^2H^2 < 4(\mu u_{e0}^2 - 1)$. At $k = 1$, the condition may be written as $4(\mu u_{e0}^2 - 2) < H^2 < 4(\mu u_{e0}^2 - 1)$. This implies a cut-off value of μu_{e0}^2 as 2 to trigger the instability. When μu_{e0}^2 attains the cutoff value, the boundary condition for the unstable regime at $k = 1$ may be stated as $0 < H < 2$. In the core of white dwarf stars with $n_0 = 10^{30}/cm^3$ and $T_{Fe} \sim 10^5$ eV, the plasmon energy becomes $\hbar\omega_{pe} \sim 3.5 \times 10^4$ eV so that $H \approx 0.3$, thus satisfying the condition.

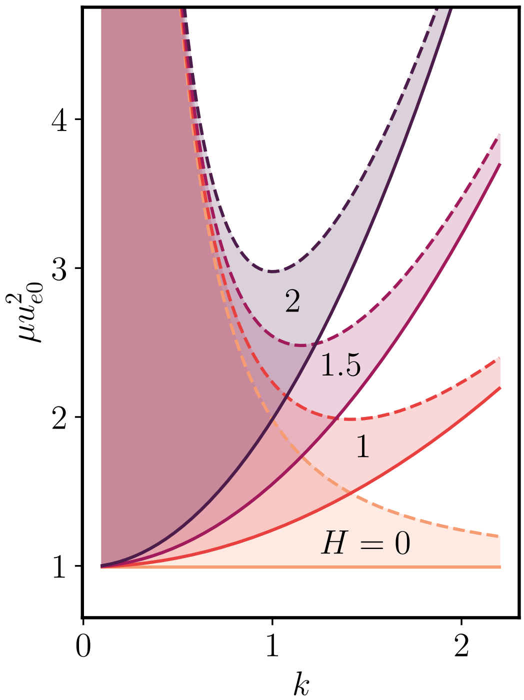

Figure 7: Stability curve of quantum ion acoustic wave in white dwarf plasma environment. The shaded parts denote the unstable region in the ($\mu u_{e0}^2 - k$) parameter space for various values of H.

5 Conclusions

A 1-D quantum hydrodynamic model is used in this work to study the role of electron and ion streaming on the characteristics of the ion acoustic wave's dispersion relation in the dense plasma, where quantum effects become dominant for the lighter species of plasma. The results are tested in the quantum plasma that may exist in the core of white dwarf star. It has been observed that in the presence of the streaming ions, the wave no longer saturates at the ion plasma frequency. The wave frequency is found to increase with the increase of the wave number. It appears as if the streaming ions are providing energy to the wave, as a result, it no longer saturates.

A stability analysis is carried out for the streaming-induced instability of the quantum ion acoustic wave. The lower and upper boundaries of the reduced electron streaming velocity, viz. μu_{e0}^2 is derived in terms of the quantum parameter H. While the electron streaming triggers the instability, the quantum parameter H has a stabilizing effect. The higher the value of H, the higher μu_{e0}^2 is required to trigger the instability. The electron streaming induced instability may be triggered in quantum plasma when energy associated with the collective oscillations of electrons is within the limit of Fermi energy for $k \sim 1$. For higher value of wave vector k i.e. low wavelength regime, the range of H is reduced to excite the instability. The results may give an important clue to the investigation of ion acoustic mode in the interaction of an electron beam with dense laser plasma or astrophysical quantum plasma.

Acknowledgements

Niranjan Gogoi gratefully acknowledges the University Grants Commission (UGC), New Delhi-110002, for the financial support provided during the research under the Junior Research Fellowship (JRF) scheme, Ref no.: 221610069839.

References

[1] F. Haas, *Quantum Plasmas: An Hydrodynamic Approach* (Springer Science & Business Media, New York, 2011).

[2] F. Haas, Braz. J. Phys. **41**, 349 (2011).

[3] M. Opher et al., Phys. Plasmas **8**, 2454 (2001).

[4] P. A. Markowich, C. A. Ringhofer, C. Schmeiser, *Semiconductor Equations* (Springer Science & Business Media, New York, 2011)

[5] M. Marklund and P. K. Shukla, Rev. Mod. Phys. **78**, 591 (2006).

[6] F. Haas, G. Manfredi and M. Feix, Phys. Rev. E **62**, 2763 (2000).

[7] G. Manfredi and F. Haas, Phys. Rev. B **64**, 075316 (2001).

[8] F. Haas *et al.*, Phys. Plasmas **10**, 3858 (2003).

[9] P. K. Shukla and B. Eliasson, Phys. Rev. Lett. **96**, 245001 (2006).

[10] P. K. Shukla, Phys. Lett. A **369**, 312 (2007).

[11] P. K. Shukla and L. Stenflo, Phys. Plasmas **13**, 044505 (2006).

[12] C. Li *et al.*, Phys. Plasmas **21**, 072114 (2014).

[13] D. Anderson *et al.*, Phys. Rev. E **65**, 046417 (2002).

[14] B. Ghosh, S. Chandra and S. N. Paul, Phys. Plasmas **18**, 012106 (2011).

[15] S. A. Khan and M. Bonitz, in *Complex Plasmas: Scientific Challenges and Technological Opportunities* (Springer, Cham, 2014).

[16] F. Cap et al., *Waves and Instabilities in Plasmas* (Springer, Vienna, 1994).

[17] P. K. Shukla and B. Eliasson, Rev. Mod. Phys. **83**, 885 (2011).

[18] V. E. Fortov, Phys.-Usp. **52**, 615 (2009).

[19] M. Rosenberg, J. Plasma Phys. **67**, 235 (2002).

ASSESSING THE EVAPOTRANSPIRATION OVER DIFFERENT STATES OF NORTH-EAST INDIA USING SATELLITE BASED DATA

Anindita Borah[1*] and Binita Pathak[1,2]

[1]*Department of Physics, Dibrugarh University-786004, Assam, India*
[2]*Centre for Atmospheric Studies, Dibrugarh University, Dibrugarh-786004, Assam, India*

*Corresponding Author: borahanindita97@gmail.com

(Received 25 September 2025; revised 11 December 2025; accepted 3 January 2026; published 1 August 2026)

Abstract: Evapotranspiration (ET) plays a crucial role in the hydrological cycle and shifts in its pattern can directly influence the availability and distribution of water resources within the concerned region. The contribution of ET varies from place to place, reflecting land cover heterogeneity. As such, the present study analyses climate change and its effects on the hydrological cycle through investigating the variation of water budget-derived ET in different states of North-East India (NEI). The MODIS satellite retrieved ET dynamics exhibits an increasing trend at a rate of 3.28 mm/year over NEI during 2000-2021. The highest ET (>1000 mm/year) is observed in the states with more forest cover: Manipur, Mizoram, Nagaland and Tripura while, Arunachal Pradesh exhibits the lowest ET (698 - 812 mm/year) because some of its mountains are covered with snow and owing to its latitudinal positions. Trend analysis exhibits a significant rise in annual ET across Assam (4.26 mm/year), Manipur (3.58 mm/year), Meghalaya (3.71 mm/year), Mizoram (5.36 mm/year), Nagaland (3.58 mm/year) while in Arunachal (1.37 mm/year) and Tripura (5.06 mm/year) the observed trends are insignificant, which are evaluated by Mann-Kendall Test. The analysis reveals that the highest ET occurs in monsoon season in all the states and lowest in the winter season. Most of deciduous plants reached its maximal growth during high ET season that coincided with highest amount of rainfall and sufficient soil moisture. This study highlights the importance of considering vegetation and geographical position in analyzing ET.

Keywords: Evapotranspiration, North-East India, MODIS satellite, Mann-Kendall test.

PACS: 92.40.-t, 92.70.Np, 92.60.hf

1 Introduction

Evapotranspiration is the process through which water is transferred from land to the atmosphere, combining evaporation from water bodies and soil surface along with transpiration from plants [1, 2]. It is a key component of the hydrological cycle, influencing agricultural productivity, soil moisture availability, drought occurrence and regional hydrological balance. The major meteorological parameters influencing ET are temperature, precipitation, solar radiation, relative humidity, wind speed, soil moisture *etc.* [3–6]. Topography and elevation are also two key factors which strongly affect the regional conditions of the study domain. Seasonal and inter-annual variation of ET are key regulating factors of terrestrial hydrological processes, vegetation dynamics, surface energy fluxes, climate variability and regional water balance. Therefore, ET responds differently to climatic variables in different places under different climatic conditions. So, accurate estimation of ET in different places is critical for forecasting actual crop evapotranspiration, irrigation scheduling, water management, climate modelling, and other practices of agricultural productivity and prediction of extreme events like drought [7, 8]. As such, this study focuses on investigating the trends of evapotranspiration in different states of North- East India (NEI).

However, the network of ground-based ET observations is limited, discontinuous and difficult to scale up, particularly in areas like NEI, which is a topographically complex region. In the absence of long-term ground-based

ET observations in NEI, satellite-based products provide the only consistent source of regional ET information. While these datasets are subject to uncertainties arising from cloud cover, complex terrain and heterogeneous land cover, they nevertheless provide valuable spatially continuous estimates. Satellite-based remote sensing has emerged as a powerful approach for monitoring ET across large spatial and temporal scales. These products integrate multi-sensor observations of radiation, temperature, vegetation indices and soil moisture with land surface models to provide spatially continuous ET values. Such data are especially valuable in regions with limited ground measurements, enabling inter-comparison and trend analysis across complex terrain.

Several global studies have utilised MODIS, GLEAM, ERA5-Land products to assess spatial patterns, seasonal variability and trends in ET for different river basins and agro-climatic zones [9–13]. Some Indian researchers have found that ET trends vary regionally due to monsoon variability, land-use change, irrigation and vegetation dynamics and with high uncertainties where ground observations are sparse. ET estimation and validation in NEI is challenging due to sharp elevation gradients, dense forest cover, highly variable monsoonal precipitation and limited ground-based observation station. Jhajharia et al. observed the reference evapotranspiration is decreased in humid region of NEI due to net radiation and wind speed [14]. This motivates the present study to perform a systematic, state-wise ET assessment for NEI, quantifying seasonal variation in different states using satellite-based data products. Such analysis is essential for assessing regional water balance, agricultural water use and climate change impacts.

2 Study area

The study focuses on the NEI region, which comprises eight states: Arunachal Pradesh, Assam, Manipur, Meghalaya, Mizoram, Nagaland, Tripura and Sikkim. Geographically, the region is located at the easternmost part of India, spans an area of approximately 2,62,179 square kilometres, accounting for 7.97% of the country's total geographical area [15]. NEI region is predominantly hilly and mountainous, except for the Brahmaputra and Barak River valleys in Assam and low-lying plains of Tripura. The region comprises of some of the wettest places on Earth, such as Cherrapunji and Mawsynram in Meghalaya. They receive more than 10,000 mm rainfall annually [16]. Climatologically, the region experiences four distinct seasons: pre-monsoon (March-May), monsoon (June-September), post-monsoon (October-November) and winter (December-February) season with abundant rainfall of 1500-6000 mm during monsoon season. The region is characterized by dense vegetation, rich biodiversity and variety of land cover types - from evergreen forests and grasslands to agricultural croplands and wetlands. Altitude variation, vegetation and climatic patterns making NEI an ecologically sensitive and hydrologically complex region.

3 Data and Methods

3.1 Data description

ET data are provided by various satellite based and reanalysis datasets, which serves as an alternative in areas where in-situ observations are limited. NEI region has only a few numbers of monitoring stations. This limited data of ET does not accurately reflect the overall scenario of the region. In the present study, ET product over the study domain is obtained from the time-series MODIS 8-day products (MOD16A2) with spatial resolution of 500m during 2000-2021 (`https://modis.gsfc.nasa.gov/data/`). This data product has been extensively validated and widely used across the globe [17, 18].

MOD16 algorithm is based on the Penman-Monteith equation which integrates meteorological inputs and vegetation information derived from MODIS. We adopted the approach proposed by [19],

$$\lambda E = \frac{sA' + \rho C_p \frac{e_{\mathrm{sat}}-e}{r_a}}{s+\gamma\left(1+\frac{r_s}{r_a}\right)} = \frac{sA' + \rho C_p \frac{\mathrm{VPD}}{r_a}}{s+\gamma\left(1+\frac{r_s}{r_a}\right)}. \tag{1}$$

where, s denotes the slope of the curve describing the relationship between saturated vapor pressure (e_{sat}) and temperature, mathematically expressed as $\frac{d(e_{sat})}{dT}$; VPD is calculated as $e_{sat} - e$, where e is the actual air vapor pressure, λE refers to the latent heat flux, A' indicates the amount of available energy on land surface, ρ is air density and C_p represents the specific heat capacity of air. Here, r_a and r_s refers aerodynamic resistance and surface resistance respectively which are the key factors for evaporation.

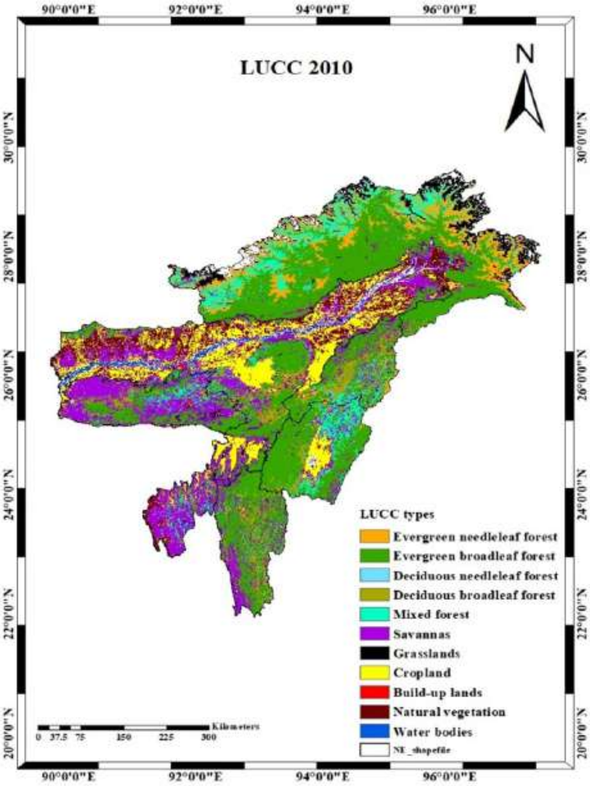

Figure 1: Land Use and Land Cover map of NEI for the year 2010.

3.2 Methodology

A non-parametric Mann-Kendall (MK) test was employed to identify the presence and extent of trends in ET over different states of NEI. This test is widely used in hydro-climatic studies since it does not rely on normally distributed data and is relatively less sensitive to missing values or outliers. It evaluates whether the data exhibit a monotonic increasing or decreasing trend over time. The test statistic (S) is computed as follows,

$$S = \sum_{i=1}^{n-1} \sum_{j=i+1}^{n} \mathrm{sgn}(x_j - x_i) \tag{2}$$

Here, n represents the total number of observations, x and x denote the data values in time series i and $j(j > i)$, respectively.

$$Z = \begin{cases} \dfrac{S-1}{\sqrt{\mathrm{Var}(S)}}, & \text{when } S > 0, \\ 0, & \text{when } S = 0, \\ \dfrac{S+1}{\sqrt{\mathrm{Var}(S)}}, & \text{when } S < 0. \end{cases} \tag{3}$$

Then standardized test statistic (Z) is used to assess the significance of the trend at 99% and 95% confidence levels. Additionally, the Sen's slope estimator is applied to quantify the magnitude of the identified trends. In this study, trend analysis was performed for seasonal and inter-annual ET time series data obtained from MODIS satellite for each state.

4 Results and Discussion

The interannual variation of ET with values fluctuating approximately 850-1000 mm during 2000-2021 (Fig. 2b and a consistent positive trend at a rate of 3.28 mm/year was observed, indicating a gradual rise in ET over the past two decades. This increasing trend likely reflects the combined influence of rising temperatures, enhanced atmospheric water demand, and potential changes in vegetation productivity in response to a warming climate.

Fig. 2a reveals pronounced spatial heterogeneity of ET value over the region. High ET values >1000 mm/year are observed in Mizoram, lower plains of Assam, Manipur, Nagaland and Tripura. In contrast, Arunachal Pradesh exhibited the lowest ET despite having dense forest cover, which is attributed to its higher latitudinal position. Higher latitude places receive less solar radiation. Because latitude controls angle and duration of solar radiation over a region.

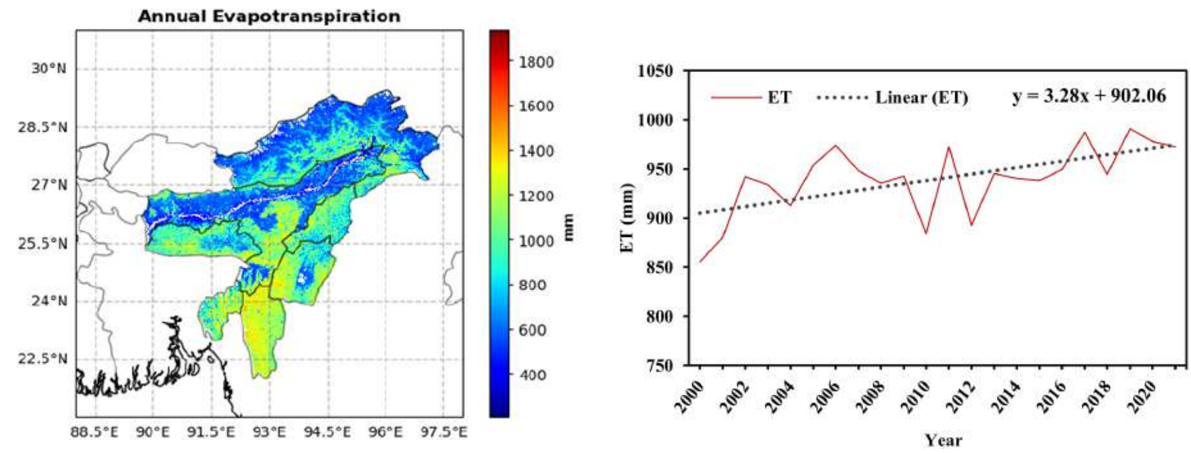

(a) (b)

Figure 2: Spatial and temporal distribution of evapotranspiration over NEI during 2000-2021 using MODIS data.

The seasonal analysis of ET over different states of NEI exhibit distinct seasonal pattern. In Arunachal Pradesh, ET values generally ranged between 180-230 mm and showed a slight increasing tendency at a rate of 0.211 mm/year during the pre-monsoon season (Fig. 3a). In contrast, monsoon season exhibited the highest seasonal ET magnitudes ($\sim$300-400 mm), reflecting the strong influence of peak rainfall and vegetation activity with a decreasing trend at a rate of -0.268 mm/year. This could be associated with cloud induced reduction in net solar radiation or changes in vegetation dynamics during peak monsoon months. The post-monsoon season displayed a weak but positive trend (0.327 mm/year). Similarly, the winter season showed the lowest ET values ($\sim$100-130 mm) but exhibited the strongest increasing trend (0.90 mm/year).

A consistent increase in ET across all seasons in Assam with rates of 0.573 mm/year in pre-monsoon, 1.565 mm/year in monsoon, 0.901 mm/year in post-monsoon and 0.913 mm/year in winter (Fig. 3b). The most pronounced changes during the monsoon, likely driven by increasing temperature, enhanced radiation and vegetation dynamics in response to changing climate conditions. Similarly, Tripura also showing increasing trend for all the seasons (Fig. 3c).

In Manipur, ET ranged between 200-400 mm and showed a notable increasing trend (1.304 mm/year), indicating enhanced land surface heating and vegetation activity before the onset of monsoon rains. The monsoon season exhibited the highest ET positive trend (0.802 mm/year). The winter season recorded comparatively lower ET ($\sim$200-250 mm) but showed a clear increasing trend (0.911 mm/year) (Fig. 3d).

In Nagaland, although monsoon contributes most to the total ET, its trend is slightly declining which is similar to Arunachal Pradesh, while non-monsoon seasons show increasing ET, especially winter and pre-monsoon, suggesting seasonal shifts and intensification of ET (Fig. 3e). In Mizoram, the highest annual increment of ET was noticed (2.69 mm/year) during pre-monsoon followed by monsoon (2.06 mm/year) (Fig. 3f). In Meghalaya, ET is highest during the monsoon season (400-550 mm), followed by the pre-monsoon ($\sim$200-300 mm), post-monsoon ($\sim$200-250 mm) and winter ($\sim$150-200 mm) seasons and all four seasons show positive trends (Fig. 3g).

A comparative analysis of NEI states reveals that Tripura exhibits the highest increasing trend in monsoon ET (2.228 mm/year) followed by Mizoram (2.06 mm/year) and Assam (1.565 mm/year), while Arunachal Pradesh and Nagaland exhibit declining trends of -0.268 mm/year and -0.005 mm/year respectively.

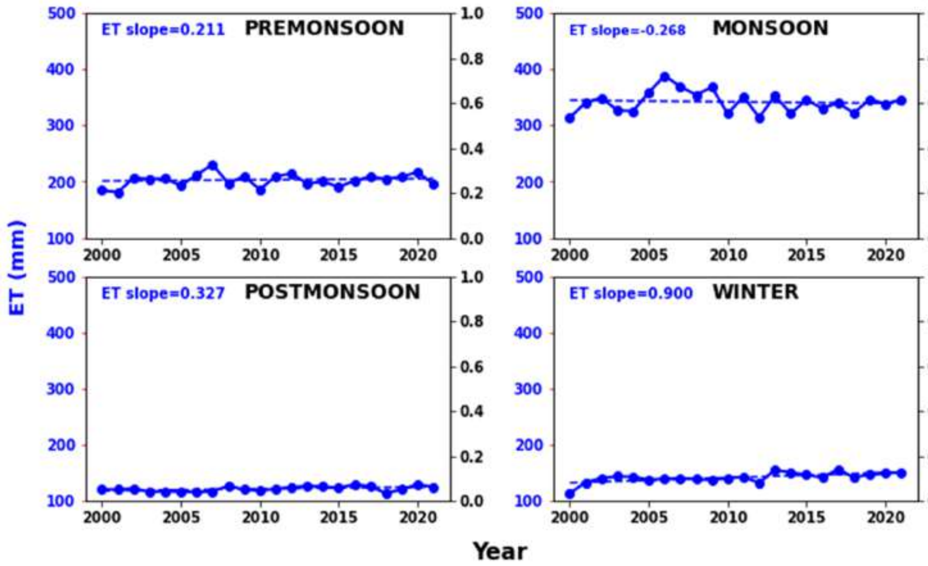

(a) Arunachal Pradesh

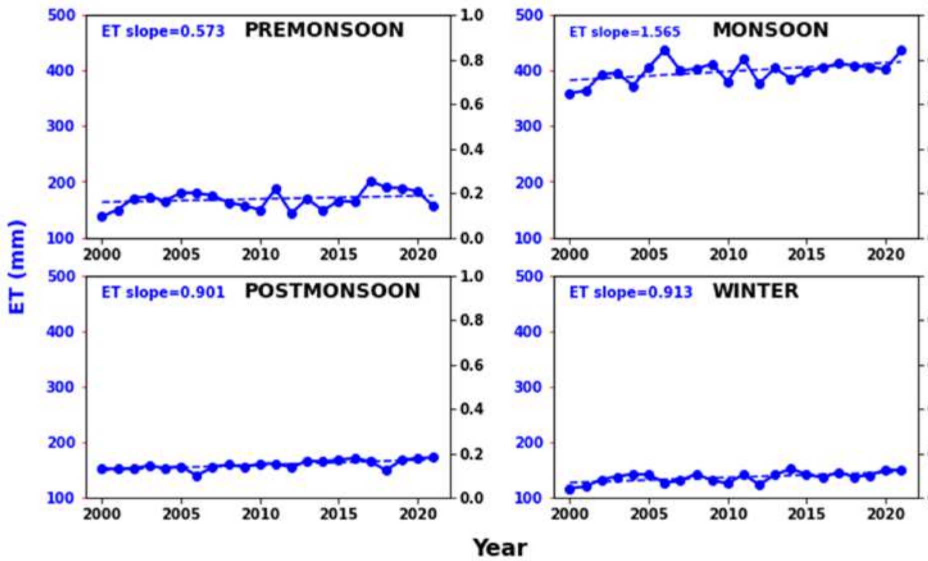

(b) Assam

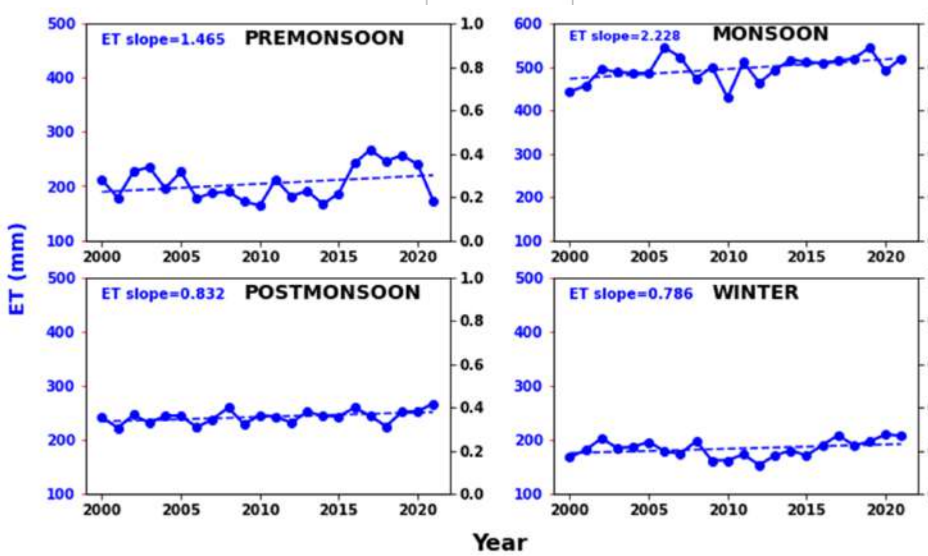

(c) Tripura

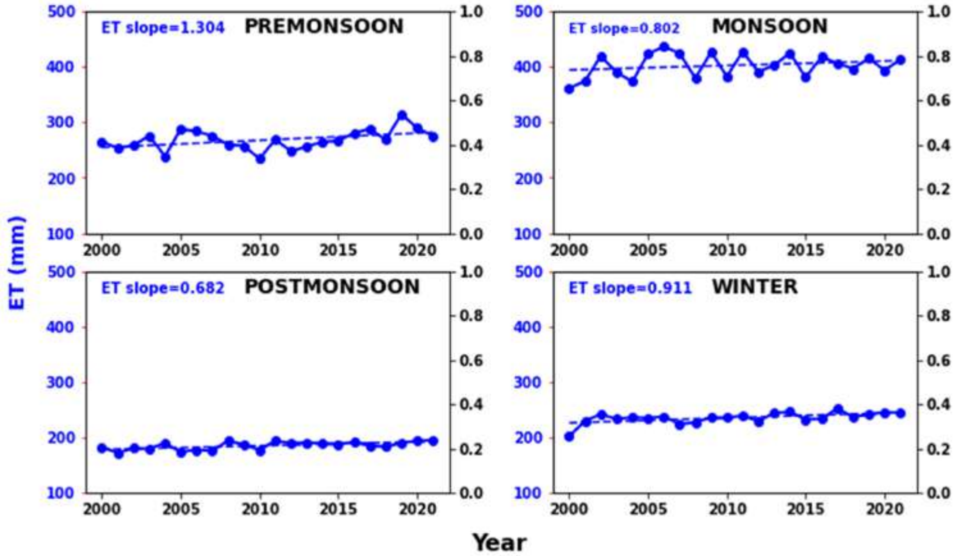

(d) Manipur

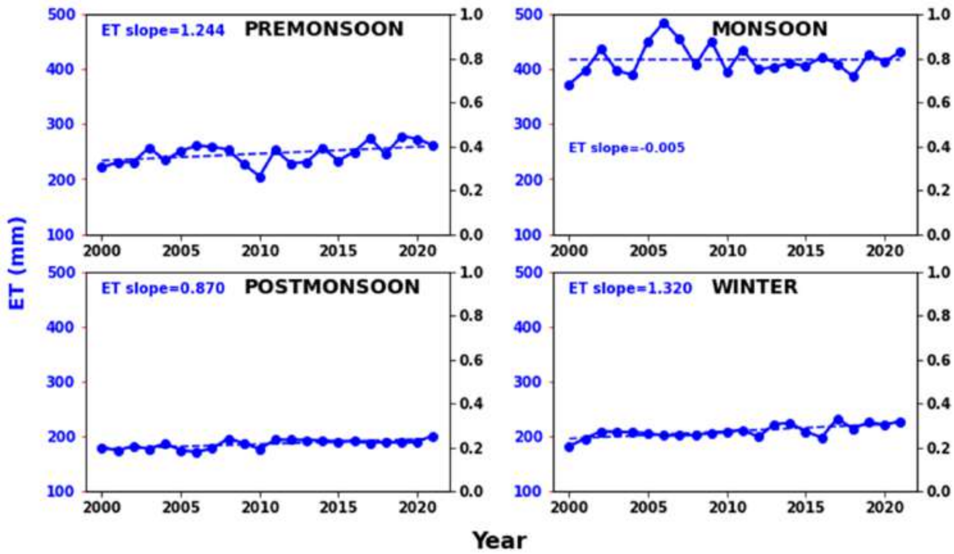

(e) Nagaland

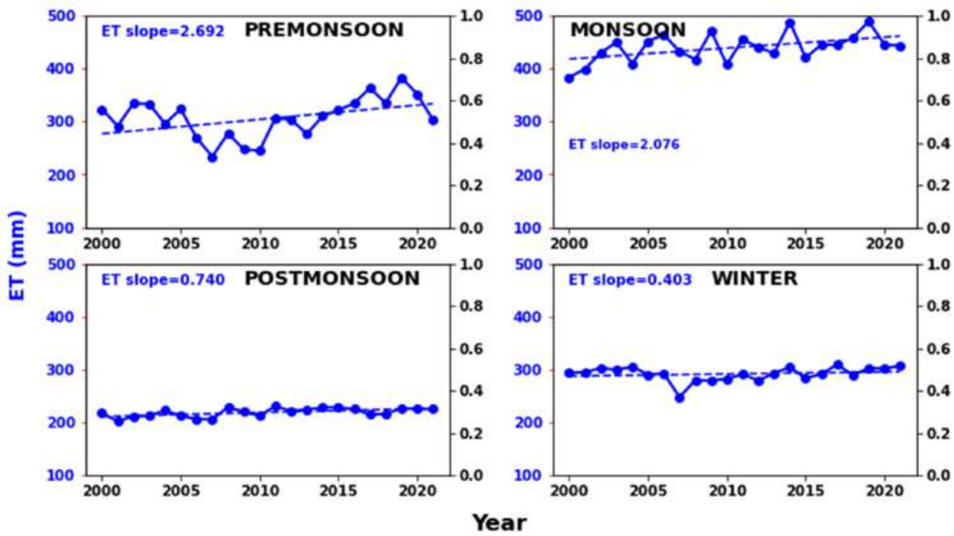

(f) Mizoram

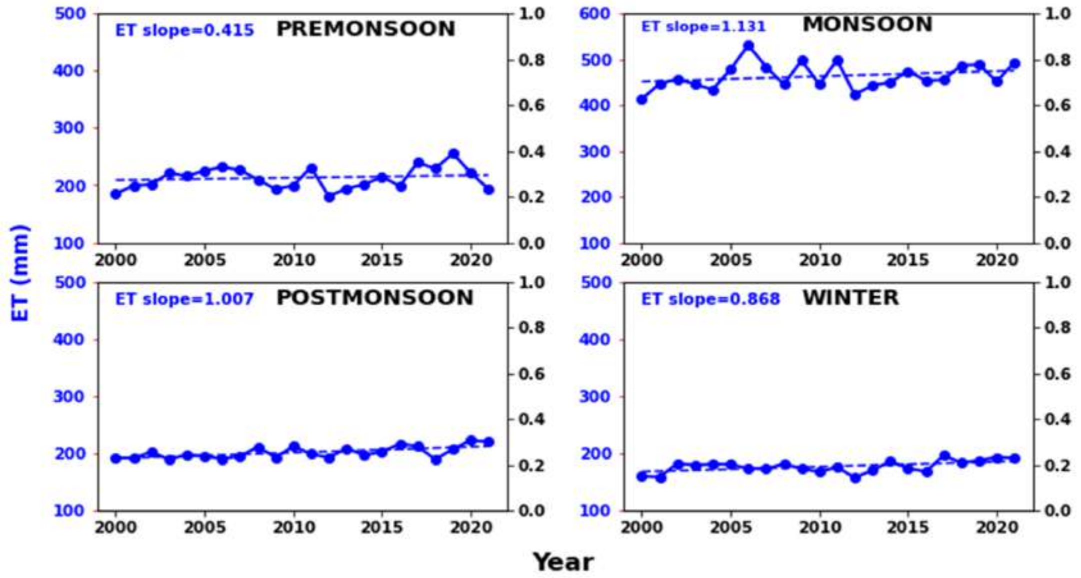

(g) Meghalaya

Figure 3: Temporal changes of ET during 2000-2021 over different states of NEI (a) Arunachal Pradesh (b) Assam (c) Tripura (d) Manipur (e) Nagaland (f) Mizoram (g) Meghalaya.

5 Conclusion

The present study indicates a significant increasing trend in ET across NEI during 2000-2021, highlighting its important role in the regional hydrological cycle in a changing climatic condition. The scarcity of reliable ground-based ET measurements in NEI, the present study provides an overview of ET behavior using the best-available satellite-derived products. The spatial pattern of ET is influenced by differences in land cover types, with the highest ET values observed over vegetation dominated states such as Mizoram, Manipur, Tripura and Nagaland, and the lowest over Arunachal Pradesh due to its higher latitudinal position. Seasonally, ET shows the highest value during monsoon in association with maximum rainfall and vegetation growth, and the minimum value in winter due to dry conditions, leaf fall and limited crop growth. Most of the states exhibit increasing ET trends, while negative trends in the monsoon season over Arunachal Pradesh and Nagaland indicate the influence of altered rainfall patterns on vegetation water use. These findings emphasize that ET is undergoing gradual intensification and seasonal redistribution of ET, impacting water availability, ecosystem productivity, and climate resilience planning in the region. The analysis establishes a much-needed baseline of spatial and temporal ET variability over this complex and data-limited region. This baseline assessment can guide future efforts incorporating high-resolution reanalysis datasets, improved downscaling techniques and dedicated field observations to better quantify and validate ET processes in NEI.

Data availability:

MODIS data can be accessed through (`https://modis.gsfc.nasa.gov/data/`) website.

References

[1] R. G. Allen, L. S. Pereira, D. Raes, and M. Smith, *Crop Evapotranspiration: Guidelines for Computing Crop Water Requirements*, FAO Irrigation and Drainage Paper 56 (Food and Agriculture Organization of the United Nations, Rome, Italy, 1998).

[2] M. F. McCabe, D. G. Miralles, T. R. H. Holmes, and J. B. Fisher, Remote Sens. **11**, 1138 (2019).

[3] L. Gong, C.-Y. Xu, D. Chen, S. Halldin, and Y. D. Chen, J. Hydrol. **329**, 620 (2006).

[4] H. Tabari and P. H. Talaee, Glob. Planet. Chang. **115**, 16 (2014).

[5] J. Gao, M. Qiao, X. Qiu, *et al.*, Adv. Meteorol. **2018**, 2158168 (2018).

[6] L. Yang, J. Li, Z. Sun, *et al.*, PLoS ONE **17**, e0265138 (2022).

[7] J. D. Valiantzas, J. Hydrol. **331**, 690 (2006).

[8] K. Wang and R. E. Dickinson, Rev. Geophys. **50**, RG2005 (2012).

[9] P. K. Raghavendra, K. R. Bhimala, G. K. Patra, and S. Goroshi, Theor. Appl. Climatol. **152**, 999 (2023).

[10] H. Liu, D. Song, J. Kong, Z. Mu, Q. Zhang, and X. Wang, Int. J. Environ. Res. Public Health **19**, 12693 (2022).

[11] A. Mokhtar, H. He, K. Alsafadi, Y. Li, H. Zhao, S. Keo, *et al.*, Environ. Earth Sci. **79**, 312 (2020).

[12] S. Goroshi, R. Pradhan, R. P. Singh, K. K. Singh, and J. S. Parihar, J. Earth Syst. Sci. **126**, 113 (2017).

[13] A. Borah, B. Pathak, A. Medhi, R. Gautam, N. Gogoi, K. J. Baishya, and P. K. Bhuyan, Theor. Appl. Climatol. **156**, 404 (2025).

[14] D. Jhajharia, Y. Dinpashoh, E. Kahya, V. P. Singh, and A. Fakheri-Fard, Hydrol. Process. **26**, 421 (2012).

[15] S. Nandy, K. K. Das, D. Bhavsar, S. Ghosh, S. Badiger, and S. P. S. Kushwaha, Remote Sens. **13**, 1066 (2021).

[16] F. Murata, T. Hayashi, J. Matsumoto, and H. Asada, Nat. Hazards **42**, 391 (2007).

[17] M. A. Friedl, D. Sulla-Menashe, B. Tan, A. Schneider, N. Ramankutty, A. Sibley, and X. Huang, Remote Sens. Environ. **114**, 168 (2010).

[18] Q. Mu, M. Zhao, and S. W. Running, Remote Sens. Environ. **115**, 1781 (2011).

[19] H. A. Cleugh, R. Leuning, Q. Mu, and S. W. Running, Remote Sens. Environ. **106**, 285 (2007).

PROTON ACCELERATION FROM SPHERICAL TARGETS USING HIGH INTENSITY LASER

Jubaraj Choudhury*[1], Sagar Samir Kalita[1], and Nilakshi Das[1]

[1]*Department of Physics, Tezpur University, Tezpur- 784028, Assam, India*

*Corresponding Author: jubarajchoudhury@gmail.com

(Received 25 September 2025; revised 15 December 2025; accepted 4 January 2026; published 1 August 2026)

Abstract: Laser-driven proton acceleration has emerged as an important research area, driven by its applications in medical therapy, nuclear fusion, materials science, and radiography. In this study, we explore spherical targets as proton sources, providing an alternative to conventional flat foil targets. Using a high-intensity laser pulse of $6 \times 10^{20}\ \mathrm{W/cm^2}$, we demonstrate proton energies exceeding 90 MeV, which is notably higher than the energies obtained from rectangular foils of the same thickness. Achieving such energy levels is crucial for advancing practical applications. Furthermore, our results demonstrate that the target diameter plays a decisive role in influencing the acceleration process. The underlying physical mechanisms responsible for these observations are also analyzed and discussed in detail.

Keywords: Laser-plasma interaction, TNSA, PIC simulation.

PACS: 52.38.Kd, 52.38.-r, 41.75.Jv

1 Introduction

Over the past two decades, continuous advancements in high-power laser facilities have made it possible to explore the interaction of matter with extremely intense laser pulses. These interactions extend well beyond the non-relativistic regime, resulting in the generation of extremely strong electric and magnetic fields[1]. When such super-intense laser pulses strike matter, they cause almost instantaneous ionization, creating plasma. This plasma not only sustains the strong fields but also acts as a medium for producing highly energetic beams of particles[2].

Laser-driven ion sources are particularly attractive because they are compact, cost-efficient, and much easier to handle compared to conventional accelerators. Traditional accelerators achieve accelerating gradients of only a few tens of MV/m, requiring kilometre-long beamlines to reach multi-GeV ion energies. In contrast, laser–plasma accelerators can maintain accelerating gradients approaching TV/m, enabling tabletop-sized setups with tremendous potential for applications[3, 4]. At present, significant research efforts are devoted to accelerating protons and heavier ions from solid targets such as metals and plastics using intense laser pulses.

The classification of plasma is based on the electron density in relation to the critical density(n_c) as underdense ($n_e < n_c$) or overdense ($n_e > n_c$). In underdense plasmas, the refractive index remains real, allowing electromagnetic waves to propagate. In overdense plasmas, the refractive index becomes imaginary, preventing wave propagation. Thus, the choice of target and its density relative to n_c critically affects energy absorption and wave propagation.

Since the 1970s, laser–matter interaction studies have revealed efficient electron acceleration. Early experiments focused on pushing electrons to relativistic energies, while subsequent work examined how these energetic electrons could transfer energy to ions, especially protons. The first clear evidence of MeV-scale protons from laser–solid interactions came in the 1990s, with energies steadily increasing through subsequent experiments. A major breakthrough occurred in 2000 when Snavely et al. demonstrated proton beams with maximum energies of 55 MeV, sparking strong interest in the field[5].

Different mechanisms have been proposed to explain ion acceleration. Front-surface acceleration, governed by the laser's radiation pressure, can occur through hole-boring or light-sail mechanisms depending on the thickness of the target. In contrast, most experimental results can be understood using the Target Normal Sheath Acceleration(TNSA) mechanism, which is a model for rear-surface acceleration[2]. Here, hot electrons generated at the laser-irradiated surface migrate to the rear side, where the sheath field generated by the charge separation is sufficiently strong to accelerate ions to high energies. Proton beams from TNSA are typically laminar and low in emittance, though they suffer from broad energy spectra, which limits certain applications[6][7].

To maximize absorption, plasmas having electron density close to the critical density (n_c) are especially important. However, producing such near-critical plasmas is challenging. Solid targets are usually much denser than, while gas jets are far less dense. Techniques such as pre-expanding solids with secondary pulses or using cryogenic gas jets can approach near-critical conditions but often lack precise control over density profiles. Structured targets are widely investigated because they enhance laser energy absorption by both electrons and ions[8–17]. Spherical targets having diameter of a few tens of microns are also studied to accelerate ions[18–22].

In this work, we have investigated proton acceleration from a spherical target using a laser of intensity $6 \times 10^{20} W/cm^2$. The dimension of the target is selected to be smaller than the laser spot size, which has not be studied in detail in earlier works[18, 20, 21]. Manufacturing these targets have become a reality with the advancements of technology. Over the years, spherical targets have been extensively utilized in laser–matter interaction research. Spherical water droplets with micrometer-scale radii , [23, 24], gas-cluster targets having sub-micron dimensions [25, 26], and small objects supported by structures with sizes from a few hundred nanometers to several microns [19, 27] are commonly used examples of mass-limited targets. A major advancement was made by Ostermayr et al., who, for the first time, employed well-defined and truly isolated charged polystyrene (C_8H_8) spheres as targets, by levitating it using a Paul trap[28]. The composition as well as the dimension of the target used in our work are well within the range which has been tested in earlier experiments of laser matter interaction, however the study of ion acceleration using laser of intensity (I_0) in $10^{20} - 10^{21}$ W/cm^2 range is novel. The introduction is followed by simulation parameters in section 2. Section 3 is the results and discussion and the conclusion is discussed at the end in section 4.

2 Simulation Scheme

In this work, two-dimensional particle-in-cell (PIC) simulations were conducted with the fully relativistic PIC code EPOCH[29]. The simulation grid was defined with a spatial resolution of $\Delta x = 8.5\ nm$ and $\Delta y = 13.33\ nm$. Open boundary conditions were applied to fields and particles across all boundaries of the simulation box.

The laser pulse considered in our work has central wavelength of $\lambda = 1\mu m$ with a gaussian profile. The transverse size (FWHM) of the pulse is $4.24\mu m$, while the pulse duration,τ_L is 56.5 femtoseconds (fs). The maximum intensity(I_0) of the laser is $6 \times 10^{20} W/cm^2$ corresponding to normalised amplitude $a_0 = \frac{eE}{m_e \omega c}$ = 20.8. The laser enters the simulation box from the left boundary and propagates along x-direction.

For the study, both spherical target and flat foils are considered. In case of the spherical target, the center is positioned at $x = 0$ with diameter same as the thickness of the foil. The front surface of the flat foil is positioned at $x = 0$. The transverse length along the y-direction is 8 micron. The electron density taken is $n_e = 270 n_c$, where $n_c = 1.11 \times 10^{21}/cm^3$ denotes the critical density for the laser wavelength $\lambda = 1\mu m$. The target taken in our study is composed of plastic (CH). In the simulations, 150 macroparticles per cell are employed for electrons and protons.

3 Results and discussion

As the laser is irradiated on the target surface, electrons respond first and gain momentum. The laser pulse reaches its peak at the target at approximately 80 fs of simulation time. The electron density plot at this time shows the electrons escaping into the vacuum. These electrons are accelerated due to ponderomotive force of the pulsed laser. The electrons are driven outward, away from the center of the pulse, primarily due to the strong spatial gradients in the laser electric field. Due to a linearly polarised laser, the ponderomotive force is given by the following expression:

$$\mathbf{f}_p = -\frac{e^2}{8 m_e \omega^2} \nabla \left[E_s^2(\mathbf{r})(1 + \cos 2\omega t) \right]$$

Here, e, m_e are the charge and mass of the electrons. E_s is the laser electric field and ω is the incident laser frequency. The expression also contains an oscillatory term, which generates two bunches of electrons during each laser cycle. This term originates from the magnetic component of the Lorentz force. When the laser intensity

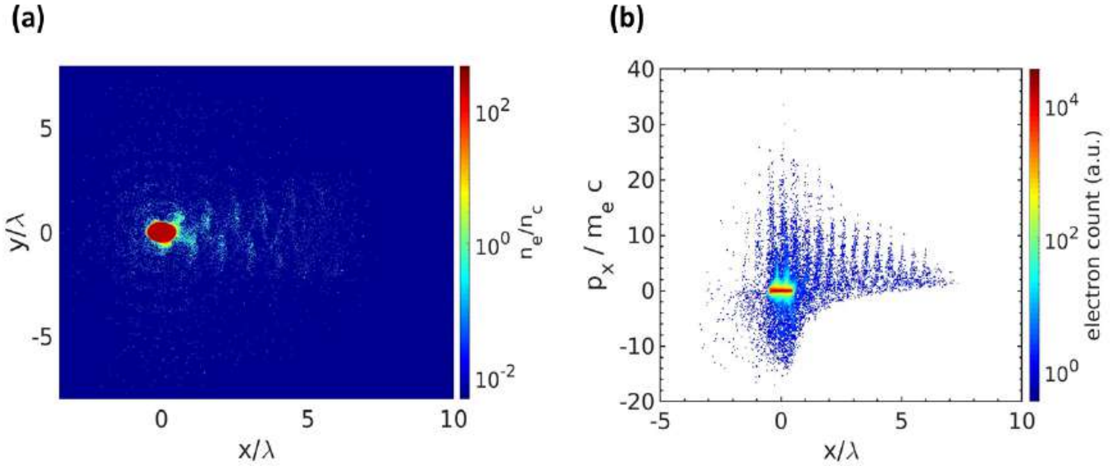

Figure 1: (a) Electron density plot at 80fs, showing electron bunches with $\lambda/2$ periodicity. (b) Corresponding electron momentum(p_x) shows the positions of bunches.

is very high ($\geq 10^{18} W/cm^2$), the effect of magnetic field part of the lorentz force generates bunches of electrons via the '$J \times B$' heating method. These bunches are spatially separated by a distance of $\lambda/2$. From the Fig. 1(a), electron bunches having spatial periodicity $\lambda/2$ are observed, which indicates the role of $J \times B$ heating in accelerating the electrons. The phase plot (Fig. 1(b)) also shows the bunches with periodicity $\lambda/2$. These highly energetic electrons or 'hot electrons' travel through the target and are trapped as they reach the rear surface. The accumulation of hot electrons at the rear surface produces a quasi-static electric field, which is strong enough to ionize and accelerate atoms from the target's rear side. This method, through which the rear ions gain momentum and accelerate is termed as Target Normal Sheath Acceleration (TNSA).

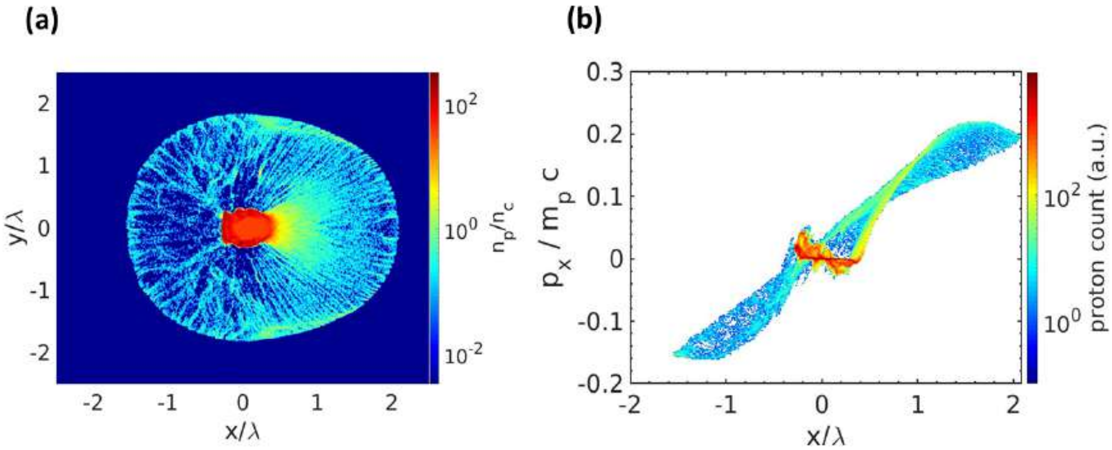

Figure 2: (a) Proton density profile at 120 fs, showing the emission of majority protons from rear surface.(b)corresponding longitudinal proton momentum profile,shows accelerated protons from both front and rear surface

The Radiation Pressure Acceleration (RPA) method is another acceleration method through the front protons gain momentum and accelerate[30]. Fig. 2(a) shows the proton density plot at around 120 fs simulation time. The protons can be seen to be accelerated from all sides of the target, however the rear protons are found to have the highest momentum(Fig. 2(b)). These protons are accelerated by TNSA mechanism. The RPA mechanism is also observed to accelerate the front protons but the momentum is much less than the TNSA accelerated rear protons. For RPA to be dominant, the intensity of the laser needs to be $\gtrsim 10^{22}\ W/cm^2$.

The simulation is performed up to a time till the energy of the protons saturate. Fig. 3(a) shows the proton density at 500 fs simulation time, which is the end of the simulation. The Fig. 3(b) presents the energy spectrum

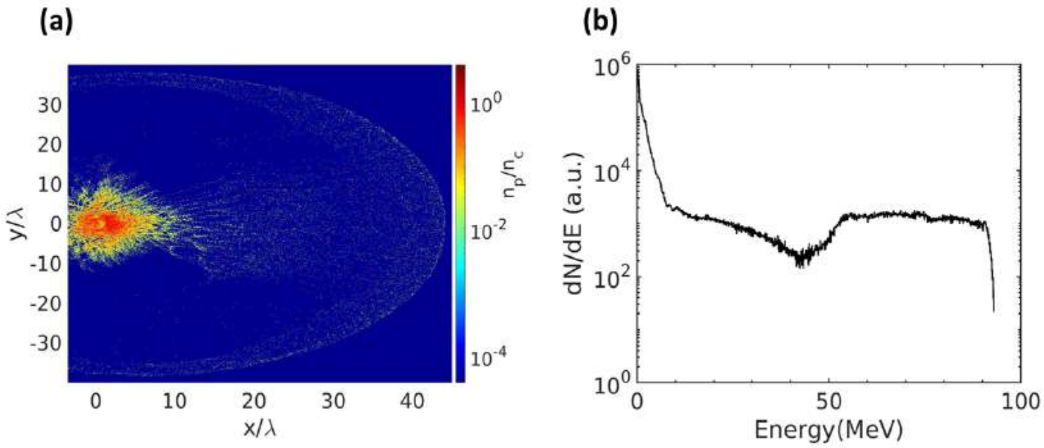

Figure 3: (a) Density plot showing accelerated protons. (b) Proton energy spectra at 500 fs. The maximum proton energy is $\sim$ 93 MeV.

of the accelerated protons measured at this time. The maximum energy of the protons is found to be around 90 MeV. This energy is significantly higher than the energy obtained from conventional flat foils of similar thickness. Protons with energy around 90 MeVs are desired for numerous practical applications. Using a flat foil with the same thickness as the spherical target's diameter results in proton energies of approximately 50 MeV. The proton energy spectra for the spherical target as well as the flat foil are shown in Fig. 4(a).

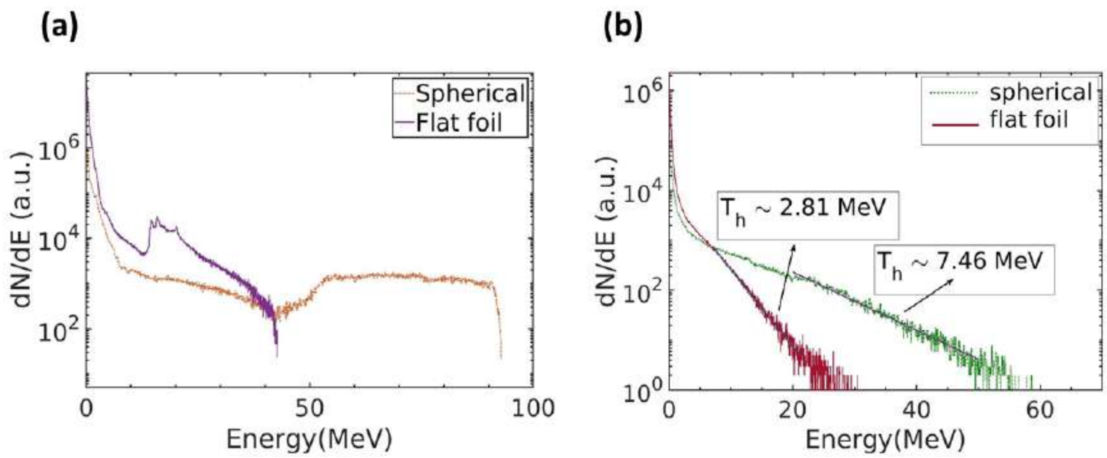

Figure 4: (a) Proton energy spectra for the foil (purple solid line) and spherical target(orange dotted line) showing spherical target has boarder and high-energetic distribution compared to flat foil at 500 fs. (b) Electron energy spectra for the foil (red solid line) and spherical target(green dotted line) showing the hot electron temperature(T_h) when electron energy is maximum. The hot electron temperature increase significantly in spherical target. Here the thickness of the foil and the sphere are same and equal to 1 micron.

With an objective of understanding the reason behind the observed higher energy in the spherical target, we have obtained the electron energy spectra and the hot-electron temperature for the two cases. The temperature of the hot electrons serves as an important indicator of how much energy the electrons have absorbed from the laser. A higher electron temperature generally means that the electrons have gained more energy, which subsequently leads to the creation of a stronger sheath electric field at the target rear surface. This field is essential for accelerating protons to high energies. From Fig. 4(b), it is evident that energy of the electrons and also the T_h is higher in the spherical target. This ultimately contributes to the higher energy in the protons in the spherical target.

The behaviour of the accelerated protons in our simulations is analyzed using the theoretical model developed by Mora et al., which quantitatively predicts proton energies in the TNSA regime.[31]. The model is a 1D collisionless plasma expansion model where electrons are treated as Boltzmanian and Ions are treated as cold and initially at rest. Electron density profile follows the Boltzmann's equation and ions are treated through fluid equations. With fluid equations and Poisson's equation, electric field is calculated at the ion front. It predicts the ion energy spectrum and ion cut off energy.

The maximum ion energy due to TNSA can be expressed as [31] [32]:

$$\varepsilon_{\text{max}} = 2Zk_BT_h\left[\ln\left(\tau' + \sqrt{\tau'+1}\right)\right]^2.$$

Here

$$\tau' = \frac{\omega_{pi}t}{\sqrt{2e_N}}, \qquad \omega_{pi} = \sqrt{\frac{e^2 n_{e0}}{\epsilon_0 m_i}},$$

is the ion plasma frequency with ion mass m_i, t the acceleration time, $e_N = 2.718...$, Z is charge state of the ion species, n_{e0} denotes ion density at initial time, k_B and ϵ_0 are the Boltzman constant and the dielctric constant in vacuum.

For sufficiently long acceleration times ($\omega_{pi}t \gg 1$), the cutoff energy can be approximated as

$$\varepsilon_{\text{max}} \approx 2Zk_BT_h\left[\ln(2\tau')\right]^2.$$

An acceleration time of $t \sim 1.3\,\tau_L$ has been found to provide a good prediction of the proton energy scaling.

From the above expressions and using the hot electron temperature obtained in our simulations, the expected maximum proton energy for a flat foil target is found to be about $\sim$ 45 MeV. This value agrees well with the energies obtained in our simulations, demonstrating the consistency of the model in this case. On the other hand, the same model predicts a proton energy of approximately 121 MeV for the spherical target. However, this value is noticeably higher than what we actually obtained from our simulation results.

The difference arises because the theoretical model used here is essentially one-dimensional (1D). While such a model is quite suitable for describing the simpler case of a flat foil target, it may not fully capture the more complex effects introduced by curved or spherical geometries. In the case of spherical targets, the geometry strongly impacts the dynamics of the interaction and, in turn, the final energies. In particular, the hot electrons, which generate the sheath field and drive ion acceleration, behave differently in spherical geometry. Although they initially contribute to a strong accelerating field, the electrons may naturally diverge as they move away from the curved surface. This divergence weakens the sheath field over time, leading to a reduction in the strength of ion acceleration and consequently a lower maximum proton energy than predicted by the simple theory.

From the Fig. 2(b), the protons having maximum energy can be observed to be accelerated from the rear surface. The hot electron cloud at the rear surface creates a sheath electric field at the rear surface and this longitudinal field accelerates the protons from the rear surface of the target, via the TNSA mechanism. The longitudinal electric field plot is obtained for both the flat & the spherical target, as seen in Fig. 5. It can be seen that the strength of the electric field created on the rear surface of the spherical target is much stronger than the field generated in the flat foil case. The combined effect of multiple physical phenomena contribute to the enhanced strength of the electric field generated by the hot electrons. The smaller transverse size of the spherical target results in the laser energy being distributed among fewer electrons compared to an extended flat foil target. This leads to enhanced energy of the electrons. Another important reason behind the enhanced T_h is due to the fact that due to the size of the target, the diffracted part of the laser from the edges of the target creates a current of electrons across the surface, leading to an elevated count of electrons at the rear surface. This leads to the enhanced longitudinal electric field in the spherical target case. This consequently results in higher energy in the accelerated protons, which is driven by this sheath field.

In the next part of our study, we examined how the dimension of the target, when compared to that if the laser spot, influences both laser energy absorption and the subsequent acceleration of protons. Since the majority of the laser energy is concentrated in the central part of the laser, the relative dimension of the target becomes an important factor in determining how effectively the energy is absorbed and transferred to the particles. The spot size of the laser used in our study is 4.24 micron.

Simulation are performed by varying the target diameter systematically from 0.8 microns to 3 microns. The proton cutoff energy is obtained from the spectra for different diameters and is shown in Fig. 6(a). The findings indicate that larger target diameters correspond to lower maximum proton energies. This behaviour highlights the strong influence of target size on the efficiency of proton acceleration. The dependence of proton cutoff energy on

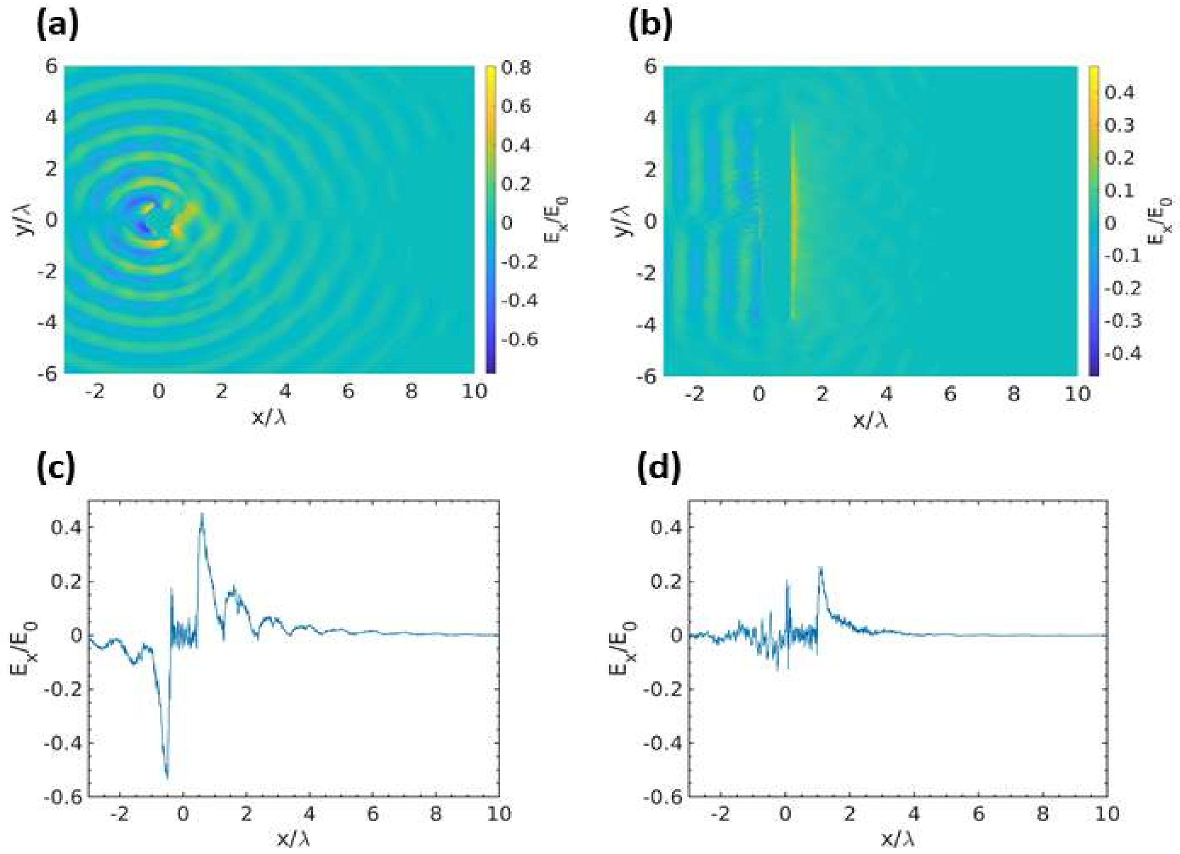

Figure 5: (a) Longitudinal electric field (E_x/E_0) profile in the spherical target. (b) E_x/E_0 plot in the x-y plane in the flat foil.(c) E_x/E_0 plot close to the central axis (y=0) for the flat foil.(d) Electric field plot close to the center of the target (y=0) for the flat foil. The plots shown are from 100 fs of simulation time, when the laser interaction with the target has occurred and the rear sheath field is fully formed. All these plots shows the sheath field formed in the spherical target is much stronger than the field in the flat foil target case.

the diameter of the sphere is shown in Fig. 6a. For a 3 micron diameter target, the energy of accelerated proton reaches ~ 50 MeV. It increases to ~ 93 MeV for a 1 Micron diameter target and no significant change is observed on further decreasing the diameter to 0.8 micron. The diameter has not been decreases further below 0.8 micron.

In order to understand the reason behind the observed variation, the laser energy absorption percentage and hot-electron temperatures are obtained using the electron energy plot. The hot-electrons contribute to the formation of strong sheath electric field which drives ion acceleration from the rear surface of the target. Fig. 6(b) shows the variation of T_h with varying target diameters. The electrons temperatures are found to show a trend similar to the one observed in proton energy. The temperatures decrease with increase in diameter. The maximum T_h of $\sim$7.5 MeV is obtained for the 1 micron diameter sphere. A small decrease in the temperature is observed in the 0.8 micron case.

The hot-electron temperature variation and the variation in the laser energy absorption by the electrons can help us understand the observed variation in the proton energy. When the target diameter becomes much smaller than the size of the laser spot, a portion of the laser beam passes around the target edges without interacting with it, leading to a loss of laser energy. This effect explains the relatively higher energy absorption observed for the 3-micron diameter case and the subsequent reduction in absorption as the target diameter decreases further. However, to understand the reason behind hot electron temperature increase with decreasing target diameter up to 0.8 micron requires a detailed analysis.

Most of the energy of the laser is concentrated in the central part of the pulse. With reduction in size of the target, this concentrated energy is distributed among a smaller number of particles within the interaction region. Consequently, each particle receives a larger share of the absorbed energy, which results in an overall enhancement

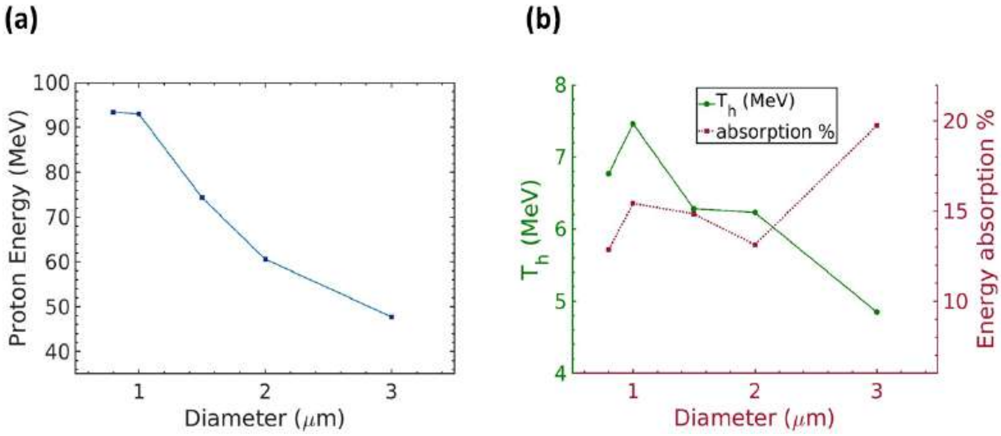

Figure 6: (a)The plot shows variation of proton cutoff energy with target diameter. Proton energy decreases as the target diameter increases. (b) This plot shows variation of hot electron temperature (T_h) and laser energy absorption on target diameter. The hot electron temperature decreases with increasing diameter while the energy absorption exhibits an increasing trend.

in the energy of the hot electrons. Elevated hot electron temperatures enhance the rear-surface sheath field strength, consequently improving the efficiency of proton acceleration.

4 Conclusion

This work explores the acceleration of protons from spherical targets, with particular emphasis on the underlying mechanisms driving ion generation and energy gain. While flat foils have been the standard choice for many years, our results show that spherical targets provide advantages that can significantly improve ion acceleration. Most of the previous studies were limited to studying electron and ion acceleration from targets with diameter greater than the laser spot size and with low intensity lasers, our investigation focuses on targets with diameter less than the laser spot size[18–21]. Isolated spherical targets can now be manufactured for various studied[20]. In our study, a spherical target of diameter 1 μm is found to provide proton cutoff energy of 93 MeV, whereas the flat foil of equal thickness produces 45 MeV. This demonstrates a substantial enhancement in energy when using a curved geometry. Similarly, the T_h in the spherical target is found to be 7.46 MeV, notably higher than the 2.81 MeV obtained for the flat foil. These results confirm that spherical targets are more effective in confining electrons and generating stronger accelerating fields. We have also studied the effect of varying the diameter of spherical targets. The results show a decreasing trend in both maximum proton energy and hot electron temperature with increasing diameter. These ions are found to be accelerated using the TNSA mechanism. The generation of hot electrons at the front surface leads to the formation of a sheath field, enabling ion acceleration from the rear surface. It is important to note that 3D simulations generally provide more accurate predictions of experimental outcomes than 2D simulations, although they require significantly greater computational resources. In order to qualitatively comprehend the physical process and mechanism involved during laser-plasma interaction, 2D simulations are found to be reliable. In the context of TNSA process, although the 2D simulation usually overestimates the strength of the fields generated and the energy of the accelerated protons, the difference in the energy of protons from 2D and 3D simulations are very small[7, 33, 34]. 3D simulations are necessary to get a good idea of the expected energy in an experiment. In summary, we have shown that spherical targets provide a clear geometric advantage in laser-driven ion acceleration, offering higher particle energies and stronger electron heating. This makes them a promising candidate for applications requiring compact, high-quality proton beams.

Acknowledgement

Author Jubaraj Choudhury acknowledges financial support from the DST-INSPIRE Fellowship (No. IF190925). Support from the Core Research Grant (SERB-DST), Government of India, is also gratefully acknowledged.

References

[1] H. Daido, M. Nishiuchi, and A. S. Pirozhkov, Rep. Prog. Phys. **75**, 056401 (2012).

[2] A. Macchi, M. Borghesi, and M. Passoni, Rev. Mod. Phys. **85**, 751 (2013).

[3] V. Malka, S. Fritzler, E. Lefebvre, M.-M. Aleonard, F. Burgy, J.-P. Chambaret, J.-F. Chemin, K. Krushelnick, G. Malka, S. Mangles, *et al.*, Science **298**, 1596 (2002).

[4] E. Esarey, P. Sprangle, J. Krall, and A. Ting, IEEE Trans. Plasma Sci. **24**, 252 (1996).

[5] R. Snavely, M. Key, S. Hatchett, T. Cowan, M. Roth, T. Phillips, M. Stoyer, E. Henry, T. Sangster, M. Singh, *et al.*, Phys. Rev. Lett. **85**, 2945 (2000).

[6] S. Wilks, A. Langdon, T. Cowan, M. Roth, M. Singh, S. Hatchett, M. Key, D. Pennington, A. MacKinnon, and R. Snavely, Phys. Plasmas **8**, 542 (2001).

[7] H. Ruhl, S. Bulanov, T. Cowan, T. Lisekina, P. Nickles, F. Pegoraro, M. Roth, and W. Sandner, Plasma Phys. Rep. **27**, 363 (2001).

[8] M. Bailly-Grandvaux, D. Kawahito, C. Mcguffey, J. Strehlow, B. Edghill, M. Wei, N. Alexander, A. Haid, C. Brabetz, V. Bagnoud, *et al.*, Phys. Rev. E **102**, 021201 (2020).

[9] H. Deng, R. Sha, L. Hu, X. Jiang, N. Zhao, D. Zou, T. Yu, and F. Shao, Plasma Phys. Control. Fusion **64**, 085004 (2022).

[10] B. Feng, L. Ji, B. Shen, X. Geng, Z. Guo, Q. Yu, T. Xu, and L. Zhang, Phys. Plasmas **25**, 103109 (2018).

[11] C. Qin, H. Zhang, S. Li, N. Wang, A. Li, L. Fan, X. Lu, J. Li, R. Xu, C. Wang, *et al.*, Commun. Phys. **5**, 124 (2022).

[12] S. Chen, T. Iwawaki, K. Morita, P. Antici, S. Baton, F. Filippi, H. Habara, M. Nakatsutsumi, P. Nicolaï, W. Nazarov, *et al.*, Sci. Rep. **6**, 1 (2016).

[13] A. Sgattoni, P. Londrillo, A. Macchi, and M. Passoni, Phys. Rev. E **85**, 036405 (2012).

[14] M. Dozières, G. Petrov, P. Forestier-Colleoni, P. Campbell, K. Krushelnick, A. Maksimchuk, C. McGuffey, V. Kaymak, A. Pukhov, M. Capeluto, *et al.*, Plasma Phys. Control. Fusion **61**, 065016 (2019).

[15] G. Gadea, A. Morata, J. Santos, D. Dávila, C. Calaza, M. Salleras, L. Fonseca, and A. Tarancón, Nanotechnology **26**, 195302 (2015).

[16] A. Andreev, K. Platonov, J. Braenzel, A. Lübcke, S. Das, H. Messaoudi, R. Grunwald, C. Gray, E. McGlynn, and M. Schnürer, Plasma Phys. Control. Fusion **58**, 014038 (2015).

[17] O. Klimo, J. Psikal, J. Limpouch, J. Proska, F. Novotny, T. Ceccotti, V. Floquet, and S. Kawata, New J. Phys. **13**, 053028 (2011).

[18] J. Limpouch, J. Psikal, A. Andreev, K. Y. Platonov, and S. Kawata, Laser Part. Beams **26**, 225 (2008).

[19] A. Henig, D. Kiefer, M. Geissler, S. G. Rykovanov, R. Ramis, R. Hörlein, J. Osterhoff, Z. Major, L. Veisz, S. Karsch, *et al.*, Phys. Rev. Lett. **102**, 095002 (2009).

[20] T. Sokollik, T. Paasch-Colberg, K. Gorling, U. Eichmann, M. Schnürer, S. Steinke, P. Nickles, A. Andreev, and W. Sandner, New J. Phys. **12**, 113013 (2010).

[21] A. Kemp and H. Ruhl, Phys. Plasmas **12** (2005).

[22] T. Liseykina, S. Pirner, and D. Bauer, Phys. Rev. Lett. **104**, 095002 (2010).

[23] T. Sokollik, M. Schnürer, S. Steinke, P. Nickles, W. Sandner, M. Amin, T. Toncian, O. Willi, and A. Andreev, Phys. Rev. Lett. **103**, 135003 (2009).

[24] S. Karsch, S. Düsterer, H. Schwoerer, F. Ewald, D. Habs, M. Hegelich, G. Pretzler, A. Pukhov, K. Witte, and R. Sauerbrey, Phys. Rev. Lett. **91**, 015001 (2003).

[25] S. Ter-Avetisyan, B. Ramakrishna, R. Prasad, M. Borghesi, P. Nickles, S. Steinke, M. Schnürer, K. Popov, L. Ramunno, N. Zmitrenko, *et al.*, Phys. Plasmas **19**, 073112 (2012).

[26] Y. Fukuda, A. Y. Faenov, M. Tampo, T. Pikuz, T. Nakamura, M. Kando, Y. Hayashi, A. Yogo, H. Sakaki, T. Kameshima, *et al.*, Phys. Rev. Lett. **103**, 165002 (2009).

[27] K. Zeil, J. Metzkes, T. Kluge, M. Bussmann, T. Cowan, S. Kraft, R. Sauerbrey, B. Schmidt, M. Zier, and U. Schramm, Plasma Phys. Control. Fusion **56**, 084004 (2014).

[28] T. M. Ostermayr, D. Haffa, P. Hilz, V. Pauw, K. Allinger, K.-U. Bamberg, P. Böhl, C. Bömer, P. Bolton, F. Deutschmann, *et al.*, Phys. Rev. E **94**, 033208 (2016).

[29] T. Arber, K. Bennett, C. Brady, A. Lawrence-Douglas, M. Ramsay, N. Sircombe, P. Gillies, R. Evans, H. Schmitz, A. Bell, *et al.*, Plasma Phys.Control. Fusion **57**, 113001 (2015).

[30] E. Clark, K. Krushelnick, J. Davies, M. Zepf, M. Tatarakis, F. Beg, A. Machacek, P. Norreys, M. Santala, I. Watts, *et al.*, Phys. Rev. Lett. **84**, 670 (2000).

[31] P. Mora, Phys. Rev. Lett. **90**, 185002 (2003).

[32] J. Fuchs, P. Antici, E. d'Humières, E. Lefebvre, M. Borghesi, E. Brambrink, C. Cecchetti, M. Kaluza, V. Malka, M. Manclossi, *et al.*, Nature Phys. **2**, 48 (2006).

[33] L. A. Daneshmand, M. Aszalos, S. Feister, and J. R. Smith, Phys. Plasmas **32** (2025).

[34] L. Fedeli, A. Formenti, L. Cialfi, A. Pazzaglia, and M. Passoni, Sci. Rep. **8**, 1 (2018).

COMPACT MIMO ANTENNA WITH ENHANCED ISOLATION FOR WLAN AND C-BAND APPLICATIONS

Trishna Doloi[*1], Gouree Shankar Das[1], Akash Buragohain[1,2], Partha Protim Kalita[1], and Yatish Beria[1]

[1]*Microwave Research Laboratory, Department of Physics, Dibrugarh University, Dibrugarh-786004, Assam, India*
[2]*Department of Physics, Tingkhong College, Dibrugarh-786612, Assam, India*

[*]Corresponding Author: doloitrishna1@gmail.com

(Received 25 September 2025; revised 5 January 2026; accepted 21 January 2026; published 1 August 2026)

Abstract: This article proposes a four-element Multiple Input Multiple Output (MIMO) antenna configuration to operate in the 4 - 8 GHz frequency range for WLAN and C-band applications. The designed structure is realized on a cost-effective, high-loss FR-4 substrate with a compact dimension. The proposed design is suitable to serve in the 5G new radio (NR) n79 (4.4 - 5 GHz), n102 (5.925 - 6.425 GHz), n104 (6.425 - 7.125 GHz) bands, as well as WLAN applications for the frequency ranges of 4.9 GHz, 5 GHz, and 5.9 GHz. The entire footprint of the designed antenna is 46 mm $\times$ 46 mm $\times$ 1.6mm. All four radiating elements are orthogonally placed, and each is coupled to a feedline for better coupling performance. To decrease the inter-element coupling among the radiators, parasitic elements are added between the patch elements. Also, a defective ground structure is used to improve isolation. These also enhance the overall antenna performance, as the result shows improvement in average isolation, total efficiency (>80%), and gain (>5 dB). The antenna design is carried out to meet the requirements of the specified frequency bands, rendering it an effective choice for WLAN, 5G NR (n79, n102, and n104), and C-band applications.

Keywords: MIMO antenna, WLAN, defected ground structure (DGS), isolation enhancement, 5G NR, C-band.

PACS: 84.40.Ba, 88.80.ht, 85.50.-n, 84.40.Dc

1 Introduction

As wireless communication technologies continue to advance, the demand for improved data rates, higher spectral efficiency, and dependable connectivity is steadily increasing. MIMO antenna technology has gained prominence as a notable development in modern communication, as it facilitates high data transfer rates, enhances spectral efficiency, and minimises signal degradation [1]. By incorporating multiple radiating elements, MIMO systems use spatial diversity and multipath propagation, thereby enabling robust performance even in complex wireless environments [2]. This technology contributes significantly in fulfilling the rising need for high-speed, reliable, and energy-efficient communication, particularly in applications such as 4G, 5G, and beyond. Consequently, MIMO has become an indispensable solution for next-generation wireless networks, where efficiency and robust connectivity are of paramount importance.

Compactness is one of the essential design considerations in MIMO antennas, especially for portable and integrated communication devices [3]. However, reducing the physical dimensions of antenna elements often results in increased mutual coupling and reduced isolation, which adversely affect the system performance as a whole. Achieving a balance between miniaturization and sufficient port isolation remains a significant challenge for antenna designers, particularly due to multiple radiating elements [1].

Various isolation enhancement techniques such as defected ground structure (DGS) method [4–6], electromagnetic bandgap (EBG) [7], balanced open slot [8], different radiating modes [9], decoupling circuits [10, 11] neutralization line (NL) [12, 13], etc. have been applied to reduce the interactions and interdependence between the radiating elements with isolation enhancement among them. Among these, DGS has been observed as a highly effective method, as it disrupts the surface current distribution and suppresses coupling paths without significantly increasing antenna size [3]. This makes DGS-based designs attractive for compact, high-performance MIMO systems.

Given these facts, researchers have been trying to develop MIMO antenna systems for different wireless applications. A MIMO antenna containing eight elements for a 5G mobile application is presented in ref. [14]. The high-performance antenna operated over the frequency range from 2.5-3.6 GHz. The antenna provided a channel capacity of 34.25 bps/Hz with 20 dB of SNR in free space, about three times that of 2×2 MIMO operations [14]. A multi-purpose dual MIMO system, comprises two MIMO antenna sets integrated on a single substrate, one 8-element MIMO with a dimension of 150 mm$\times$70 mm working on the 3.4 - 3.6 GHz frequency and one 4-port MIMO working on 5.02 - 6.93 GHz with a dimension of 20mm$\times$7mm, for 5G mobile systems, is presented in [15]. In [16], a chain of defected ground structures is used to design a MIMO antenna with low mutual coupling and minimize cross-polarization. The reported radiation efficiency was 74%, with 2 dBi peak gain. A circularly polarized MIMO antenna with orthogonal modes for the 5G cellular application system operating below 6 GHz is presented, covering the 3.4 - 3.8 GHz band [17]. The antenna design achieved more than 20 dB isolation among the elements. The overall efficiency of the suggested design was above 80%, with more than 4 dBic of CP gain in the operating bandwidth. A novel method for decoupling, by employing multiple radiation modes with varying patterns and polarizations is proposed in ref. [9]. The antenna delivered an isolation of 23 dB between 2.4 GHz and 2.65 GHz with a maximum efficiency of 92% over the operating frequency range. A small-sized dual-element MIMO antenna operating in the sub-6 GHz band for 5G applications is designed by Mathew et al. in [18]. The antenna design was based on slot radiators and used FR4 substrate. The proposed design is optimized by using a defective ground structure to increase the port-isolation. The operational bandwidth of the antenna ranges from 3.1 GHz to 4.2 GHz. In [19], Ding et. al. designed a MIMO antenna using a parabolic reflector along with a parasitic strip. The entire footprint of the compact broadband MIMO antenna element is 36mm$\times$27mm$\times$0.8 mm, printed using expensive Rogers substrate to cover the bandwidth range of 2.32 GHz to 2.95 GHz.

The works documented in the literature have employed various methods to increase isolation between radiating elements. However, the recent literature hardly ever shows low mutual coupling with high gain and overall improved antenna parameters in the case of a small antenna configuration. In these respects, the presented work features a 4-port MIMO antenna design employing a low-cost substrate for WLAN, 5G NR (n79, n102, and n104), and C-band applications. Unlike many previously reported FR-4-based MIMO antennas that achieve either wide bandwidth, high isolation, or good radiation performance at the expense of the others, the proposed design simultaneously realizes wideband operation from 4 to 8 GHz, enhanced inter-element isolation, and stable radiation characteristics within a compact footprint. Methods such as partial ground structure and parasitic elements are applied to lower the coupling to minimize the degradation of MIMO antenna performance. The antenna design achieves high isolation, large impedance bandwidth, and reliable diversity performance, rendering it a strong choice for next-generation wireless communication systems. The designed antenna structure is analyzed in terms of S-parameters, and different diversity parameters validating its suitability for practical deployment.

2 Design Methodology

2.1 Single Antenna Element:

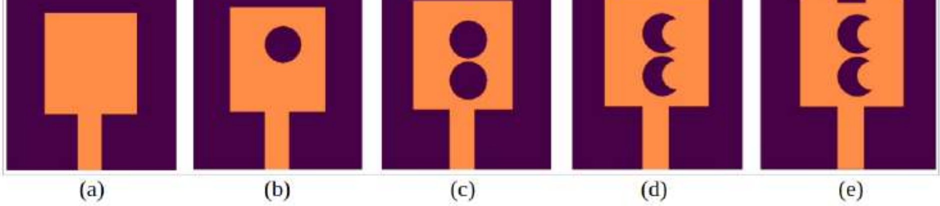

Figure 1: Evolution of single antenna element.

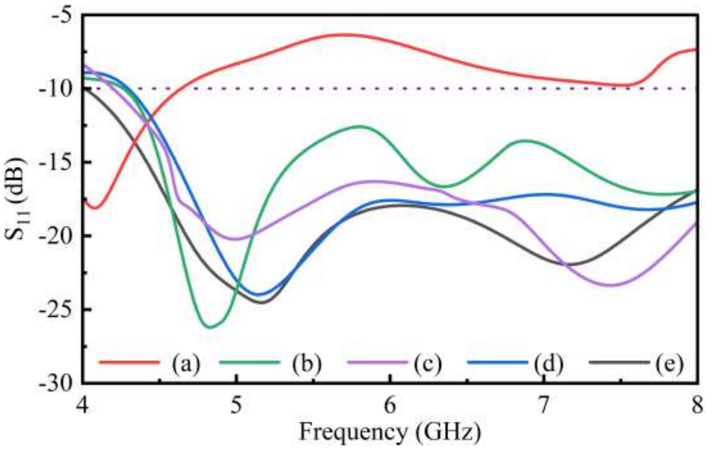

Figure 2: Variation of S11 of the antenna.

The antenna design process began with a conventional rectangular microstrip patch antenna, which serves as the reference structure due to its simple geometry and well-established characteristics. However, the basic rectangular configuration is typically constrained by limitations such as limited frequency coverage, reduced impedance matching, limited gain, and flexibility. Hence, geometrical modifications are introduced as shown in the Fig. 1. Fig. 2 shows the changes in the reflection coefficient value with the evolution of the antenna. The designed structure is implemented using cost-effective FR-4 substrate.

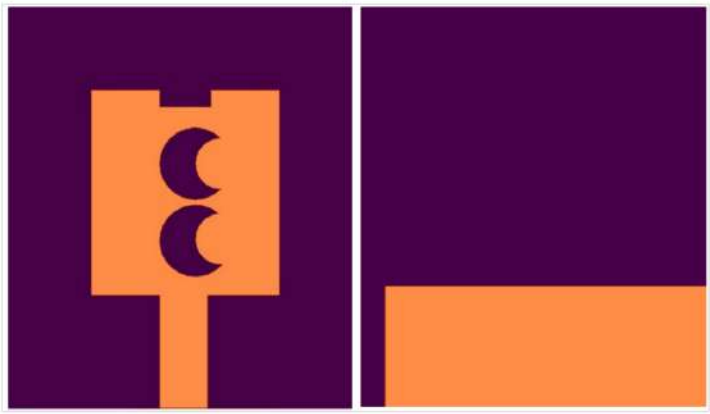

Figure 3: The single antenna element.

Fig. 3 displays the single-element structure of the proposed MIMO as well as the arrangement of the design geometry of the ground plane. Each radiating patch consists of two half-moon-shaped structures with a rectangular cut on the top plane of the structure. The modified rectangular patch is fed by a microstrip feedline. For the ground plane, a partial ground structure is adopted, which helps in reducing mutual coupling and enhancing isolation. Its dimensions are designed and optimized using the `ANSYS HFSS` (High Frequency Structure Simulator) software. Fig. 4 displays the S_{11} graph for the final single antenna element.

2.2 Quad-Element MIMO Design:

Fig. 5 presents the detailed geometry of the designed MIMO design, presenting the radiating elements and ground structure along with their corresponding design parameters. The initially designed single-antenna patch is positioned orthogonally to develop a four-port MIMO antenna as illustrated in Fig. 5(a). The parasitic elements used between each of the orthogonally arranged element helps to decrease the electromagnetic coupling between the

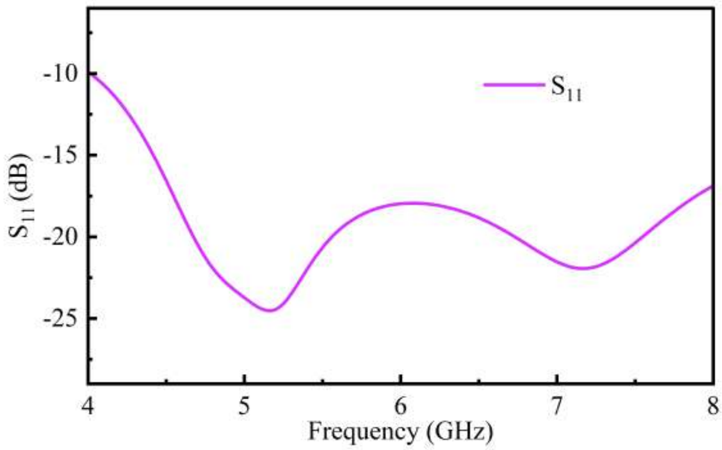

Figure 4: Return loss of the single antenna element.

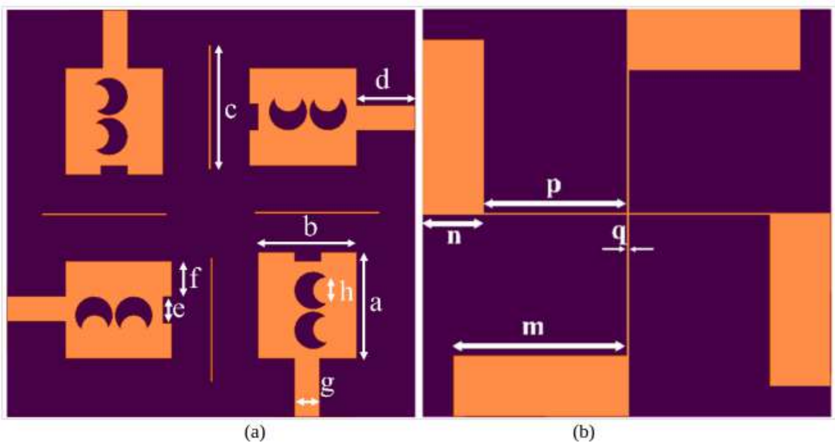

Figure 5: (a) Front and (b) back view of the 4-port MIMO.

present antenna components and suppress near-field coupling between adjacent radiators. The partial ground plane approach is adopted for the ground plane to increase the operational bandwidth of the design and disrupts surface current propagation [2]. A common reference level (common ground) is obtained by connecting the partial ground plane structures of all four ports with two thin neutralization lines, as seen in Fig. 5(b). Along with the partial ground plane structure and parasitic elements, neutralization lines are also implimented into the ground plane to lower the coupling and boost isolation. Table 1 displays the geometric dimensions of the planned structure.

Variables	**Dimensions**	**Variables**	**Dimensions**	**Variables**	**Dimensions**
a	12	e	3	m	15
b	11	f	4	n	6
c	14	g	3.2	p	12
d	6.6	h	2.9	q	0.2

Table 1: Geometric antenna variables with dimensions (in mm).

2.3 Field Distribution Analysis:

The electric and magnetic field distributions of the designed structure are presented in Fig. 6(a) and (b), respectively. Fig. 6(a) illustrates that when one port is excited, the strongest current concentration is observed around the excited radiating element. The high-intensity regions correspond to the areas of maximum electric field strength, while the gradual transition to blue regions indicates weaker fields along the ground plane and adjacent structures.

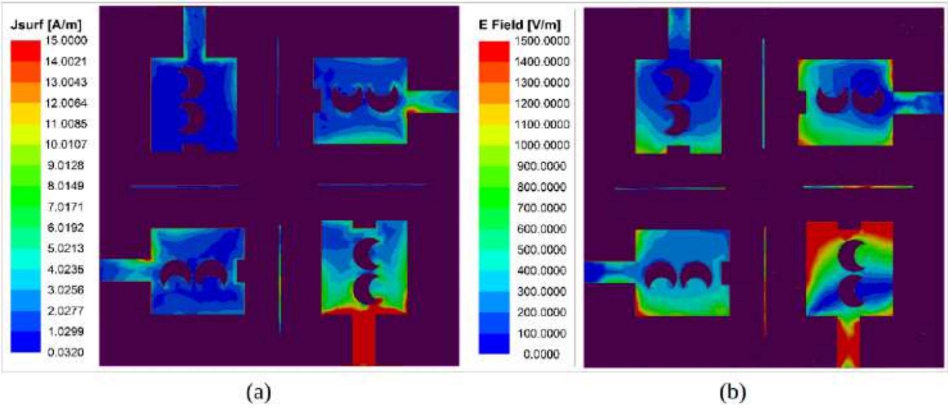

Figure 6: Surface current distribution of the design, (a) E-field and (b) H-field.

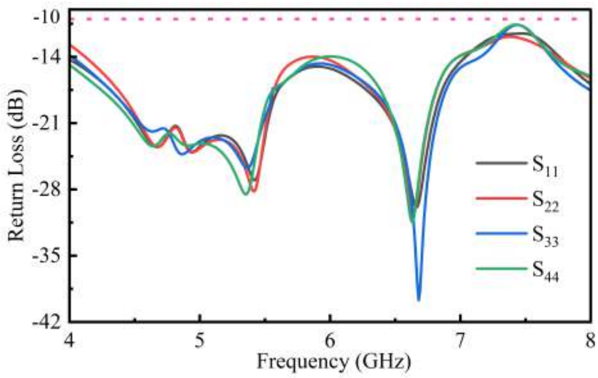

Figure 7: Return loss values of the 4-port MIMO.

The magnetic field distribution of the design structure is presented in Fig. 6(b), highlighting the concentration of the magnetic field around the current paths along the radiating elements. It can be observed that the maximum H-field intensity is concentrated near the feed and the excited radiating patch, confirming the effective excitation and radiation of the element. In addition, weaker magnetic field levels are observed around the non-excited elements, demonstrating the reduced field coupling between the ports. The application of the DGS effectively alters the field distribution and mitigates undesired interactions, thereby improving the isolation and stability of the designed compact MIMO antenna structure.

3 Results and Discussion

The acquired results from the simulation are analysed in this section. The reflection coefficients (S_{11}, S_{22}, S_{33}, and S_{44}) of the designed structure are presented in Fig. 7. The design covers the frequency range from 4 - 8 GHz. The S-parameters at ports 1, 2, 3, and 4 are -31.487 dB, -30.75 dB, -40.55 dB, and -31.76 dB, respectively. The reflection coefficient plot confirms that the antenna resonates around 5.45 GHz and 6.65 GHz, covering the desired frequency band with good impedance matching. The proposed antenna demonstrates strong return loss performance, achieving significantly higher reflection coefficient values (max. 35 dB) near the resonant frequencies. The plotted transmission coefficients indicate that the minimum (worst-case) port-to-port isolation remains better than -11.5 dB across the entire 4-8 GHz band, indicating efficient transmission and minimal reflection.

Fig. 8 presents the obtained transmission coefficients used to find the isolation among the antenna components. After using the parasitic elements, the value of isolation improved over -11.5 dB. The peak gain of the antenna is observed to be 7 dB with an efficiency greater than 80%, as presented in Fig. 9.

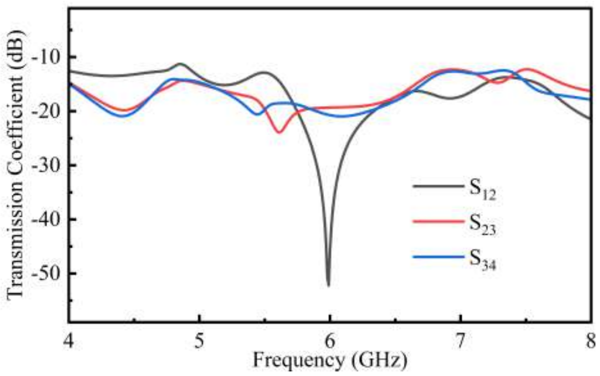

Figure 8: Transmission coefficients of the antenna.

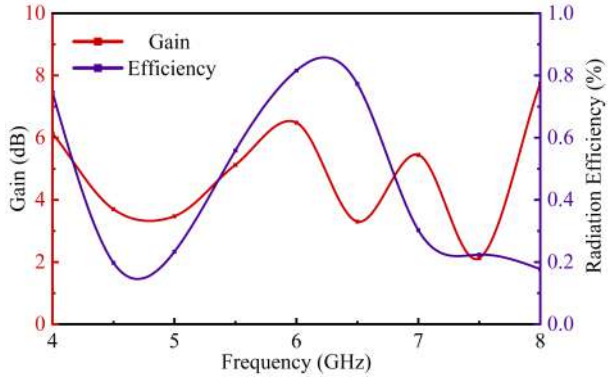

Figure 9: Gain and Efficiency of the Configuration.

4 MIMO Performance Parameters

Several diversity parameters are used to assess the performance of MIMO systems. One key metric for evaluating the interaction between radiating elements is the envelope correlation coefficient (ECC), which directly influences the channel capacity of the wireless configuration. Fig. 10 shows the calculated correlation of the proposed antenna, which is less than 0.011. Diversity gain (DG) is another important parameter that quantifies the improvement in signal reliability achieved through diversity techniques and reflects the effective reduction in transmission power requirements. It is given by the formula [1],

$$DG = 10\sqrt{1 - ECC} \tag{1}$$

and the DG value is found to be greater than 9.9992 dB.

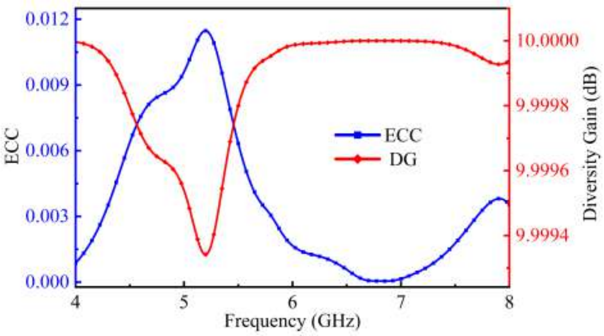

Figure 10: ECC and DG plots of the antenna.

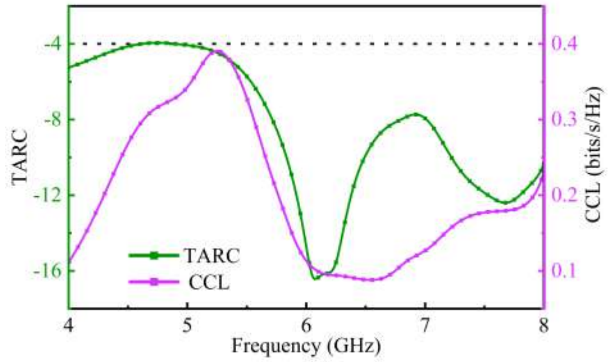

Figure 11: CCL and TARC plots of the design.

Another essential performance metric among the MIMO parameters is channel capacity loss (CCL). The suggested antenna design ensured less than 0.38 bits/s/Hz CCL value. TARC is used to verify the performance of a MIMO antenna by expressing the total incident power to the radiated power of the antenna. The TARC number should be ≤ 0 to emit the entire quantity of power properly [20]. Here, the CCL and TARC values of the introduced structure are presented in Fig. 11. These parameters are widely employed to ensure optimal system performance, as they provide insights into power distribution, mutual coupling effects, and overall channel efficiency.

All results are based on full-wave electromagnetic analysis because the goal of this work is to define the design process and validate the designed antenna structure through simulation. To verify the simulated performance empirically, the antenna will be manufactured and then measurement will be done using a VNA. Certain tolerances and material differences may have a little impact on the final performance during the practical manufacture of the suggested design, and manufacturing tolerances may cause variations in the copper cladding thickness. Small changes in the mutual coupling and slight differences in isolation may result from such adjustments. Furthermore, extra losses during measurement may be introduced by the parasitic effect caused by soldering flaws and SMA connectors. Slight variations in performance can also be brought on by environmental elements like humidity and temperature. These factors were taken into consideration during the design optimization process, and following the fabrication of prototypes and experimental characterization, they will be further investigated.

Table 2 comprises the performance characteristics of the proposed antenna structure and the various antenna structures mentioned in the literature.

Ref.	Substrate	Frequency (GHz)	Gain (dB)	Efficiency (%)	ECC	DG (dB)	TARC	CCL (bits/s/Hz)
[6]	FR-4	1.6–4.4	5.62	53	0.001	9.9	–	0.4
[9]	F4B	2.4–2.65	9.25	92	0.05	–	–	–
[21]	FR-4	3.78–9.5	3.78	81	0.04	9.997	–	–
[22]	FR-4	3.81–7.48	4.6	–	0.01	–	-10	0.4
[23]	FR-4	5.68–8.01	2.5–6.5	90	0.001	–	–	–
[24]	FR-4	2–5.2	6.3	–	0.01	10	-20	0.05
[25]	Rogers RT 5870	5.65–6.55	5.2	–	0.046	–	–	0.0758
[26]	Rogers-5880	5.2–5.7	3.05	90	0.007	9.96	-10	0.4
[27]	Rogers-5880	3.08–7.75	8.3	73–84	0.004	9.98	–	–
This work	**FR-4**	**4–8**	**7**	**87**	**0.011**	**9.9992**	**-16**	**0.38**

Table 2: Performance comparison of the designed MIMO with recent works.

5 Conclusion

The proposed work presents a small-sized quad-element MIMO design for 5G wireless applications. The prototype of the antenna structure is designed and optimized using a cost-effective FR-4 substrate. For the reduction of inter-element coupling partial ground structure is used. The MIMO design comprises four radiating patches facing each other. Each contains two half-moon shaped structure with a rectangular cut at the top of the radiating element. The defected ground structure method and the neutralization line are introduced to decrease the inter-element interaction between the radiating components. The designed antenna also uses parasitic elements for the same purpose. This approach enhances isolation between the radiating elements as isolation coefficients are less than -11.5 dB. The value of ECC is found to be less than 0.011, indicating that the coupling of the antenna is very low. The value of CCL is 0.38 bits/s/Hz. In addition, diversity gain is greater than 9.9992. These characteristics make the proposed antenna structure well-suited for the 5G NR n79, n102, and n104 bands. The present work is limited to the design and full-wave simulation of a four-element antenna structure. Fabrication and measurement of the designed antenna will be carried out in future studies to provide experimental validation of the simulated performance.

Acknowledgements

The authors sincerely acknowledge the DST FIST (level-I) Project No (SR/FST/PSI-217/2016) and the DST PURSE Project No (SR/PURSE/2022/143) and funding by Department of Science Technology, Govt. of India to the Department of Physics, Dibrugarh University, Assam, India.

References

[1] A. C. Balanis and D. R. Cockrell, IEEE Trans. Aerosp. Electron. Syst. **AES-7**, 960 (1971).

[2] M. Alibakhshikenari *et al.*, Sci. Rep. **12**, 7907 (2022).

[3] V. K. Gupta and R. Baru, in *Advances in Intelligent Computing and Communication. Lecture Notes in Networks and Systems, Vol. 202*, edited by S. Das and M. N. Mohanty (Springer, Singapore, 2021), pp. 199–209.

[4] H. Xing *et al.*, Electronics **9**, 1265 (2020).

[5] T. Doloi *et al.*, in *2024 15th International Conference on Computing Communication and Networking Technologies (ICCCNT)* (2024), pp. 1–6.

[6] G. Shankar Das *et al.*, Mater. Today Proc. (2023), *article in press*.

[7] W. Wu, B. Yuan and A. Wu, Int. J. Antennas Propag. **2018**, 8490740 (2018).

[8] Y. Li *et al.*, IEEE Trans. Antennas Propag. **67**, 3820 (2019).

[9] Y.-F. Cheng and K.-K. M. Cheng, IEEE Trans. Antennas Propag. **69**, 8204 (2021).

[10] H. Jiang *et al.*, in *2019 International Conference on Microwave and Millimeter Wave Technology* (ICMMT, 2019), pp. 1–3.

[11] W. Hu *et al.*, IEEE Access **7**, 153910 (2019).

[12] A. A. Megahed *et al.*, IEEE Access **10**, 19875 (2022).

[13] A. Birwal *et al.*, MAPAN **36**, 763 (2021).

[14] M. Abdullah, S. H. Kiani and A. Iqbal, IEEE Access **7**, 134488 (2019).

[15] P. Mathur *et al.*, IEEE Access **9**, 106734 (2021).

[16] J. Acharjee, K. Mandal and S. K. Mandal, AEU–Int. J. Electron. Commun. **97**, 110 (2018).

[17] S. Chakraborty *et al.*, SN Appl. Sci. **2**, 1180 (2020).

[18] S. Mathew, G. Saini and S. S. Gill, Int. J. Recent Technol. Eng. **9**, 202 (2020).

[19] K. Ding *et al.*, IEEE Antennas Wireless Propag. Lett. **16**, 2349 (2017).

[20] T. Doloi *et al.*, Phys. Scr. **99**, 105013 (2024).

[21] N. Das *et al.*, in *2023 International Conference on Electrical, Computer and Communication Engineering (ECCE)*, (IEEE, 2023), pp. 1-6.

[22] B. M. Yousef *et al.*, AEU–Int. J. Electron. Commun. **170**, 154815 (2023).

[23] Z. Wang, M. Wang and W. Nie, Electronics **12**, 3465 (2023).

[24] S. Hassan Ghadeer *et al.*, AEU–Int. J. Electron. Commun. **159**, 154480 (2023).

[25] M. Mishra *et al.*, IEEE Access **10**, 49829 (2022).

[26] A. Ali *et al.*, Ain Shams Eng. J. **15**, 102579 (2024).

[27] M. M. Hasan *et al.*, Sci. Rep. **12**, 9433 (2022).

COHERENCE OF THE LIGHT FROM THE INDIAN FIREFLY ASYMMETRICATA CIRCUMDATA

Amlan Jyoti Borah[*1] and Anurup Gohain Barua[1]

[1]*Department of Physics, Gauhati University, Guwahati-781014, India*

[*]Corresponding Author: amlanjyoti001@gmail.com

(Received 26 September 2025; revised 4 January 2026; accepted 7 March 2026; published 1 August 2026)

Abstract: Numerous investigations conducted on firefly bioluminescence over the past few decades have improved our knowledge of the intriguing phenomenon that produces light. Different studies have also demonstrated the influence of external environmental elements on the light emitting reaction. In this article, interference fringes from the light of the Indian firefly *Asymmetricata circumdata* produced using a Michelson interferometer are presented. The fringes vanish when the path difference of interfering beams equals or exceeds 30 cm, indicating that the light of this firefly species maintains a stable phase up to a path difference of 30 cm.

Keywords: Firefly bioluminescence, Asymmetricata circumdata, Interference, Michelson interferometer, Temporal coherence.

PACS: 78.60.Ps, 42.25.Hz, 42.55.Zz, 07.60.Ly, 87.64.kv

1 Introduction

Fireflies are an amazing creation of mother Nature that can produce light by their own. They use this light to locate mates or to scare predators or attract preys [1, 2]. A chemical reaction that is approximately 41% efficient [3, 4] is responsible for light production in fireflies. In this reaction, luciferin (a luminophore), luciferase (an enzyme), Mg^{2+}, ATP and molecular oxygen take part. Initially, luciferin gets oxidised to form oxyluciferin in an excited state, which releases visible light during relaxation to ground state [5]. Reaction steps are summarised in Fig. 1.

$$D-luciferin + ATP \xrightarrow{Luciferase,\, Mg^{2+}} Luciferase - luciferyl\ adenylate + Pyrophosphate$$

$$\Big\downarrow +O_2 \quad Luciferase$$

$$Oxyluciferin^{*} + CO_2 + AMP + H^{+}$$

$$\Big\downarrow$$

$$Oxyluciferin + Light$$

Figure 1: Bioluminescence reaction that produces light in fireflies. Due to its high efficiency, this light is also referred to as cold light.

In the bioluminescence (BL) reaction in fireflies, neural signals regulate whether a flash is emitted or not [6, 7]. The reaction is affected by any external environmental factors. Among different factors, the most influential one is temperature [8–12]. At lower temperatures than normal one, the BL reaction becomes slower- making the reaction start and end very slowly and emits broad flashes [13]. Below a certain low temperature, flash duration increases exponentially and a blue shift of peak wavelength is also discernible. This happens due to cold denaturation of luciferase. Conversely, rate of the reaction becomes faster at higher temperatures. At a certain hot temperature, a red shift of peak wavelength is visible and shortest flashes are obtained. This is known as thermal denaturation. Above this temperature, flashes again start to broaden. The temperatures ranges for thermal and cold denaturation are species specific. Fireflies keep a safe margin from temperatures at which denaturation happens- they appear at least 5–7$°C$ higher than cold denaturation temperature and at least 3–4 $°C$ lower than thermal denaturation temperature. Temperatures within these two limits are favourable for fireflies. In the firefly species *Abscondita perplexa* (previously named as *Luciola praeusta*), widely found in northeastern India, the thermal and cold denaturation temperatures are 42 and 11.5–11.0 $°C$, respectively [12, 13], which makes them capable of appearing from March to November just after sunset. On the other hand, for *Schlerotia substriata*, these values are 34 and 10.5–9.0 $°C$, respectively [10], making them appear about one to one and a half hour after sunset in the same location. Other external factors affecting BL reaction are magnetic and electric fields. In Japanese firefly species *Luciola cruciata* and *Luciola laterialis*, both the pulse density and frequency were found to increase under the influence of external pulsed magnetic field suggesting that the magnetically induced current inside the firefly affected its nervous system or the photochemical process in the light organ [14]. In static electric field, though the firefly species *A. perplexa* showed no variation in peak-wavelength position, but its flashes broadened twice in males and thrice in females and no variation was observed in alternating field [15]. Therefore, it was concluded that the static electric field probably removed free electrons from the cuticle layer, which in turn carried away some heat from the firefly making it cool, which in turn slowed the reaction rate and made flashes broad. In a recent article, it is reported that biting by a spider alters male flashes to mimic with those of females [16].

Investigations made on the internal structure of the firefly light-emitting organ reveal the presence of uric acid granules, which behave like a cavity similar to that present in a random laser [17]. Another report about a laser-like emission in specimens of the firefly *A. perplexa* is also available [18]. The temporal coherence length measured for this species is 23 cm [19]. *Asymmetricata circumdata* is another firefly species that coexists with *A. perplexa*. Therefore, its coherence property has been measured for comparison.

2 Materials and methods

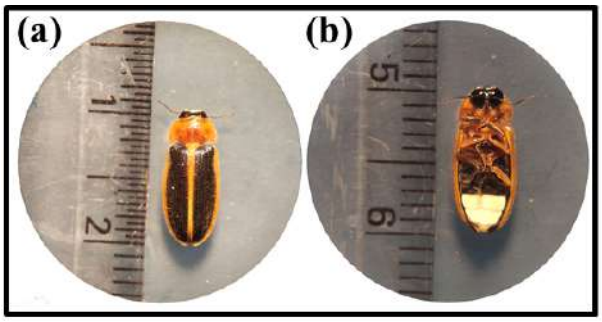

Figure 2: Photographs showing a male specimen of the firefly species Asymmetricata circumdata in (a) dorsal and (b) ventral views. The presence of two white segments in the abdomen confirms it as a male.

Among the four firefly species identified on the Gauhati University campus (26.1540° N, 91.6630° E), *Abscondita perplexa* has the highest population, and *Asymmetricata circumdata* is second in the list, followed by the other two species- *Diaphanes sp.* and *Schlerotia substriata*. Fireflies of the species *A. circumdata* appear 1.5 to 2 hours after sunset and thus are dark-active. It is very difficult to catch females of this particular species. Catching of a few males is somewhat less difficult. A mature firefly is approximately 1 cm long, as shown in Fig. 2. For the experiment, 10 healthy male specimens were collected using a specially designed net. Before the experiment, fireflies were kept in the dark laboratory in a bottle with good air flow. Acclimatised fireflies were then fixed with a beam expander using cotton and sellotape. A Michelson interferometer was used to form interference fringes. The experimental setup is presented in Figure 3. Snapshots of fringes were captured using DSLR (`NIKON D7000`) camera with a lens (`AF-S NIKKOR 24-120 mm 1:4 G ED`).

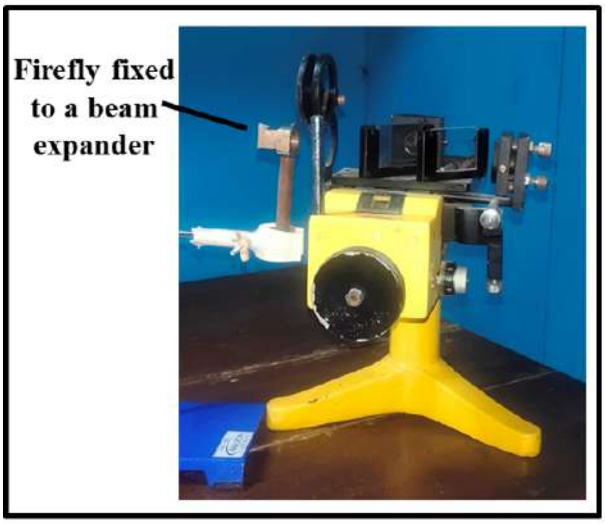

Figure 3: A photograph showing a Michelson interferometer. The point-like light of the firefly is expanded to obtain interference fringes on this interferometer.

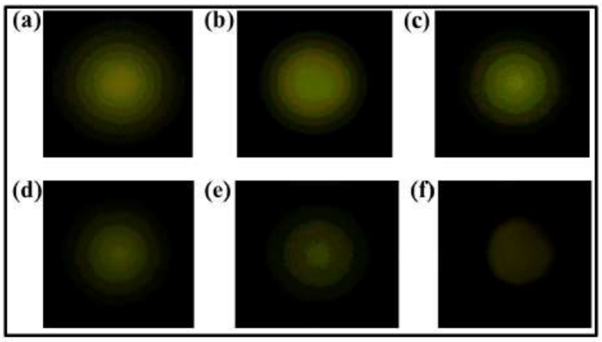

Figure 4: Snapshots of interference fringes at different path differences. (a) Fringes are formed at zero path difference. (b) to (f) Path differences are set at 8, 16, 24, 30, and 31 cm, respectively.

3 Results and discussion

Interference fringes formed at different path differences are presented in Fig. 4. Since firefly light is polychromatic- a mixture of three colours, viz. green, yellow, and red [20]- we get colourful fringes. Due to the overlapping of different ordered fringes for these colours, completely dark fringes are absent. When there is no path difference, the number of rings in the interference fringes is maximum. With increasing path difference, the number of interference rings decreases. It is found that at a path difference of 30 cm, the minimum number of rings is obtained, and interference fringes start disappearing hereafter. No fringes were obtained at a path difference of 31 cm.

4 Conclusion

Light of the firefly *A. circumdata* is found to interfere in a Michelson interferometer to form circular rings. The disappearance of interference rings at a path difference exceeding 30 cm confirms a better coherence length of this species in comparison to that of the species *A. perplexa*. Hence, it can be concluded that the light of *A. circumdata* is much more monochromatic.

Acknowledgements:

We thank the Institutional Animal Ethical Committee (IAEC) of Gauhati University for according permission to use specimens of the firefly species.

References

[1] S. M. Lewis and C. K. Cratsley, Annu. Rev. Entomol. **53**, 293 (2008).

[2] B. N. Balaji *et al.*, *Animal Diversity: Taxonomical and Physiological Aspects* (M/S Academic Publishers & Distributors, Lucknow, 2023) p. 183.

[3] Y. Ando *et al.*, Nature Photon. **2**, 44 (2007).

[4] K. Niwa *et al.*, Chem. Lett. **39**, 291 (2010).

[5] O. Shimomura, *Bioluminescence: Chemical Principles and Methods*, revised ed. (World Scientific, Singapore, 2012).

[6] H. A. Robertson and A. D. Carlson, J. Exp. Zool. **195**, 159 (1976).

[7] T. A. Christensen *et al.*, Neuroscience **9**, 183 (1983).

[8] U. Sharma *et al.*, Photochem. Photobiol. Sci. **13**, 1788 (2014).

[9] U. Sharma *et al.*, J. Photochem. and Photobiol. B **161**, 383 (2016).

[10] M. M. Rabha *et al.*, Sci. Rep. **11**, 12498 (2021).

[11] M. M. Rabha *et al.*, J.Biosci. **45**, 61 (2020).

[12] A. J. Borah *et al.*, Optik **281**, 170826 (2023).

[13] M. M. Rabha *et al.*, J. Photochem. Photobiol. B **170**, 134 (2017).

[14] M. Iwasaka *et al.*, J. Appl. Phys. **109**, 07B303 (2011).

[15] A. J. Borah and A. Gohain Barua, Photochem. Photobiol. **00**, 1 (2025).

[16] X. Fu *et al.*, Curr. Biol. **34**, R768 (2024).

[17] K. S. Goh *et al.*, PLoS ONE **8**, e56406 (2013).

[18] A. Gohain Barua *et al.*, J. Biol. Phys. **40**, 267 (2014).

[19] U. Sharma *et al.*, Curr. Sci. **114**, 637 (2018).

[20] N. Dehingia *et al.*, Curr. Sci. **99**, 1425 (2010).

EFFECT OF FINITE BARYON DENSITY IN FREE ENERGY CALCULATION UNDER ONE-LOOP CORRECTION

S. Somorendro Singh*[1]

[1]*Department of Physics and Astrophysics, University of Delhi, Delhi - 110007, India*

*Corresponding Author: sssingh@physics.du.ac.in

(Received 19 September 2025; revised 10 March 2026; accepted 27 March 2026; published 1 August 2026)

Abstract: The free energy evaluation is studied under one-loop correction at finite baryon density. The finite baryon density in this one-loop correction results in bubble/droplet formation achieved with quark and gluon parametrization in the range of $\gamma_q = 1/8$ and $8\gamma_q \leq \gamma_g \leq 18\gamma_q$. Stable droplets are specifically realized when the quark and gluon parameterizations satisfy $\gamma_q = 1/8$ and $12\gamma_q \leq \gamma_g \leq 16\gamma_q$. So this baryon density enhances the stability of the droplets of quark-gluon plasma (QGP) with a smaller size. This implies that incorporating finite baryon density into the free energy calculations provides significant insights into QGP formation. Therefore, the model with one-loop correction at finite baryon density is suitable for describing QGP signals.

Keywords: Quark-gluon Plasma; Quark-Hadron phase transition; Quantum chromodynamics; Free energy

PACS: 12.38 Mh; 12.29 Pn; 25.75Ld

1 Introduction

The strong interaction theory called ”Quantum Chromodynamics” (QCD) can describe characteristic features of coloured quarks and gluons. QCD frameworks predict a distinct phase transition where these colored, unconfined quarks and gluons condense into color-neutral bound states known as hadrons. [1, 2]. This change of nature is believed to occur under extreme conditions of high nuclear density or very high temperature. So, the matter formed in these two extreme conditions is designated as the quark-gluon plasma (QGP). Because QGP states are highly transient and short-lived, tracking and predicting their behavior remains a complex task. Nevertheless, investigating such challenging phenomena is a common pursuit to uncover their inner nature. So, the topic is a burning candidate for investigation of these phases. Globally, several specialized experimental centers study these phases, notably the Relativistic Heavy-Ion Collider (RHIC) at BNL and the Large Hadron Collider (LHC) at CERN. Complementing these major operations, newer research facilities like FAIR at Darmstadt and NICA at Dubna are explicitly configured to explore physics at compact baryon densities [7, 8]. These specialized laboratories prioritize the investigation of dense baryonic matter. For instance, Baryonic Matter at Nuclotron (BM@N) experiments utilize high-energy ion beams from the Nuclotron to recreate particle production conditions mirroring the early universe's evolution. Again, from lattice's point, there is report of involving the finite baryon density in the study of QGP formation [9, 10]. However, the facilities available to these experiments will also provide the detailed news of the early universe phase transition, quark-gluon plasma droplet formation, and phase structure picture of QCD [11–14].As a result, modeling QGP within ultra-relativistic heavy-ion collisions stands out as a frontier area in modern collider physics , drawing intense interest from theorists and experimentalists seeking to leverage baryon density as a key dynamical variable. QGP signatures are expected to manifest near the convergence of high baryonic density and temperature, where both distinct phases coexist [15, 16]. There is also information about QGP formation at the convergence of baryonic density and temperature, where both phases exist [17]. In this short paper, the calculation of free energy evolution is concentrated with the effect of finite baryon density under the purview of one-loop corrections. The underlying baryon density is directly determined by the total population of charged particles within the thermodynamic system. Given contemporary paradigms of

QGP evolution, the presence of these finite baryon densities cannot be disregarded. It has been experimentally observed that the high-speed particles are the charged particles. Based on this information, laboratories like CBM (compact baryon matter) in Darmstadt, Germany are established for the detail study about these charged particles. So, the consideration of finite baryon density in the present calculation is reasonable in the context of phenomenological studies. To determine the free energy, we construct a thermodynamic partition function that establishes a link between Gibbs free energy and finite baryonic density. The one-loop corrected partition function within the mean-field potential framework is adjusted by redefining the density of states to accommodate baryonic density factors. This modified density of states is formulated via dynamic quark and gluon flow parameters, where the effective quark masses are shifted by both the baryon density and loop corrections. Consequently, the free energy expansion of the expanding QGP fireball varies with the quark and gluon flow parameters, modifying droplet stability across different flow conditions [18–20]. These flow parameters are critical in determining how stable droplets or bubbles develop as the system's temperature rises. Again, one of the most successful model to explain about the description of QGP formation is the relativistic hydrodynamics, which provides the quantitative pictures of heavy-ion collision dynamics [21–23] However, the hydrodynamic approach tends to yield next generation approximations for better model- data agreement [24, 25].

Briefly, the density of states at finite baryon density is restudied and next evaluate the free energy computing the free energy evolution by incorporating one-loop effects alongside the quark and gluon flow parameters. In the evaluation, the quark mass is considered with temperature and baryon density dependence. So the temperature is taken in such a way that QGP-phase transition is normally observed during temperature $(150 - 270)$ MeV and due to it, the bubble/droplet formation is observed within the range of these temperatures. However, the baryon density is considered on a random choice with the scale of temperature at which the appropriate value of the baryon density may be achieved. Now we look at the changes in the free energy produced by this.

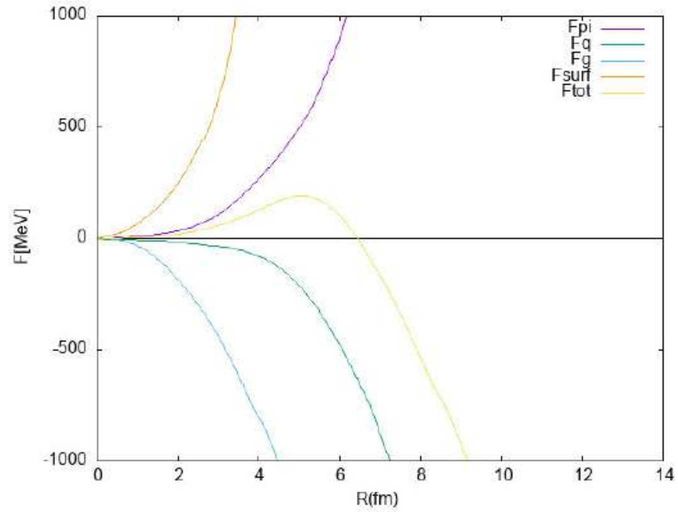

Figure 1: Free energy graph of individual particles vs. R at $\gamma_q = 1/8$, $\gamma_g = 12\gamma_q$ for particular temperature $T = 170\ MeV$ and baryonic chemical potential $\mu_B = \mu/3$ where, $\mu = 300$ MeV.

2 Density of state with one-loop correction at finite baryon density

The density of states of the present calculation is obtained through the potential model. The interacting potential defined at this finite baryonic density is obtained through the extension of earlier one-loop correction potential [26–28]. However, the idea of potential interaction is brought from the static potential to dynamical quarks as it has a finite value depending on the temperature, which can play a little role in influencing the potential between quarks and anti-quarks. While the static potential originates from heavy quark masses and the system is under the influence of high and baryonic density. Due to it, the dynamic quark mass is perturbed by high temperature and chemical potential. So its value has been compared to the heavy quark mass and the interaction potential of these

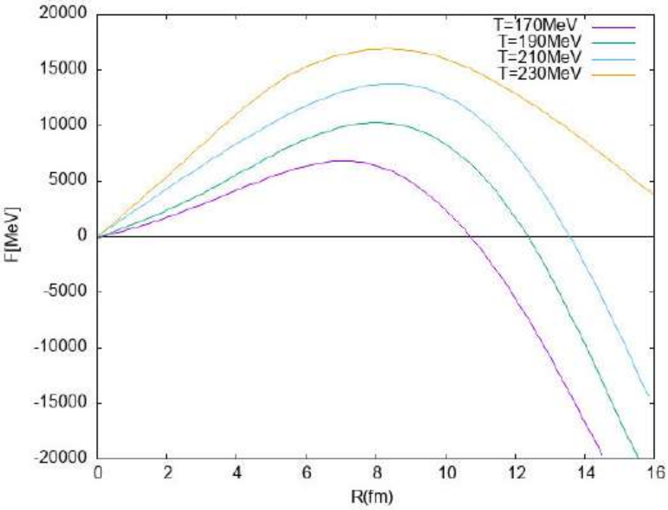

Figure 2: Total free energy versus R the size of the droplet at $\gamma_q = 1/8$, $\gamma_g = 8\gamma_q$ and $\mu_B = \mu/3$ where, $\mu = 300\ MeV$ for various temperatures.

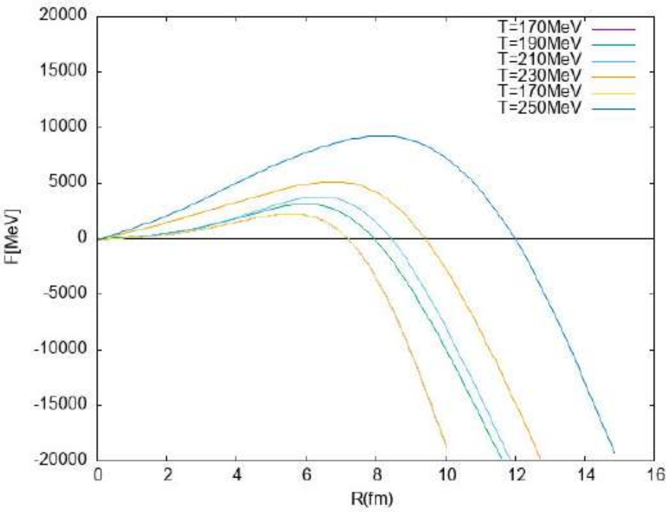

Figure 3: Total free energy versus R the size of the droplet at $\gamma_q = 1/8$, $\gamma_g = 10\gamma_q$ and$\mu_B = \mu/3$ where, $\mu = 300\ MeV$ for various temperatures.

modified quark masses has been obtained. It is now expressed as:

$$V(p,\mu) = \frac{8\pi}{p}\gamma\alpha_s(p,\mu)(T^2+\mu^2/\pi^2)[1+\frac{\alpha_s(p,\mu)}{4\pi}b_1] - \frac{m_0^2}{2p} \quad (1)$$

where γ represents the RMS (root mean square) value of the quark and gluon flow parameters say $\gamma_q = 1/8$ and $\gamma_g = (8-16)\gamma_q$. $\alpha_s(p,\mu)$ is defined as done in earlier papers. It is:
$\alpha_s(p,\mu) = \frac{4\pi}{29\ln[1+(p^2+\mu^2)/\Lambda^2]}$ in which Λ is the quantum chromodynamics parameter normally taken as $150\ MeV$. μ is taken in terms of baryon chemical potential as $\mu = 3\mu_B,\ \mu_B$ is finite baryon chemical potential. b_1 is the one-loop correction factor, which is defined as

$$b_1 = 2.5833 - 0.2778n_l \quad (2)$$

where n_l is light quark numbers of flavor $2+1$ as u,d and s [29, 30]. So using this potential we obtain the density of state as:

$$\rho(p) = \frac{v}{\pi^2}[\frac{\gamma^3(T^2+\mu^2/\pi^2)}{2}]^3 g^6(p)A \quad (3)$$

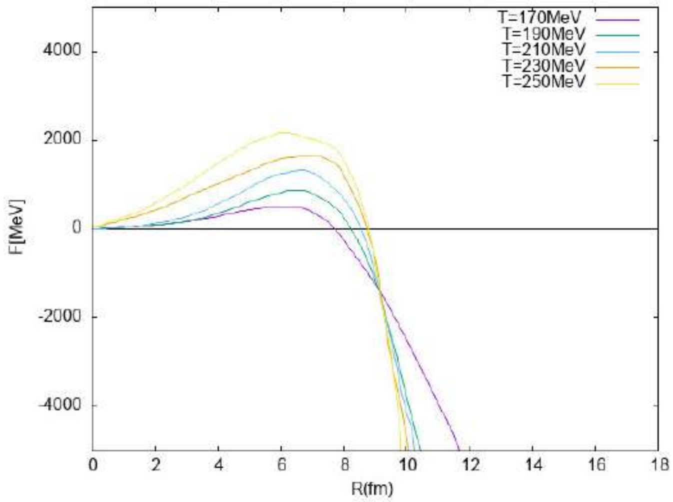

Figure 4: Total free energy vs. R the size of the droplet at $\gamma_q = 1/8$, $\gamma_g = 12\gamma_q$ and $\mu_B = \mu/3$ where, $\mu = 300\ MeV$ for different temperatures.

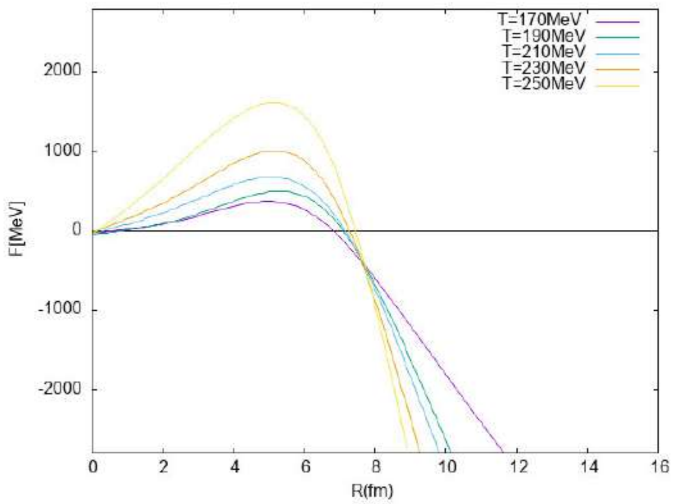

Figure 5: Total free energy vs. R the size of the droplet at $\gamma_q = 1/8$, $\gamma_g = 14\gamma_q$ and $\mu_B = \mu/3$ where, $\mu = 300\ MeV$ for various temperatures.

Eq. (3) defines the modified density of states in phase space, revised to incorporate one-loop corrections within an interacting potential at a finite baryonic chemical potential μ_B. It is really obtained through reviewing our earlier paper on one-loop corrections. In the expression, v is the QGP occupied volume. $g^2(p) = 4\pi\alpha_s(p,\mu)$ and A is a factor of one-loop coupling constant obtained in simplifying the density of state through the potential in the above expression (1). It is found as:

$$A = \{1 + \frac{\alpha_s(p,\mu)b_1}{\pi}\}^2[\frac{(1+\alpha_s(p,\mu)b_1/\pi)}{p^4} + \frac{2(1+2\alpha_s(p,\mu)b_1/\pi)}{p^2(p^2+\Lambda^2)\ln(1+\frac{p^2+\mu^2}{\Lambda^2})}] \tag{4}$$

3 Thermodynamic free energy at finite baryon density

The relevant thermodynamic potential can be constructed by knowing the temperature, the finite baryon density and the Hamiltonian of the system. So the partition function of the system is defined in a number of literature is as [31]

$$Z(T,\mu,V) = Tr\{exp[-\beta(\hat{H} - \mu\hat{N})]\} \tag{5}$$

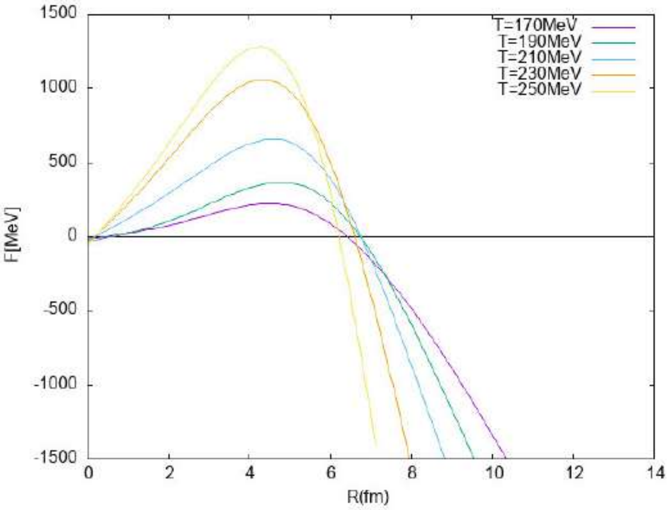

Figure 6: Total free energy vs. R the size of the droplet at $\gamma_q = 1/8$, $\gamma_g = 16\gamma_q$ and $\mu_B = \mu/3$ where, $\mu = 300\ MeV$ for various temperatures.

where $\beta = \frac{1}{T}$, μ represents the chemical potential expressed relative to the baryon chemical potential ($\mu = 3\mu_B$), $\hat{N}$ denotes the quark number operator, and T is the temperature. Now it is co-related the Gibbs free energy using the partition function. It is related in this way as [32–34]:

$$F_i = T \ln Z(T, \mu, V) \tag{6}$$

The free energy evolution is subsequently established by integrating the density of states with the appropriate Fermi-Dirac and Bose-Einstein distribution functions for fermions and bosons, respectively:

$$F_i = \pm T g_i \int \rho_{q,g}(p) \ln[1 \mp e^{-(\sqrt{m_i^2+p^2}-\mu)/T}]dp\ , \tag{7}$$

In this formulation, the quark mass depends explicitly on both temperature and finite baryon density. The term g_i accounts for the degeneracy factors associated with color and particle-antiparticle degrees of freedom for quarks and gluons. The term $\rho_{q,g}$ denotes the phase-space density of states modified by one-loop corrections within the interaction potential at baryon density μ_B. Integrating these factors across the free energies of fermions and bosons allows us to map the dynamics of the QGP flow. In addition to these bulk free energies, we incorporate an interfacial energy term to account for hydrodynamic movements within the medium, alongside a Bag energy constant to enforce confinement. This surface term is also evaluated using the root mean square flow parameters of quarks and gluons: [35, 36].

$$F_{interface} = \frac{\gamma T R^2}{4} \int p^2 \delta(p - T) dp, \tag{8}$$

In the above equation, γ is already defined in eq. (1) This parameter controls the QGP fluid dynamics and is introduced when interfacial energy forms to counterbalance the bag energy pressure, where R signifies the radius of the QGP droplet. To account for the hadronic phase, the free energy contributions from medium-mass hadrons (which dominate the reaction zone with degeneracy factor g) are given by: [37]:

$$F_h = (gT/2\pi^2)\nu \int_0^\infty p^2 \ln[1 - e^{-(\sqrt{m_h^2+p^2}-\mu/T)}]dp. \tag{9}$$

where m_h represents the mass of the corresponding hadronic species. These hadrons are considered to be medium-mass hadrons as they are the dominant factor in the reaction zone. Finally, all these contributed free energies are added and then the total modified free energy F_{total} is computed as:

$$F_{total} = \sum_i F_i\ +\ F_{interface}\ +\ F_h, \tag{10}$$

where index i runs over u, d, s quarks, and gluons.

4 Results

This section presents numerical solutions to the free energy expressions derived from our potential-based density-of-states model. The Fig. 1 demonstrates the free energies of the individual participants e.g quarks, gluons, interfacial, the most dominant contribution pions among the hadrons. So the corresponding plots of the individual particles present in the figure show the energy evolution carried by these particles. Then the figure is traced at the choice of baryonic chemical potential $\mu_B = \mu/3$ where, $\mu = 300\ MeV$ and at temperature $T = 170\ MeV$. This temperature is generally taken as the transition temperature. Then it tries to represent the free energy summing up all the contributions of the involved particles together in this Fig. 1. However, in considering all the particles among hadrons, it is taken only few of particles having less masses than $1000\ MeV$ of hadrons as these masses contributed somewhat more in comparison to other massive hadrons in the reaction zone. So the Fig. 2 is plotted for all these contributed particles of hadrons, quarks, gluon and interface. This combined free energies indicate the droplet formation of different sizes according to the different temperatures at quark and gluon parameters $\gamma_q = 1/8$ and $\gamma_g = 8\gamma_q$. At this particular parameter the droplets are formed at the different temperatures and there is no stability in the droplet of QGP bubbles. With the increasing temperature, the size of the droplet increases at this finite baryonic chemical potential with the same flow parameter.

Again, in Fig. 3, the free energy vs the size of droplet is plotted at the quark flow parameter fixed at $\gamma_q = 1/8$ and increased gluon flow parameter to $\gamma_g = 10\gamma_q$. At such a parameter the droplets/bubbles are found but they are still unstable droplet at this baryon chemical potential $\mu_B = \mu/3$ with $\mu = 300\ MeV$ with smaller sizes. It indicates that the droplet size is still visible in obtaining smaller droplets with the fixed quark and increased gluon flow parameters. Then it is further searched to find suitable stable droplets of QGP with an ad-hoc search of gluon parameters in Fig. 4 to 6. In these figures, the stable droplets are able to find at a slight different value of gluon flow parameter. In Fig.4 the stable droplet is seen with the size of the droplet around $9\ fm$ at $\gamma_q = 1/8$ and $\gamma_g = 12\gamma_q$. It indicates that there is stable drop of QGP if there is a suitable choice of the gluon flow parameter. Again in Fig.5 the same situation is obtained with slightly changed in the size of droplets. The size is found to be around $8\ fm$ with the marginal change of the gluon flow parameter at $\gamma_g = 14\gamma_q$. It shows that the droplet is more stable with the increase of temperature with increased gluon parameter. In Fig.6, the gluon flow parameter is increased a little and there is a slight change in the stability of the droplet. It implies that the stable droplets are not able to obtain for any range of gluon flow parameter beyond this value, $\gamma_g = 14\gamma_q$. It says that the stable/unstable droplets are obtained in a particular range of the gluon parameter say $\gamma_q = 1/8$ and $12\gamma_q \leq \gamma_g \leq 16\gamma_q$ Beyond this window, the QGP droplet dynamics become highly turbulent across variations in temperature and chemical potential. Stable fluid configurations are strictly locked within the narrow range of $12\gamma_q \leq \gamma_g \leq 14\gamma_q$. This localized stability stems from the temperature and chemical potential dependence embedded in the quark masses via the one-loop corrected potential model. Hence, incorporating a baryonic chemical potential alongside one-loop corrections is capable of generating stable, equilibrium droplets in QGP flow profiles.

Therefore, as a final remark, a one-loop correction considering a baryonic chemical potential can generate an equilibrium/stable droplet in the flow dynamics of QGP.

To summarize, by building upon our established one-loop calculations and introducing a finite baryonic chemical potential, we have shown that stable droplet configurations remain a viable outcome in QGP hydrodynamics.

5 Conclusion

We have demonstrated that the simultaneous inclusion of a finite baryonic chemical potential and one-loop corrections to the mean-field potential leads to distinct windows of stability and instability in droplet formation. These states are sensitive to the chosen quark and gluon flow parameters, spanning the range $\gamma_q = 1/8$ and $12\gamma_q \leq \gamma_g \leq 16\gamma_q$. In particular, robust equilibrium stability is achieved when $12\gamma_q \leq \gamma_g \leq 14\gamma_q$, with the resulting droplet sizes showing an expansion relative to models using uncorrected potentials. Therefore, we conclude that hydrodynamical parameters like the quark and gluon flow parameters act as critical regulatory agents controlling QGP fluid dynamics to permit stable droplet configurations. Establishing this droplet stability opens up pathways to systematically investigate other thermodynamic characteristics of the QGP medium.

Acknowledgments

The author expresses sincere gratitude to K K Gupta for insightful discussions and a meticulous reading of the manuscript. The author also thanks Tushar Bhalla for his help in preparing the figures. Finally, the author gratefully acknowledges the Institution of Eminence, University of Delhi, Delhi, for providing financial support through a faculty research program grant (Ref. No./IOE/2024/12/FRP).

References

[1] A. Ali Khan *et al.* (CP-PACS), Phys. Rev. D **63**, 034502 (2001).

[2] E. Karsch, A. Peikert and E. Laermann, Nucl. Phys. B **605**, 579 (2001).

[3] C Leticia *et al.*, Prog. Part. Nucl. Phys. **124**, (2022).

[4] E. Shinlchi, AIP Conf. Proc. **1235**, 179 (2010).

[5] Y. Akiba, Prog. Theor. Phys. Suppl, **187**, 55 (2011).

[6] P. Moreau *et al.*, Astron. Nachr, **342** 715 (2021).

[7] M. Nahrgang, J. Phys: Conf. Ser, **503**, 012001 (2014).

[8] A. Sorin *et al.*, Proc. Sc (**CPOD2014**), **217**, 042 (2014).

[9] S. Borsanyi *et al.*, Phys. Rev Lett.,**125** 052001 (2020).

[10] D. Behera, S. Deb, C. R. Singh and R, Sahoo Phys. Rev. C, **109** 014902 (2024).

[11] I. Arsene *et al.* (BRAHMS), Nucl. Phys. A **757**, 1 (2005).

[12] B. B. Back *et al.* (PHOBOS), Nucl. Phys A **757**, 28 (2005).

[13] J. Adams *et al.* (STAR), Nucl. Phys. A **757**, 102 (2005).

[14] K. Adcox *et al.* (PHENIX), Nucl. Phys. A **757**, 184 (2005).

[15] J. Randrup and J Cleymans, Eur. Phys. J. A, **52**, 218 (2016).

[16] P. Senger, Particles, **2**, 499 (2019).

[17] J. J. B-Bohr, I. N. Mishustin and Th. Dossing, Nucl. Phys. A, **923**,19 (2014).

[18] I. Nalima *et al.*, Phys. Rev D **113** , 074035 (2026).

[19] A. Peshier, B. Kämpfer, O. P. Pavlenko and G. Soff, Phys. Lett. B **337**, 235 (1994).

[20] V. Goloviznin and H. Satz, Z. Phys. C - Particles and Fields **57**, 671 (1993).

[21] Ch. Chiu and Ch. Shen, Phys. Rev. C, **103**, 064901 (2021).

[22] P Romatschke, Int. J. Mod. Phys E, **19**, 1 (2010).

[23] C. Gale, S. Jeon and B. Schenke, Int. J. Mod. Phys. A, **28**, 1340011 (2013).

[24] G. Torrieri and I. Mishustin, Phys. Rev C, **78**, 021901R (2008).

[25] T. Hirano and K. Tsuda, Nucl. Phys. A **715**, 821c (2003).

[26] W. Fischler, Nucl. Phys. B **129**, 157 (1977).

[27] A. Billoire, Phys. Lett B **92**, 343 (1980).

[28] S. S. Singh and R. Ramanathan, Prog. Theo. Expt. Phys. **2014**, 103D02 (2014)

[29] A. V. Smirnov, V. A. Smirnov and M. Steinhauser, Phys. Lett. B **668**, 293 (2008).

[30] A. V. Smirnov, V. A. Smirnov and M. Steinhauser, Phys. Rev. Lett. **104**, 112002 (2010).

[31] H. Satz, Ann. Rev. Nucl. Part. Sci. **35** 245 (1985).

[32] G. Neergaad and J. Madsen, Phys. Rev. D **60**, 054011 (1999).

[33] M. B. Christiansen and J. Madsen, J. Phys. G **23**, 2039 (1997).

[34] S. S. Singh, D. S. Gosain, Y. Kumar and A. K. Jha, Pramana J. Phys. **74**, 27 (2010).

[35] R. Ramanathan, Y. K. Mathur, K. K. Gupta and A. K. Jha, Phys. Rev. C **70**, 027903 (2004).

[36] S. S. Singh, K. K. Gupta and A. K. Jha, Int. J. Mod. Phys. A **29**, 1450097 (2014).

[37] R. Balian and C. Block, Ann. Phys. **60**, 401 (1970).